

EVALUATING NEW SPECTRAL ANALYSIS TECHNIQUES TO STUDY THE HOT SURFACE OF MERCURY WITH MERTIS ON BEPICOLOMBO



Dissertation zur Erlangung des akademischen Grades eines
Doktors der Naturwissenschaften (Dr. rer. nat)

vorgelegt als kumulative Arbeit
am Fachbereich Geowissenschaften
der Freien Universität Berlin

von

INDHU VARATHARAJAN

Berlin, 2020

Erstgutachter: Prof Dr Harry Becker
Freie Universität Berlin
Institut für Geologische Wissenschaften
Arbeitsbereich Geochemie

Zweitgutachter: Prof. Dr. Harald Hiesinger
Westfälische Wilhelms-Universität
Geologische Planetologie
Institut für Planetologie
Arbeitsbereich Planetologie

Tag der Disputation: February 16, 2021

EIDESSTATTLICHE ERKLÄRUNG

Hiermit erkläre ich, dass ich die beigefügte Dissertation selbständig verfasst und keine anderen als die angegebenen Hilfsmittel genutzt habe.

Ich versichere weiterhin, dass ich die beigefügte Dissertation nur in diesem und keinem anderen Promotionsverfahren eingereicht habe und, dass diesem Promotionsverfahren keine endgültig gescheiterten Promotionsverfahren vorausgegangen sind.

Berlin, Nov 2020

Indhu Varatharajan

TO MOM, DAD, AND SISTER

We shall not cease from exploration. And the end of all our exploring will be to arrive where we started and know the place for the first time.

T.S. Eliot, Little Gidding.

ACKNOWLEDGEMENTS

Pursuing PhD has been my childhood dream and past four years was a roller coaster ride for me. During this PhD journey, I had my first opportunity to conduct experiments using synchrotron facility, had my first ever telescope observations sitting on the remote Hawaiian islands of the Pacific Ocean, climbed a volcanic mountain for the first time for field analogue studies, had the first opportunity to experience a launch at the Mission Control Center at ESA for BepiColombo mission, and participated in 8 week summer research accelerator learning and applying Artificial Intelligence at Oxford University. Other than scientific expenditure, this opportunity enabled me to explore the unknown territories and gave me chance to experience various cultures, languages, and food. All of these experiences enriched my PhD journey with beautiful memories which would not have been possible without freedom, trust, and constant support given by my advisor and mentor Jörn Helbert. I am deeply grateful to you for offering this PhD opportunity and allowing me to explore this journey by giving me the absolute physical and scientific mobility. You have always kept your doors open for me and stood by me strongly even during my worse mental health episodes. I can't thank you enough for being my constant source of strength and inspiration throughout this journey.

Since the first day I joined PhD, my colleagues at Planetary Spectroscopy Lab (PSL), Alessandro Maturilli and Mario D'Amore, you both made me instantly feel as a part of the MERTIS team, and also a part of a family. I have learnt a lot from both of you starting from laboratory experiments to pythonic thinking. I sincerely thank you for providing me the sustained support and comfort zone that helped me at every step of the way.

I am very grateful to you, Harry Becker, for allowing me to have registered under your supervision at Freie University Berlin for this PhD. Every discussion with you had inspired me to diversify my scientific thoughts and literature survey in various aspects to Mercury. I thank you whole heartedly for the unwavering support and care.

My PhD journey is certainly incomplete without my EPEC (Europlanet Early Career) peers. Since September 2017, you have been my tenacious shadow during my entire venture and it's an absolute honor to have worked with you as a Chair for all these years. Professional learnings and personal friendships that I got along this EPEC journey were ineffable. Thank you Rutu Parekh, Gianluca Carneilli, Solmaz Adeli, Maike Neuland, Erica Luzzi, Noah Jaggi, Petr Brož, Joanna S Oliveira, Joanna Marques Oliveira, Fulvio Franchi, Ottaviano Reutsch, Hans Huybrighs, Ana Cernok, Anastasia Kokori, Ana Losiak, Melossa Mirino, Gene Schmidt, and entire EPEC network – I am so proud to be a part of this amazing team and I always will!! Special thanks to Lena Noack, Nigel Mason, and Anita Heward for providing me this amazing opportunity.

I sincerely thank all my collaborators for all the support and discussions throughout all these years: Thank you Olivier Namur, Georg Ulrich, Bernd Kästner, Kay Woltharth, Christian Woehler, Constantine Tsang, Cristian Althaus, Katrin Stephan, Matthias Grott, Sebastian Besse, David Rothery, Harry Hiesinger, Iris Weber, Karin Bauch, Kirsten Born, Lutz Hecht, Bhala Sivaraman, Vijayan S, Rishitosh Sinha, Anil Bhardwaj, Jaya Krishna, Shyama Narendranath, Megha Bhatt, Amit Basu. I will not forget the timely help provided by Claudia Hauschild and Plaul Stephanie with all my immediate requests on visa processing and other PhD related requests.

I would like to extend my gratitude to Harry Becker and Harry Hiesinger to have agreed to act as experts to review my thesis. I thank my entire doctoral committee for agreeing to be a part of my final and important phase of my PhD: Thank you - Frank Potsberg, Lena Noack, Timm John, Harry Becker, and Jorn Helbert.

To all my friends and colleagues at DLR, I am extremely thankful to you for being my companion over the last few years. I am indebted to the random laughs, mensa lunch discussions, unconditional support, and honest feedback that I received from all of you. Thank you Rutu, Giulia, Jinia, Solmaz, Nasia, Janani, Yaqui, Sabrina, Kay, Narendra, Max, Mika, Claudia.

This PhD thesis is dedicated first to my world - my mom, dad, and my sister. Amma (mom) – you have always been an unconditional source of love and inspiration to me as long as I could remember. Thank you so much for believing in me and allowing me to explore my life with all the freedom, trust, and support. You taught me everything I know. You taught me to be bold, independent, curious, kind, and everything I am now. You are my first inspiration and my role model. My life and everything it contain is dedicated to you. Appa (dad), you were the one triggered my scientific curiosity that drives me every day when I wake up. You were the first one to call me as “scientist daughter” even before I even got my Masters. You saw a successful scientist in me even before this world could see. I would not have followed my dreams if you hadn’t taught me “being unconventional and dreaming big” is OK. I am the one who walk on this road but it was you who aspired me for this journey. I know that wherever you are, you are still watching me and blessing me with all the love in your heart. Thank you so much for teaching me important life lessons that made least sense to me then but help me guide through now in this complex world. You are the one who constantly keeps me in check even during your absence. Bujji (sister) – though you are my younger sister, you are my second parent, my first best friend, and a great companion since childhood. Thank you for coming into my life and being my constant source of hope, happiness, and love.

My last and very special dedication is to my then boyfriend and now fiancé Hari (Dada), who has always been equally passionate about my dreams as I am. You put a name plate on my worktable “Dr. Indhu Varatharajan” on the first day of my PhD and it has always reminded me of what I needed to do to make it real especially during challenging time. The amount of pride your eyes carry when you talk about my passions and dreams, has been my strongest anchor to fulfill my ambitions. These five years of long distance would not have been made easier without your unconditional support and love. You have always been my strongest pillar, infinite source of love and an unshaken endurance, even during my worst moods and phases. Thank you for loving me for who I am and always keeping me in your thoughts in every minute decision of your everyday life.

ABSTRACT

Mercury is the closest planet to the Sun and its formation still remains unclear. It is an important boundary condition for formation models of our solar system and planetary system in general. Among the exoplanets many planets have been discovered in similar distances from their host star. Due to the closeness to the Sun Mercury experiences extreme temperature variations (-150°C – 450°C) during its day-night cycles. Spectroscopy is one of the most powerful techniques to study the surface mineralogy of any planetary body from its orbit. Various spectral ranges provide different insights to the surface we look at. In order to spectrally interpret the surface mineralogy, it is important to understand the spectral behavior of the planet's analogues under its respective surface environment conditions in a controlled laboratory setup.

This thesis focuses primarily on understanding the composition of Mercury from orbital remote sensing observations, especially with the Mercury Radiometer and Thermal Imaging Spectrometer (MERTIS) instrument onboard ESA-JAXA BepiColombo mission to Mercury. MERTIS will be the first radiometer and the first thermal infrared (TIR; 7-14 μm) hyperspectral spectrometer to orbit Mercury. To this purpose a specialized spectral library was created of various Mercury analogues under their extreme environmental conditions as a function of temperature under vacuum, the stability and spectral signature of a range of sulfides was studied, the derivation of various spectral parameters to facilitate the mapping of surface composition was evaluated and with these the analysis of data in the visible and near-infrared by the NASA MErcury Surface, Space ENvironment, GEochemistry, and Ranging (MESSENGER) was revisited. The specialized emissivity spectral library of 7 synthetic sulfides and 10 terrestrial silicates, as potential Mercury analogues, has been developed as a function of temperature ranging from 100°C to 500°C under vacuum. Put together, they will aid the mapping of the crustal and volcanic mineralogy of the Mercury surface. The new spectral parameter developed in the presented work on laboratory silicate mineralogy study shows that olivine, pyroxenes, and feldspar groups can be successfully separated by MERTIS.

MESSENGER mission carried two visible infrared spectrometers (0.45-1.45 μm), Mercury Atmospheric and Surface Composition Spectrometer (MASCS; hyperspectral-point spectrometer), and Mercury Dual Imaging System (MDIS; multispectral-imaging spectrometer), to map the surface mineralogy of Mercury. However, due to Fe-poor nature of the Mercury surface materials, the spectrometers revealed featureless red-sloped spectra across major surface units. This limited the direct mapping of the silicate mineralogy of the Mercury's crustal and volcanic rocks, and therefore, remains only as estimated mineralogy using the data obtained from geochemistry suite. In the presented study, the global multivariate analysis of MASCS data was carried out to understand the spectral diversity of the planet and its relation to the known geochemical terrains mapped by geochemistry suite. The study for the first time spectrally distinguished between low-Mg and high-Mg northern volcanic plains.

One of the major discoveries of NASA MESSENGER mission is the discovery of widely spread hollows on Mercury surface, which are indicative of possible sublimation processes of the volatile-rich minerals. As sulfides are strongly proposed as the potential candidates of hollow materials, MgS, FeS, CaS, CrS, TiS, NaS, and MnS are studied for its emissivity spectra as a function of temperature in vacuum, further, the ultraviolet- to far-infrared reflectance

spectroscopy of the fresh and thermally weathered sulfides under vacuum are also investigated in the presented work. This unique spectral library of sulfides will enable mapping of volatile-rich surface mineralogy of Mercury by spectrometers onboard MESSENGER and BepiColombo missions. Further, the extended study presented in this thesis investigates the emissivity spectral behavior of CaS for four simulated Mercury days. The results from this study prove CaS is the most stable sulfides that survives the extreme thermal environment of Mercury and is an important tracer for other sulfides those might be lost in the hollow-forming process dominated by sublimation. The emissivity spectra reported here are significant for the detection and mapping of CaS associated with hollows and pyroclastics using MERTIS datasets.

This thesis is a cumulative work comprising of six peer-reviewed manuscripts out of which three are published and three are in correspondence with their respective journals for publications.

KURZFASSUNG

Merkur ist der sonnennächste Planet, daher erfährt seine Oberfläche während seiner Tag-Nacht-Zyklen extreme Temperaturschwankungen (-150 °C – 450 °C). Die Hauptbeiträge dieser Arbeit konzentrieren sich auf die Erstellung einer spezialisierten Spektralbibliothek verschiedener Merkur-Analoga unter ihren extremen Umweltbedingungen als Funktion der Temperatur im Vakuum und die Ableitung spektraler Parameter zur Erleichterung der Kartierung der Oberflächenzusammensetzung. Spektroskopie ist eine der leistungsstärksten Techniken zur Untersuchung der Oberflächenmineralogie eines Planetenkörpers von seiner Umlaufbahn aus. Verschiedene Spektralbereiche liefern unterschiedliche Einblicke in die Oberfläche, die wir betrachten. Um die Oberflächenmineralogie spektral zu interpretieren, ist es wichtig, das spektrale Verhalten der Analoga des Planeten unter seinen jeweiligen Oberflächenumgebungsbedingungen in einem kontrollierten Laboraufbau zu verstehen. Diese einzigartige Spektralbibliothek wird die MERTIS-Nutzlast an Bord der ESA-JAXA BepiColombo-Mission zum Merkur unterstützen. Mercury Radiometer and Thermal Imaging Spectrometer (MERTIS) wird das erste Radiometer und das thermische Infrarot (TIR; 7-14 μm) Hyperspektralspektrometer sein, das den Merkur umkreist. In der vorgestellten Arbeit wurde die spezialisierte Emissivitätsspektralbibliothek von 7 synthetischen Sulfiden und 10 terrestrischen Silikaten, den potentiellen Merkur-Analoga, als Funktion der Temperatur im Bereich von 100°C bis 500°C unter Vakuum entwickelt. Zusammengenommen helfen sie bei der Kartierung der Krusten- und Vulkanmineralogie der Merkur-Oberfläche mit einer räumlichen Auflösung von 500 m/Pixel. Die neue spektrale Darstellung, die in der vorgestellten Arbeit über die Laborstudie zur Silikatmineralogie entwickelt wurde, zeigt erfolgreich, dass Olivin-, Pyroxen- und Feldspatgruppen von MERTIS unterscheidbar sind.

Die NASA-Mission MErcury Surface, Space ENvironment, GEOchemistry, and Ranging (MESSENGER) führte zwei Spektrometer für das sichtbare Infrarot (0,45-1,45 μm), das Mercury Atmospheric and Surface Composition Spectrometer (MASCS; Hyperspektral-Punkt-Spektrometer) und das Mercury Dual Imaging System (MDIS; Multispektral-Imaging-Spektrometer) mit, um die Oberflächenmineralogie von Merkur zu kartieren. Aufgrund der eisenarmen Beschaffenheit der Merkur-Oberflächenmaterialien zeigten die Spektrometer jedoch über die wichtigsten Oberflächeneinheiten merkmalslose rotabgestufte Spektren. Dies schränkte die direkte Kartierung der Silikatmineralogie der Kruste und des Vulkangesteins des Merkur ein und bleibt daher nur als geschätzte Mineralogie unter Verwendung der aus der Geochemie-Suite erhaltenen Daten erhalten. In der vorgestellten Studie wurde die globale multivariate Analyse der MASCS-Daten durchgeführt, um die spektrale Vielfalt des Planeten und ihre Beziehung zu den bekannten geochemischen Terrains, die von der Geochemie-Suite kartiert wurden, zu verstehen. Die Studie unterschied zum ersten Mal spektral zwischen den nördlichen Vulkanebenen mit niedrigem und hohem Mg-Gehalt.

Eine der wichtigsten Entdeckungen der NASA-MESSENGER-Mission ist die Entdeckung weit verbreiteter Hohlräume auf der Merkur-Oberfläche, die auf mögliche Sublimationsprozesse der Minerale mit hohem Anteil an flüchtigen Stoffen hindeuten. Da Sulfide als potentielle Kandidaten für Hohlmaterialien vorgeschlagen werden, werden MgS, FeS, CaS, CrS, TiS, NaS und MnS auf ihre Emissionsgradspektren als Funktion der Temperatur im Vakuum untersucht. Darüber hinaus wird in der vorliegenden Arbeit auch die Ultraviolett- bis Ferninfrarot-Reflexionsspektroskopie der frischen und thermisch verwitterten Sulfide im

Vakuum untersucht. Diese einzigartige Spektralbibliothek von Sulfiden wird die Kartierung der flüchtigen-reichen Oberflächenmineralogie des Merkur durch Spektrometer an Bord der MESSENGER- und BepiColombo-Missionen ermöglichen. Darüber hinaus untersucht die in dieser Arbeit vorgestellte erweiterte Studie das spektrale Emissionsgradverhalten von CaS für vier simulierte Merkurtage. Das Ergebnis der Studie beweist, dass CaS das stabilste Sulfid ist, das die extreme thermische Umgebung von Merkur überlebt, und dass es ein wichtiger Tracer für andere Sulfide ist, die in dem von Sublimation dominierten Hohlformprozess verloren gehen könnten. Die hier berichteten Emissionsgradspektren sind für den Nachweis und die Kartierung von CaS in Verbindung mit Hohlräumen und Pyroklastika unter Verwendung von MERTIS-Datensätzen von Bedeutung.

Diese Dissertation ist eine kumulative Arbeit, die sechs begutachtete Manuskripte umfasst, von denen drei veröffentlicht wurden und drei von denen drei veröffentlicht und drei zur Veröffentlichung in Fachzeitschriften eingereicht wurden.

TABLE OF CONTENTS

Abstract	xi
Kurzfassung.....	xiii
List of figures.....	xix
List of tables.....	xxi
1. INTRODUCTION	1
1.1 SPECTROSCOPY AND SURFACE SCIENCE.....	1
1.1.1 <i>Electromagnetic radiation and its interaction with surface material</i>	2
1.1.1.1 Reflectance spectroscopy.....	4
1.1.1.2 Emittance spectroscopy	5
1.1.2 <i>Factors affecting reflectance and emittance spectroscopy</i>	7
1.1.3 <i>Building planetary spectral library under controlled laboratory conditions</i>	8
1.1.3.1 Fourier transform infrared (ftir) spectroscopy approach	9
1.1.3.2 Importance of simulated planetary environment conditions.....	10
1.2. MERCURY AND ITS SURFACE EXPLORATION	12
1.2.1 <i>Enigmatic Mercury</i>	13
1.2.1.1 The origin.....	13
1.2.1.2 The volatile-rich interior	13
1.2.1.3 Spectral reflectance.....	15
1.2.1.4 Surface Mineralogy	17
1.2.2 <i>Bepicolombo and its Spectrometers for Direct Surface Mineralogy Studies</i>	19
1.3. SCOPE OF THIS THESIS.....	22
2. Global Multivariate Spectral Analysis of Mercury and the Identification of Geochemical Terrains: Derived from the MASCS Spectrometer onboard NASA's MESSENGER Mission	27
2.1 ABSTRACT	28
2.2 INTRODUCTION	29
2.3 CREATION OF GLOBAL MASCS HYPERSPECTRAL CUBE	33
2.4 STANDARD SPECTRAL PARAMETER MAPS	35
2.4.1 <i>UV downturn</i>	35
2.4.2 <i>Visible Slope and Normalized Visible Slope</i>	35
2.5 STATISTICAL ANALYSIS TECHNIQUES	37
2.5.1 <i>Unsupervised Clustering Analysis</i>	37
2.5.2 <i>Principal Component Analysis</i>	40
2.6 REGIONAL AND GLOBAL PERSPECTIVE OF MASCS PRIMARY PCs.....	41
2.6.1 <i>Principal Component (#1)</i>	43
2.6.2 <i>Principal Component (#2)</i>	43
2.6.3 <i>Principal Component (#6)</i>	44
2.7 GLOBAL MULTIVARIATE SPECTRAL ANALYSIS.....	51
2.7.1 <i>Comparative Analysis of MASCS-derived Spectroscopy, Mineralogy, and Morphology of various Geochemical Terranes of Mercury</i>	54
2.7.1.1 One color units: NP, RB, PD, HAI-East	57
2.7.1.2 Two-color units: CB, HAI-West	58
2.7.1.3 Multi-color units: HMR, HMR-CaS, IT	58
2.8 SUMMARY AND CONCLUSIONS.....	58
2.9 ACKNOWLEDGEMENTS	61
2.10 SUPPORTING INFORMATION	61
3. The Planetary Spectroscopy Laboratory (PSL) – wide spectral range, wider sample temperature range	65
3.1 ABSTRACT	66
3.2 INTRODUCTION	66
3.3 PSL SET-UP DESCRIPTION.....	67
3.4 PSL SUPPORT EQUIPMENT.....	69
3.5 SPECTRAL MEASUREMENT OF SAMPLE EMISSIVITY	71
3.6 SPECTRAL MEASUREMENT OF SAMPLE REFLECTANCE.....	74

3.7 SPECTRAL MEASUREMENT OF SAMPLE TRANSMITTANCE	75
3.8 CONCLUSION	76
4. Spectral Behavior of Sulfides in Simulated Daytime Surface Conditions of Mercury: Supporting past (MESSENGER) and future missions (BepiColombo).....	79
4.1 ABSTRACT	80
4.2 INTRODUCTION	81
4.3 SAMPLES	83
4.4 METHODS.....	83
4.4.1 Facility – Planetary Spectroscopy Laboratory (PSL)	83
4.4.2 Emissivity.....	86
4.4.3 Reflectance.....	86
4.5 RESULTS	87
4.5.1 Emissivity.....	87
4.5.2 Reflectance.....	92
4.5.2.1 Ultraviolet-Visible (UV/VIS): 0.2 - 0.6 microns	92
4.5.2.1.1 Fresh sulfides	93
4.5.2.1.2 T-processed sulfides	94
4.5.2.2 Visible-Infrared (VIS-IR): 0.3 – 1 microns.....	95
4.5.2.3 Near infrared (NIR): 1-6 microns	97
4.5.2.4 Mid Infrared/Thermal Infrared (MIR/TIR): 7-14 μ m	99
4.5.2.5 Far Infrared (FIR): 15-100 microns	101
4.6 DISCUSSIONS.....	102
4.6.1 BepiColombo MERTIS	102
4.6.2 MESSENGER MASCS	103
4.6.3 BepiColombo SIMBIO-SYS/VIHI	104
4.6.4 Spectral behavior of sulfides with respect to phase angle and temperature.....	105
4.7 CONCLUSIONS	108
4.8 ACKNOWLEDGEMENT.....	108
4.9 SUPPORTING INFORMATION	108
4.9.1 Planetary Spectroscopy Laboratory (PSL) in detail.....	108
4.9.2 Step-by-step procedure of emissivity measurements of sulfides at psl.....	109
4.9.3 Step-by-step procedure of reflectance measurements of sulfides.	110
5. Thermal Stability and Emissivity Behavior (7-14 μm) of Calcium-Sulfides under Simulated Daytime Surface Conditions for Multiple Mercury days: Implications for the formation of hollows and Calcium-Sulfide detection by MERTIS onboard the BepiColombo mission	113
5.1 ABSTRACT	114
5.2 INTRODUCTION	115
5.3 SAMPLE, FACILITY AND METHODS	116
5.3.1 Emissivity.....	116
5.3.2 X-Ray Diffraction (XRD)	120
5.4 RESULTS AND DISCUSSIONS	120
5.4.1 Emissivity measurements.....	120
5.4.2 XRD Analysis.....	122
5.5 IMPLICATIONS.....	124
5.6 CONCLUSIONS	127
5.7 ACKNOWLEDGEMENTS	127
6. Thermal Infrared Spectroscopy (7-14 μm) of Silicates under Simulated Mercury Daytime Surface Conditions and their Detection: Supporting MERTIS onboard the BepiColombo Mission	129
6.1 ABSTRACT	130
6.2 INTRODUCTION	130
6.3 SAMPLE SELECTION, PREPARATION AND CHARACTERIZATION	133
6.4 METHODS.....	135
6.4.1 Spectroscopy facility.....	135
6.4.2 Experimental set-up and procedure	136
6.4.3 Spectral parameters studied	138

6.5 RESULTS	140
6.5.1 Olivine (<i>forsterite</i>)	141
6.5.2 Pyroxenes (<i>enstatite, diopside, hypersthene</i>)	141
6.5.3 Feldspars (<i>anorthite, labradorite, andesine, oligoclase, microcline</i>)	142
6.5.4 Feldspathoid (<i>nepheline</i>).....	143
6.6 DISCUSSIONS	144
6.6.1 <i>Spectral trends as a function of temperature</i>	144
6.6.2 <i>Application to MERTIS data analysis</i>	146
6.7 CONCLUSIONS	148
6.8 ACKNOWLEDGMENTS	148
6.9 SUPPORTING INFORMATION	149
7. The Mercury Radiometer and Thermal Infrared Imaging Spectrometer (MERTIS) onboard BepiColombo: first inflight calibration results	153
7.1 ABSTRACT	154
7.2 INTRODUCTION	154
7.2.1 <i>BepiColombo Mission</i>	154
7.2.2 <i>MERTIS Instrument</i>	155
7.3 NEAR EARTH COMMISSIONING PHASE OPERATIONS.....	158
7.4 NEAR EARTH COMMISSIONING PHASE RESULTS	159
7.4.1 <i>TIS Spectrometer</i>	159
7.4.2 <i>TIR Radiometer</i>	161
7.5 CONCLUSIONS	162
8. Conclusions	165
8.1 SUMMARY	165
8.1.1 <i>Surface science from MASCS spectrometer</i>	165
8.1.2 <i>Specialized Spectral Library under simulated Daytime Surface conditions of Mercury</i>	166
8.1.2.1 Sulfide mineralogy	167
8.1.2.2 Silicate mineralogy	168
8.2 IMPLICATIONS.....	169
Bibliography	173

LIST OF FIGURES

Figure 1.1. Electromagnetic radiation	3
Figure 1.2. Interaction of the incoming radiation on the semitransparent material	4
Figure 1.3. Key angles that defines the scattered geometry	5
Figure 1.4. Relation between the spectral radiance curves for Sun (5778 K), Mercury (700 K), and Earth (283 K) .	6
Figure 1.5. Working principle of FTIR spectrometer	9
Figure 1.6. Extreme thermal environment of Mercury surface	11
Figure 1.7. Images of Pyroclastic vent “Nathair Facula” and hollows within the crater Eminescu	14
Figure 1.8. Visible-infrared spectra of Moon vs Mercury	16
Figure 1.9 Major Geochemical terranes of Mercury.....	18
Figure 1.10. The relationship between MESSENGER and BepiColombo orbits for MPO and MMO	20
Figure 2.1. MDIS enhanced global color mosaic of Mercury overlaid by the geochemical terranes	31
Figure 2.2. Standard spectral parameter maps derived from MASCS hyperspectral datacube	36
Figure 2.3. K-means clustering of global MASCS datacube of Mercury	38
Figure 2.4. Principal Component Analysis (PCA) coefficients maps of global MASCS datacube.....	42
Figure 2.5. PC1 map vs Global MASCS reflectance at 750 nm	43
Figure 2.6. PC2 map vs nanophase iron map of Mercury	44
Figure 2.7. PC6 map overlaid on the MDIS 8-color basemap.....	45
Figure 2.8. MASCS false color composite (FCC) map created from PC1, PC2, and PC6 maps	52
Figure 2.9. Global MASCS False Color Composite Map at equirectangular and stereographic projections	55
Figure 2.10 Number density of MASCS spectra per pixel used to create global MASCS spectral cube.....	61
Figure 2.11. Global MASCS reflectance variability map at 700 nm	62
Figure 2.12. Distribution of MASCS visible detector temperature for all observations	62
Figure 2.13. K-means clustering map for k values = 2,3,4,5,6,7,8,9,10.....	63
Figure 3.1. The Laboratory set-up at PSL.....	68
Table 3.1. Collection of detectors equipment available at PSL.	68
Figure 3.2. Sketch of the support equipment at the PSL.	70
Figure 3.3. Emissivity spectra of a quartz sample taken in vacuum at increasing temperatures.	72
Figure 3.4. Webcam picture of a sample cup, sample measured surface temperature is 600°C.....	73
Figure 3.5. Bi-directional reflectance spectrum of the PlanetX sample measured at the PSL in the whole spectral range from UV to the FIR (0.2 – 150 μm).	75
Figure 3.6. Transmittance spectrum of a pellet made of 1% quartz (0-25 μm) + 99% KBr	76
Figure 4.1. Laboratory set-up at PSL.....	84
Figure 4.2. Graphical summary of the methodology used in the study to measure the emissivity and reflectance spectra.....	85
Figure 4.3. Emissivity of the sulfides measured at 100 °C, 200 °C, 300 °C, 400 °C, and 500 °C at spectral range of 7-14 μm	87

Figure 4.4. Measured reflectance at phase angles 26°, 40°, 60°, and 80° at UVVIS spectra range (0.2 – 0.6 μm) of fresh and T-processed sulfides	93
Figure 4.5. Measured reflectance at phase angles 26°, 40°, 60°, and 80° at VIS-IR spectra range (0.3 – 1 μm) of fresh and T-processed sulfides	96
Figure 4.6. Measured reflectance at phase angles 26°, 40°, 60°, and 80° at NIR spectra range (1 – 6 μm) of fresh and T-processed sulfides	98
Figure 4.7. Measured reflectance at phase angles 26°, 40°, 60°, and 80° at MIR/TIR spectra range (7 – 14 μm) of fresh and T-processed sulfides	100
Figure 4.8. Measured reflectance at phase angles 26°, 40°, 60°, and 80° at FIR spectra range (15 – 100 μm) of fresh and T-processed sulfides	101
Figure 4.9. Measured reflectance at phase angles 26°, 40°, 60°, and 80° at complete spectra range studied (0.2 – 100 μm) for both fresh and heated sulfides	107
Figure 5.1 Graphical illustration of laboratory set-up at PSL for high temperature emissivity measurements....	117
Figure 5.2. Graphical summary of the methodology used in the study to measure the emissivity of calcium sulfides (CaS) for four heating cycles	118
Figure 5.3. Emissivity measurements showing emissivity behavior of CaS under four simulated Mercury daytime surface conditions	122
Figure 5.4. XRD diffratogram of fresh CaS and thermally processed CaS after four heating cycles	123
Figure 5.5 The peak surface temperature distribution across Mercury surface	125
Figure 6.1. Graphical illustration of laboratory set-up at PSL for high temperature emissivity measurements....	136
Figure 6.2. Graphical summary of the methodology to measure temperature-dependent emissivity spectra ...	137
Figure 6.3. Emissivity spectra of all the studied powdered silicates of grain sizes < 25 μm for temperatures 100 °C, 200 °C, 300 °C, 400 °C, and 500 °C under vacuum	140
Figure 6.4. Derived spectral parameters; CF position (μm), RB1 position (μm), RB1 emissivity, and RB spectral contrast (μm) for each silicate vs corresponding sample temperature.	144
Figure 6.5. Plot between CF position and RB1 position (CF vs RB1 plot)	147
Figure 7.1. Schematic view of the MERTIS instrument	156
Figure 7.2. List of Telecommands sent to MERTIS instrument during BepiColombo Near Earth Commissioning Phase (NECP)	158
Figure 7.3. Radiance Values from different MPOI position and from 700K hot blackbody during inflight and on-ground	160
Figure 7.4. Barycenter shift between MERTIS NECP data and laboratory data measured in Thermo Vacuum Chamber	161
Figure 7.5. BB700 – Space and BB300 – Space of TIS and TIR MERTIS data during NECP	162

LIST OF TABLES

Table 1.1 Comparison between experimental and normative mineralogy of various geochemical units of Mercury from MESSENGER datasets	19
Table 3.2. Collection of beamsplitters equipment available at PSL.....	69
Table 4.1. Characteristic spectral absorption bands for detection of sulfides by MERTIS	104
Table 4.2. Detection of sulfides in the spectral range (1-100 μm) for reflectance measurements.....	106
Table 4.3. List of sulfide samples used in the study.....	112
Table 4.4. Instrument specifications and spectral ranges of measurements at PSL	112
Table 6.1. Summary of silicate minerals used in this study.....	134
Table 6.2. Oxides content of the silicate minerals used in the study	135
Table 6.3. Spectral parameters derived from the emissivity spectra of all studied silicates as a function of temperature.	149

1

INTRODUCTION

1.1 SPECTROSCOPY AND SURFACE SCIENCE

Identifying the nature and abundance of minerals on a planetary surface is the most vital step to unravel its formation and geological evolution. Remote sensing enables us to perform global investigation of various aspects of planets including the geologic history that shapes the physical and composition of the planet's surface, atmosphere, and magnetosphere (Emery *et al.*, 2017). Almost everything we know about the surfaces of the solar system bodies is enabled by remote sensing. Remote sensing is enabled by the study of interaction of the light that are emitted and scattered by any particular media including planetary regoliths in space and planetary analogues in the laboratory (Wu *et al.*, 2018, Guanter *et al.*, 2019). When such study is investigated over the function of wavelength then it's called spectroscopy (Shirley and Fairbridge, 1997, Hapke, 2012). The particles with different composition and physical structure exhibits different spectral features over a wide spectral range. These spectral signatures intimately relate to the crystal structure of the particles and therefore aiding the determination of their chemical composition and mineralogy through remote sensing (Hapke, 2012, Bishop *et al.*, 2019).

Spectroscopy thus becomes the powerful tool to remotely study the surface mineralogy, chemical and physical make up of any planetary body. Spectrometers with wide spectral range, greater spectral and spatial resolution with repeated orbital coverage are helping us to map the surface mineralogy of planets in greater detail. Various spectral ranges tell different stories and properties of the surface we look at (Hapke, 2012, Bishop *et al.*, 2019). For eg., visible-infrared (VIS-IR) surface spectroscopy of an atmosphereless rocky planet can tell us about the distribution of Fe, Ti, Mg, Ca rich minerals for both its igneous and sedimentary phases whereas thermal IR spectroscopy reveals the Si-O abundance on the bulk mineralogy of the pixel we look at (Pieters and Englert, 1993, Bishop *et al.*, 2019). By carefully understanding the spectral behavior of various planetary analogues in laboratory experiments

at the planetary surface and environmental conditions, one can map the mineral abundance and distribution globally from orbit.

Orbital spectroscopy in planetary remote sensing is enabled by detectors that are capable of recording the reflected or emitted spectral signal from the planet surface at various discrete wavelengths at the same time (Wu *et al.*, 2018, Guanter *et al.*, 2019, Booysen *et al.*, 2020). These orbital spectrometers can be either multispectral or hyperspectral modes (Farrand *et al.*, 2019). The major difference between these modes are the number of spectral bands that these spectrometers are able to record. Multispectral remote sensing only enables us to map the surface between 3 to 10 spectral bands, whereas, hyperspectral remote sensing enables us to map each surface pixel at up to hundreds or even thousands of closely spaced and continuous spectral bands (Booyesen *et al.*, 2020). Imaging spectrometers therefore help us to effectively map the surface and its properties from the orbit and also very useful on a rover, balloon or plane (Farrand *et al.*, 2019, Booysen *et al.*, 2020).

1.1.1 ELECTROMAGNETIC RADIATION AND ITS INTERACTION WITH SURFACE MATERIAL

Electromagnetic radiation (EMR) is energy that propagates through vacuum (free space) or medium (atmosphere of planets) in the form of an advancing interaction between electric and magnetic fields (Fig. 1.1) (Clark and Rilee, 2010, Hapke, 2012, Pérez-Juste and Faza, 2015). The Sun is the primary source of EMR in our solar system but it's not the only one. All matter (such as Sun, human body) with the absolute temperature (in K) above zero emits EMR energy due to the vibrations among the molecular bonds because of molecular agitation (Clark and Rilee, 2010, Hapke, 2012, Pérez-Juste and Faza, 2015). This energy is called emittance energy and are described in detail in section 1.1.1.2.

Our Sun radiates this electromagnetic energy over a wide range of wavelengths and emits the most radiation in the visible portion of the spectrum (see Fig. 1.4). Before the electromagnetic energy from the Sun reaches the planet's surface, it passes through the atmosphere if present (e.g., Earth and Venus) (Chance and Martin, 2017). For planets without significant atmosphere e.g., Mercury, this electromagnetic radiation at all wavelengths interacts directly with the planet's surface materials (Bishop *et al.*, 2019, Murchie *et al.*, 2019).

When EMR photons interact with surface materials, some are reflected from the grain surfaces, some are absorbed by the grains, and some are transmitted through the surface

grains (Fig. 1.2) such that Total Incident Energy (G) = Reflectance (ρG) + Absorbance (αG) + Transmittance (τG), where, reflectivity (ρ), absorptivity (α), and transmissivity (τ) are defined as the fractions of the original incident light (G) such that the sum of the reflected, absorbed, and transmitted energy should be equal to the incident radiation due to law of conservation of energy (Clark and Rilee, 2010, Hapke, 2012, Pérez-Juste and Faza, 2015).

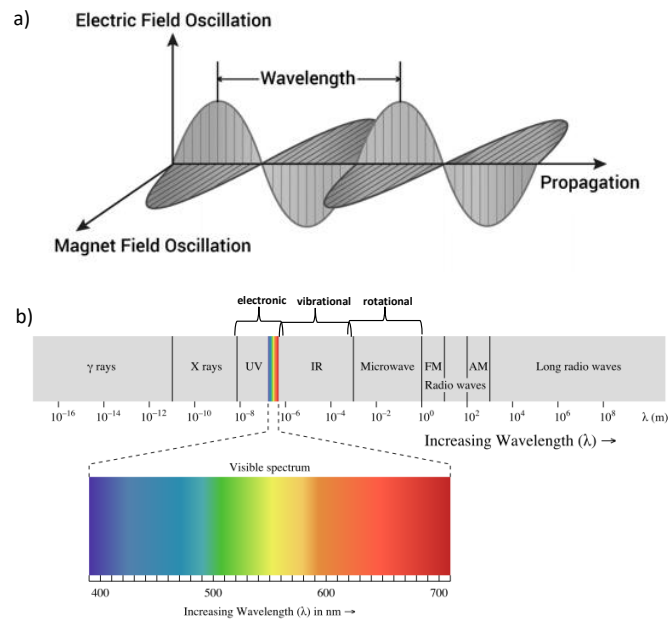


Figure 1.1. a) shows the direction of electromagnetic wave propagation and its corresponding electric and magnetic field oscillation perpendicular to each other. b) shows the complete range of EMR energy emitted by the Sun which further interacts with all solar-system objects.

These physical parameters (ρ , α , τ) varies depending on the material and its physical and chemical state, the surface roughness as well as the geometric circumstances (e.g. incidence angle of the sunlight) (Hapke, 2012). They also vary with the wavelength of the electromagnetic energy and importantly the surface environment such as surface temperature, pressure, and space weathering conditions (Hapke, 2012). By carefully studying these differences in the reflectance/absorbance/transmittance spectra under controlled laboratory conditions, makes it possible to remotely identify the planetary surface composition, mineralogy and its physical properties from the orbit and telescope data (Reitze *et al.*, 2017, Maturilli *et al.*, 2018c, Cloutis *et al.*, 2019, Helbert *et al.*, 2019, Varatharajan *et al.*, 2019a).

Among these energies, the reflectance and the emittance energy are the only radiation that can be measured remotely from the planetary orbit or telescopic observations (Hapke, 2012). The following sub-sections are therefore focussed on the reflectance and emittance spectroscopy.

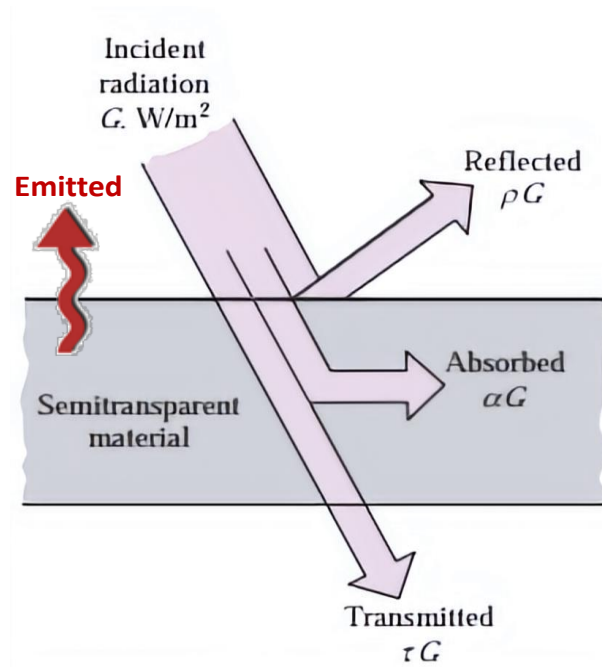


Figure 1.2. Illustration showing the interaction of the incoming radiation on the semitransparent material. Image is modified from (Çengel *et al.*, 2001)

1.1.1.1 REFLECTANCE SPECTROSCOPY

When the incident EMR hits the planetary surface, the energy absorbed by the surface minerals are influenced by several processes. These differences in the absorption processes and their wavelength dependence allow us to derive information about the chemistry of a mineral from its reflected or emitted light (Pieters and Englert, 1993, Bell, 1997, Hapke, 2012, Bishop *et al.*, 2019). In reflectance spectroscopy, the measured spectrum is understood by calculating the ratio of the amount of reflected to incident light where the absorption features (or local spectral minima) are directly associated with the chemistry and the physical nature of the surface (Bell, 1997, Hapke, 2012). These absorption features in the measured spectra are due to the electronic and vibrational processes (Bell, 1997, Hapke, 2012).

The photometric behaviour of a planetary surface defines the direction of the reflected light scattered from it. The key angular factors that controls the reflected energy includes

incidence angle (i), emergence angle (e), and the phase angle (g) (Fig. 1.3) (Hapke, 2012, Goguen, 2014, Mustard and Glotch, 2019). In order to mosaic the datasets of the instrument which mapped the surface at different geometries, the photometric modelling approach is adopted where all the datasets of an instrument are normalised for a common illumination and geometry (Bell, 1997, Hapke, 2012). Such normalisation is critical to interpret the surface mineralogy through orbital spectroscopy. However, when attempting to map the spectral behaviour of a planetary surface mapped by different instruments of different missions having each an inherent observing geometries, it becomes critical to create the spectral library of planetary analogues for varying observing geometries over a wide spectral range to enable the comparison of the results from different orbiters of the same planet (Mustard and Pieters, 1989, Maturilli *et al.*, 2018c, Varatharajan *et al.*, 2019b).

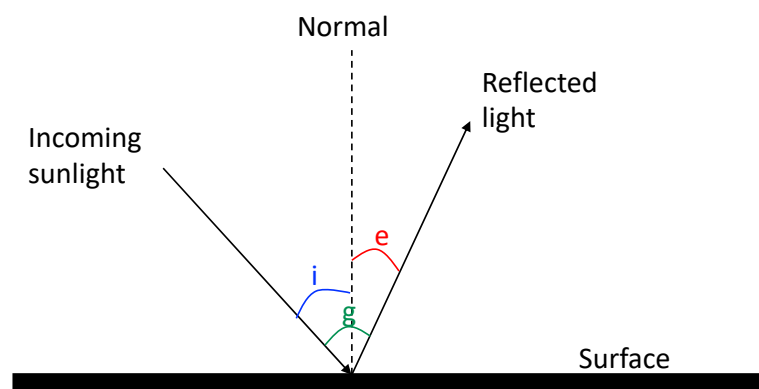


Figure 1.3. Key angles that defines the scattered geometry. Incidence angle (i) is defined by the angle between the incoming sunlight and the surface normal, emergence angle (e) is defined by the angle between the outgoing scattered or reflected light and the surface normal, and the phase angle (g) is defined by the angle between the incoming sunlight and the outgoing reflected light.

1.1.1.2 EMITTANCE SPECTROSCOPY

Emittance spectroscopy is based on the direct emitted/radiated energy from the planet/object having surface temperature greater than absolute zero (in K). In other words, there is no external light source is involved in measurement of emission spectroscopy, instead the sample/surface itself acts as the radiation source. The wavelength at which this energy is emitted directly depends at the temperature of the surface and it's based on planck's law (Hapke, 2012). Planck's law is valid only for blackbody surfaces which are assumed to be

perfect emitters. The Planck function of a black body ($U(\lambda, T)$) is defined as a function of wavelength (λ) and temperature (T) (Hapke, 2012) as shown in equation 1 below;

$$U(\lambda, T) = \frac{2\pi h_0 c_0^2}{\lambda^5} \frac{1}{e^{hc_0/\lambda k_0 T} - 1} \quad \text{----- (eq. 1)}$$

where h_0 is Planck's constant ($= 6.626 \times 10^{-34}$ J sec), c_0 is the speed of light, k_0 is Boltzmann's constant ($= 1.381 \times 10^{-23}$ J K⁻¹).

The comparative blackbody plank's curves for Sun (5778 K), Mercury (700 K), and Earth (283 K) are plotted in Fig. 1.4. Fig. 1.4 shows that the maximum emitted energy shifts to shorter wavelength with increase in temperature. Sun majorly emits at the visible wavelength range whereas the emission for Mercury and Earth peaks in the MIR infrared spectral range. Therefore, MIR spectral region is also referred as thermal infrared (TIR) spectral range (Hapke, 2012, Bandfield and Rogers, 2019).

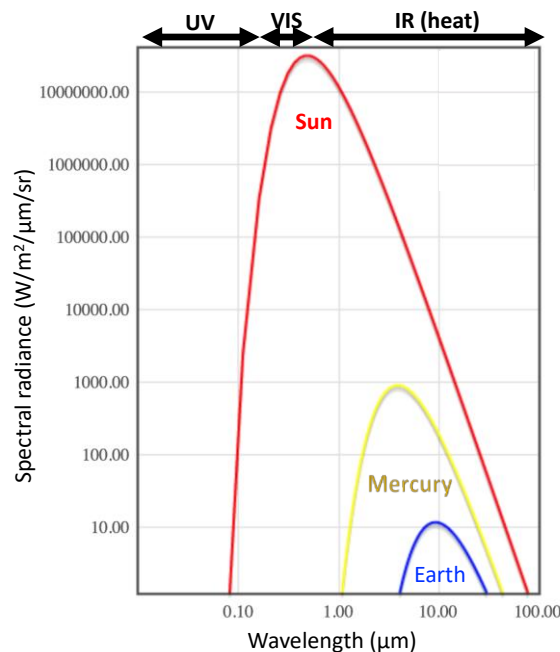


Figure 1.4. Plot shows the relation between the spectral radiance curves as a function of wavelength for Sun (5778 K), Mercury (700 K), and Earth (283 K) (derived from eq. 1). The plot shows that the emissivity peaks at visible-near infrared spectral region in the case of Sun, whereas the emissivity peaks at thermal infrared/mid-infrared spectral region in the case of Mercury and still a slightly farther region in case of Earth. In general, the emissivity peaks shift to shorter wavelengths for increasing temperatures. This knowledge is important while deciding the spectral range of the instrument aiming to map the emissivity of its targeted planet/system.

Emissivity is defined as the ratio of the energy emitted from a material to that of a blackbody (perfect emitter) at the same temperature and has unit less dimensions from 0 to 1 (Hapke, 2012, Bandfield and Rogers, 2019). For hot planetary surfaces such as Mercury and Venus, the emitted energy peaks at TIR spectral region (Fig. 1.4). The three diagnostic spectral features in the TIR emissivity spectrum that are commonly used for remote identification and characterization of silicate minerals include the Christiansen feature (CF), Reststrahlen bands (RBs), and the transparency feature (TFs). The CF position (wavelength at emissivity maximum) is an index of silica polymerization and therefore the amount of Si-O (Conel, 1969, Logan *et al.*, 1973, Cooper *et al.*, 2002, Donaldson Hanna *et al.*, 2012), RBs relate to fundamental vibration bonds due to stretching and bending modes of Si-O and its cations (Lyon, 1965, Conel, 1969, Hamilton, 2000) and TFs are the emissivity minima in the TIR spectrum caused by volume scattering of Si-O-Si bonds (Cooper *et al.*, 2002, Hapke, 2012). Therefore, understanding the TIR spectral evolution as a function of temperature will give direct evidence to the surface mineralogy and the physical properties.

1.1.2 FACTORS AFFECTING REFLECTANCE AND EMITTANCE SPECTROSCOPY

From remote sensing standpoint, the key intrinsic variables that affect the nature of the spectra and its absorption features are influenced by the abundance and oxidation state of transition metals (principally iron) in silicates, oxides, and sometimes sulfides (for Mercury) (Sprague *et al.*, 1995), the presence of opaque components such as ilmenites (in Moon) (Yang *et al.*, 2019) and carbon-bearing phases (possibly in Mercury) (Domingue *et al.*, 2014a, Trang *et al.*, 2017); and the extent of space weathering which could substantially modify the optical properties of the surface materials due to prolonged interaction with the space environment. Other factors that still affect the spectral shape includes the varying grain sizes of same mineral, differences in the viewing angles causing non-uniform phase angle of observation, and the slope/irregularity of the surface occupying the pixels (Okin and Painter, 2004, Helbert and Maturilli, 2009, Maturilli *et al.*, 2016a, Maturilli *et al.*, 2016b, Varatharajan *et al.*, 2019b). Though these factors affecting the spectra can be understood in a controlled environment, the real challenge comes in understanding the spectra can be addressed in two parts: 1. spectral behaviour of minerals in their related planetary environment and 2. understanding the mixture spectra containing more than one mineral.

The Fe-bearing minerals including oxides, olivine, pyroxene, and glasses creates crystal field absorptions near 0.85–1.05 μm wavelength when interacted with incident light and therefore can be effectively distinguished in the planetary surfaces containing Fe-bearing mineral phases such as Moon and Mars (Holsclaw *et al.*, 2010, Horgan *et al.*, 2014). However, for surfaces such as Mercury which possess less than 2.5 wt% Fe in the surface does not produce strong absorption features (McClintock *et al.*, 2008, Izenberg *et al.*, 2014, Varatharajan *et al.*, 2019c) and therefore make it difficult to understand the direct surface mineralogy through reflectance spectroscopy in the VNIR spectral region.

Opaque minerals within the pixels typically darken and flatten the reflectance spectrum of a mixture. Space weathering leads to formation of submicroscopic amorphous rims on regolith grains, which further contain nm-scale inclusions of metal or sulfides formed from impact-generated vapor and solar wind sputtering (Hapke *et al.*, 1975, Pieters and Englert, 1993, Hapke, 2001, Domingue *et al.*, 2014b). This further affects the nature of the silicate spectra by darkening and reddening (i.e., steepening the slope of reflectance with respect to wavelength) in the VNIR wavelengths (Pieters *et al.*, 1993, Fischer and Pieters, 1994, Taylor *et al.*, 2001) and brightening and bluing (i.e., reducing the slope) of the spectrum in the UV (Hendrix *et al.*, 2012, Hendrix *et al.*, 2016). Both opaque minerals and space weathering subdue mineralogical absorptions.

1.1.3 BUILDING PLANETARY SPECTRAL LIBRARY UNDER CONTROLLED LABORATORY CONDITIONS

In order to remotely map the surface mineralogy of a planetary surface such as Mercury, it is important to create a specialised high-resolution spectral library of various Mercury analogues unique for that planetary body under its extreme environmental conditions over a wide spectral range (Maturilli *et al.*, 2008, Maturilli *et al.*, 2016b, Maturilli *et al.*, 2017b, Maturilli *et al.*, 2018b, Varatharajan *et al.*, 2019a). This can be achieved by simulating the surface environment conditions in the controlled laboratory facility and fitting them to the spectrometer without compromising the sensitivity of the optics and the measurements. This section briefly introduces the Fourier Transform Infrared (FTIR) spectroscopy approach widely adapted by various spectroscopy laboratories including Planetary Spectroscopy Laboratory (see Chapter 3) and its capability to perform direct emissivity studies at extreme temperatures when fitted with an external emissivity chamber.

1.1.3.1 FOURIER TRANSFORM INFRARED (FTIR) SPECTROSCOPY APPROACH

In a traditional dispersive spectroscopy approach, a monochromatic light source of narrow wavelength spectral region irradiates the sample and its corresponding reflected light is measured (Hsu, 1997). On the other hand, FTIR spectroscopy uses a broadband beam source and therefore enables collection of high spectral resolution data over a wide spectral range based on the working principle of Michelson interferometer (Griffiths and De Haseth, 2007, Shakun *et al.*, 2017). The simple working principle of FTIR spectroscopy is outlined in Fig. 1.5 (Griffiths and De Haseth, 2007).

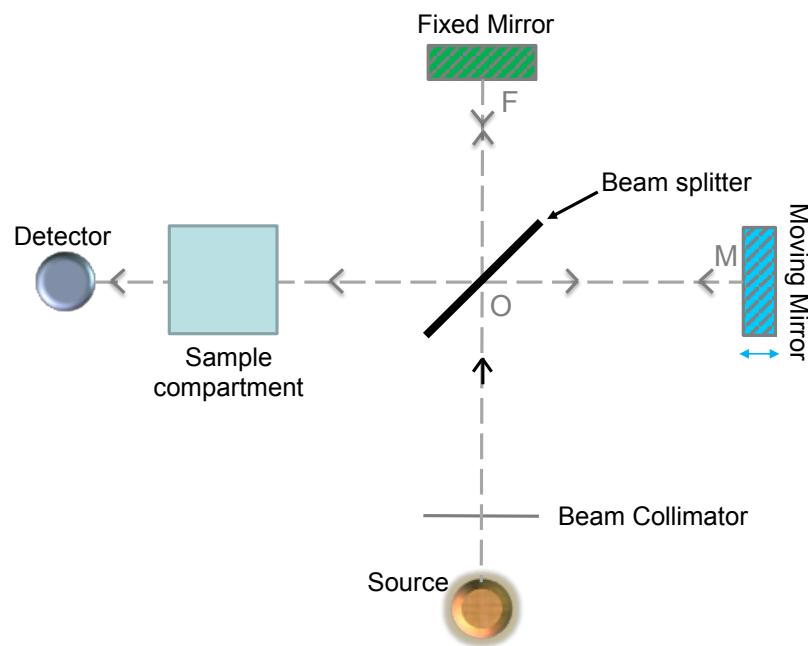


Figure 1.5. Simple outline of the working principle of FTIR spectrometer based on (Griffiths and De Haseth, 2007)

In FTIR spectroscopy, a broadband beam/light source having wide spectral frequencies is used to irradiate a sample at once. Before the collimated beam source hit the sample surface, it is first sent through the beam splitter which splits the light source to two halves. One half of the light source hits a fixed mirror (F) and the other half hits a moving mirror at constant velocity (M), and thus creating a path difference between the beams. When these two halves are now reflected back from their corresponding mirrors and then recombined, it creates an interference pattern. This interferogram is now sent to the sample and its corresponding reflected interferogram is sent to the detector. The full spectrum of the reflectance of the sample as a function of wavenumber is then obtained by applying Fourier

transform to the resulting compared spectra between the sample and the reference (Griffiths and De Haseth, 2007). Inside the sample compartment, the viewing angle of the interferogram can be adjusted such that the reflectance spectroscopy of various planetary analogues at wide spectral range (ultraviolet to far infrared) at varying phase angle of observations can be studied at very high spectral resolution (Maturilli *et al.*, 2018c).

By choosing the beam source of wide spectral range and its corresponding sensitive detectors, a FTIR spectrometer facilitates the flexible and dominant method of high-spectral-resolution laboratory spectroscopy.

The Planetary Spectroscopy Laboratory (PSL) at Department of Planetary Laboratories at the Institute of Planetary Research, German Aerospace Center (DLR), Berlin currently operates three Bruker 80V FTIR spectrometers which are fitted with external light sources of choice (UV-FIR) and their corresponding detectors. This facility therefore enables UV-FIR reflectance spectroscopy of planetary analogues at the spectral resolution of 4 cm^{-1} . The sample compartment at PSL is fitted with the Bruker A513 accessory which further allows to repeat the spectral measurements of the samples and references at varying viewing geometry. Chapter 3 elaborately discuss the capabilities of PSL facilities and Chapter 4 discusses the phase angle dependent UV-FIR spectroscopy of sulfides for both fresh and thermally weathered sulfides.

1.1.3.2 IMPORTANCE OF SIMULATED PLANETARY ENVIRONMENT CONDITIONS

In most remote-sensing measurements, absorptions bands can be detected only through their effects on the radiation that is thermally emitted by the planetary surface being studied (Hapke, 1993). Considering planet Mercury and its closeness to the sun over its geologic history, its surface has been repeatedly experienced extreme hot ($450 \text{ }^\circ\text{C}$; daytime) and extreme cold (-170°C ; nighttime) temperatures for every 176 days leading to thermally weathering (Soter and Ulrichs, 1967, Krotikov and Shchuko, 1975a). Mercury's 2:3 orbital resonance has the significant impact on the latitudinal and longitudinal dependence on the peak surface temperatures during Mercury days (Soter and Ulrichs, 1967, Krotikov and Shchuko, 1975a, Vasavada *et al.*, 1999, Bauch *et al.*, 2021). The slow rotation of the planet leads to local surface temperatures upto 450°C for about 88 days (Strom and Sprague, 2003). Therefore, Mercury surface experiences an extremely wide range of temperature variations

(-150°C to 450°C) at different latitudes and longitudes for such prolonged exposure time (Vasavada *et al.*, 1999, Bauch *et al.*, 2021) (Fig. 1.6).

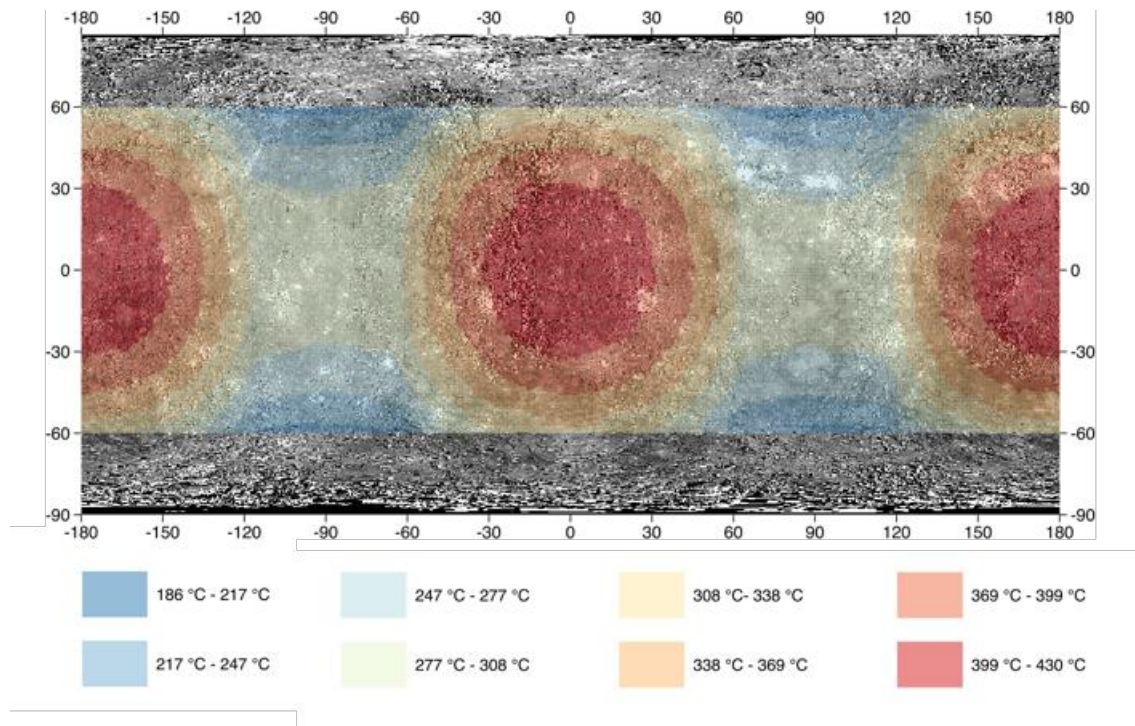


Figure 1.6. Extreme thermal environment of Mercury surface mapped from the data by (Bauch *et al.*, 2021).

Together with the lack of stabilizing atmosphere, these temperature variations significantly affect the crystal structure and density of minerals due to thermal expansion (Stangarone *et al.*, 2017). From a crystal structural point of view, these extreme change in temperatures within the mineral induces the variations of bond distances and angles which further changes the vibrational behaviour when reaching extreme temperatures and are closely related to the vibrational frequencies within the TIR spectral region (Chihara *et al.*, 2001, Koike *et al.*, 2003, Koike *et al.*, 2006, Helbert *et al.*, 2013b, Ferrari *et al.*, 2014, Maturilli *et al.*, 2014, Reitze *et al.*, 2017, Stangarone *et al.*, 2017, Varatharajan *et al.*, 2019a, Ferrari *et al.*, 2020).

In order to understand the spectral behaviour of the planetary analogues under such extreme surface environment conditions, one of the FTIR spectrometers at PSL is fitted with an external emissivity chamber which allows us to perform direct emissivity measurements of

the samples at extreme temperatures of Mercury under vacuum conditions (Chihara *et al.*, 2001, Koike *et al.*, 2003, Koike *et al.*, 2006, Helbert *et al.*, 2013b, Ferrari *et al.*, 2014, Maturilli *et al.*, 2014, Reitze *et al.*, 2017, Stangarone *et al.*, 2017, Varatharajan *et al.*, 2019a, Ferrari *et al.*, 2020). This facility enables us to demonstrate and understand the evolving spectral behaviour of silicates, sulfides, and graphites under simulated daytime surface conditions of Mercury which show significant TIR spectral signature changes under varying temperatures in vacuum (Helbert and Maturilli, 2009, Helbert *et al.*, 2013b, Maturilli *et al.*, 2019, Varatharajan *et al.*, 2019a, Varatharajan *et al.*, 2020b). These studies compel the importance of creating specialised spectral library under simulated planetary environment which will help in interpreting the remotely sensed TIR spectra. Chapters 4,5,6 discuss the samples, methods, and results of direct emissivity measurements of sulfides and silicates in the TIR spectral region under varying temperature environment of Mercury.

1.2. MERCURY AND ITS SURFACE EXPLORATION

Mercury, the smallest and the innermost of the terrestrial planets, is also the hottest planet among the airless bodies in the solar system (Mahoney, 2014). Understanding its formation and evolution are important to understand the formation of the solar system itself.

In the 1970s, Mariner 10 images provided the first closer look into the Mercury's heavily cratered plains and different geologic units distinguished by color differences (Hapke *et al.*, 1975). Over the next four decades telescopic reflectance spectra at ultraviolet (UV) through short-wave infrared (SWIR) wavelengths ($\sim 0.1\text{--}2.5\ \mu\text{m}$) revealed a featureless reflectance spectrum lacking evidence for absorptions due to ferrous iron in silicate minerals (e.g., (Warell *et al.*, 2009, Vernazza *et al.*, 2010) and references therein), though thermal emission spectra suggested the presence of various silicate phases (Sprague *et al.*, 1994, Sprague *et al.*, 1997, Cooper *et al.*, 2001, Sprague *et al.*, 2002, Sprague *et al.*, 2009).

The MErcury Surface, Space ENvironment, GEOchemistry, and Ranging (MESSENGER) mission is the first to orbit Mercury between 2011 and 2015 (Solomon *et al.*, 2001). MESSENGER carried seven scientific instruments out of which four instruments which includes Mercury Atmospheric and Surface Composition Spectrometer (MASCS) (McClintock and Lankton, 2007, Domingue *et al.*, 2019a, Domingue *et al.*, 2019b), Mercury Dual Imaging

System (MDIS) (Hawkins *et al.*, 2007, Denevi *et al.*, 2018), X-ray Spectrometer (XRS) (Schlemm *et al.*, 2007, Weider *et al.*, 2012), and Gamma-Ray and Neutron Spectrometer (GRNS) (Goldsten *et al.*, 2007, Lawrence *et al.*, 2017) are specifically sent to understand the surface chemistry and its mineralogy (Solomon *et al.*, 2001). The optical spectroscopy suite (MASCS, MDIS) onboard MESSENGER covered only the visible and near-infrared spectral range (Hawkins *et al.*, 2007, McClintock and Lankton, 2007, Denevi *et al.*, 2018, Domingue *et al.*, 2019a, Domingue *et al.*, 2019b). The most comprehensive UV through SWIR spectral measurements have been acquired by the MDIS wide-angle camera (WAC) and MASCS Visible and Infrared Spectrograph (VIRS) and Ultraviolet and Visible Spectrometer (UVVS) on the MESSENGER spacecraft. None of the spectral measurements obtained so far have shown silicate absorption bands in this spectral range due to the Fe-poor nature of the surface minerals (Izenberg *et al.*, 2014). This poses necessary challenges for direct identification of the surface mineralogy. On the other hand, new measurements by geochemistry suite (XRS, GRNS) of MESSENGER spacecraft suggest a mineralogy dominated by magnesium-rich orthopyroxene and feldspar (Namur and Charlier, 2017, Vander Kaaden *et al.*, 2017). However, direct identification of the surface mineralogy of Mercury is still missing.

1.2.1 ENIGMATIC MERCURY

1.2.1.1 THE ORIGIN

The Mercury's high uncompressed density (about 5.3 Kg/m³) and its largest core among all terrestrial planets is still mysterious (Mahoney, 2014). Mercury's high density is attributed to the abundance of Fe- and heavy siderophile elements in comparison to Si, Mg, and other lithophile elements (Mahoney, 2014). The metal-rich composition of Mercury can be either explained by the stripping of 64% of mass of the initially chondritic Mercury or the unknown nebular fractionation processes of the non-chondritic Mercury (Lewis, 1988, Benz *et al.*, 2008). The origin of Mercury is still "the least well-understood topic" (Chapman, 1988).

1.2.1.2 THE VOLATILE-RICH INTERIOR

MESSENGER data revealed the most unexpected multiple independent lines of evidence that Mercury's surface including its crust and possibly mantle are rich in volatiles (Blewett *et al.*, 2011, Blewett *et al.*, 2013, Xiao *et al.*, 2013, Goudge *et al.*, 2014, Thomas *et al.*,

2014a, Besse *et al.*, 2015, Vilas *et al.*, 2016). Understanding the nature and abundance of these volatiles is of fundamental importance for understanding the formation and evolution of Mercury. Detailed mapping of the nature and extent of these volatiles will help us to determine the distance from the Sun at which material accreted to form the proto-Mercury and its evolution to present day Mercury.

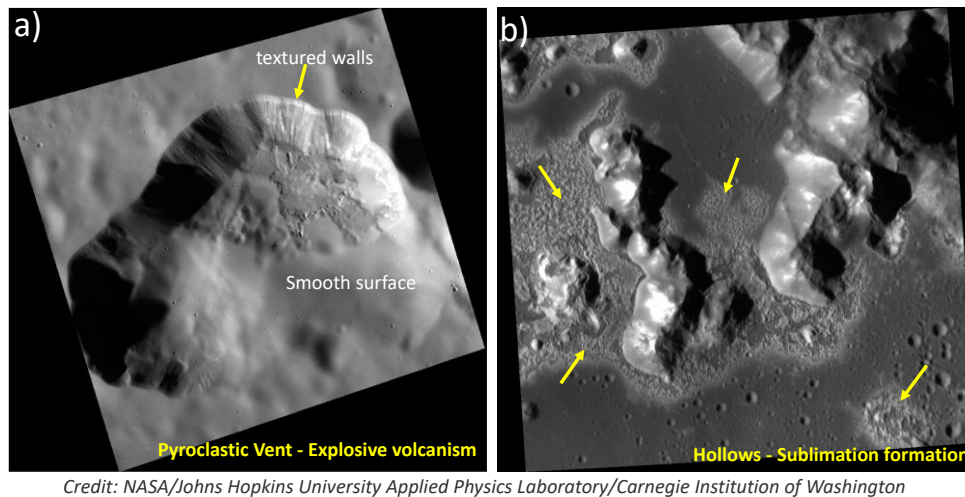


Figure 1.7. a) Pyroclastic vent named “Nathair Facula” situated at the north-east of Rachmaninoff Basin (35.84°N 64°E) representing the explosive volcanic event on Mercury. The image was taken by MDIS WAC (Image ID: 7866002) at the targeted color observation mode at spatial resolution 73 m/pixel. The image is ~55km across the diagonal acquired at phase angle of 87.7°. This high-resolution image shows the smooth surface which are blanketed by the very fine particles (volcanic ash) and the textured north-eastern walls indicating the downslope movement of the ejected material marked by yellow arrow. b) Hollows within the crater Eminescu (10.52°N 114.3°E) representing the volatile sublimation processes on Mercury surface. The image was taken by MDIS NAC (Image ID: 605799) at the spatial resolution of 24 m/pixel and the image is about 28 km wide at the phase angle of 50.4°. This high-resolution image shows the extensive formation of hollows, some of which are indicated by yellow arrows, on and surrounds the mountainous peak-ring.

The two most striking evidences of Mercury’s volatile-rich interior are obtained from the photogeologic observations by MDIS data;

a) The first line of evidence includes the evidences of explosive volcanic vents (Fig. 1.7a) in the form of non-circular holes of about 10 km size and 1 km depth (Kerber *et al.*, 2011, Besse *et al.*, 2015), called pyroclastic vents. These are usually characterised by a high albedo, spectrally red spot (a facula) and several tens of km across with a diffuse outer edge (Thomas

et al., 2014b). These explosive eruptions on this scale suggests the violent gaseous expansion of an abundant volatile (Kerber *et al.*, 2009).

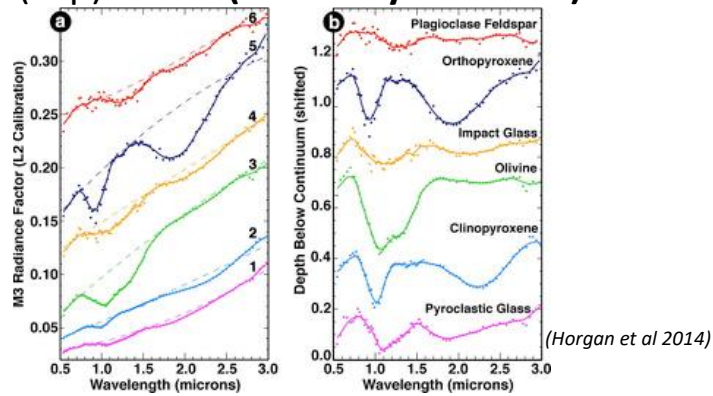
b) The second line of evidence includes the discovery of ‘hollows’ (Fig. 1.7b) which are characterised by their steep-sided, flat bottomed depressions 10-20 m deep from which 100 m to km wide patches of material have somehow been removed from the surface (Blewett *et al.*, 2013, Thomas *et al.*, 2014a). The suggested mechanisms for hollow formation include sublimation (Helbert *et al.*, 2013a), thermal desorption, photon-stimulated desorption, and sputtering, and all the proposed mechanisms conclude that whatever is being lost is not fully stable at present-day Mercury surface conditions and therefore indicating their volatile-rich nature. The first evidence of nature of hollow materials was reported by (Vilas *et al.*, 2016) which indicated the presence of CaS and MgS in the Dominici and Hopper hollows. The study used MDIS 8 band spectral datasets and compared the laboratory spectra of CaS and MgS measured at PSL for the interpretation.

The detailed mapping of the nature, abundance, and distribution of Mercury volatiles across the surface will not only help us to decipher the interior composition of Mercury but will also help us to constrain the nature of Mercury’s origin. Chapter 4 of this dissertation presents the specialised spectral library of seven sulphide minerals (Varatharajan *et al.*, 2019a), where the emissivity of each sulfides are measured as a function of temperature under vacuum to study the changing spectral nature under extreme thermal environment of Mercury. The reflectance measurements of the fresh and thermally weathered sulfides are also presented at wide spectral range and various phase angle combinations. This study will help the detailed mineralogy map of the hollows across Mercury surface.

1.2.1.3 SPECTRAL REFLECTANCE

Mercury is known for its extremely reduced nature. In contrast to lunar reflectance spectra (Fig. 1.8 top), which possess characteristic absorption bands, the spectral reflectance measurements by both MESSENGER MASCS (Izenberg *et al.*, 2014) and telescopic observation of Mercury (Warell *et al.*, 2009, Vernazza *et al.*, 2010) within the VIS-IR spectral region (0.3-1.5 μm) presents with a featureless red-sloped spectra (Fig. 1.8 bottom). This suggests that Mercury surface lacks the crystal-field absorptions which are caused by the presence of transition metals in silicate, principally iron.

(Top) Moon (Chandrayaan-1 M3)



(Bottom) Mercury (MESSENGER MASCS)

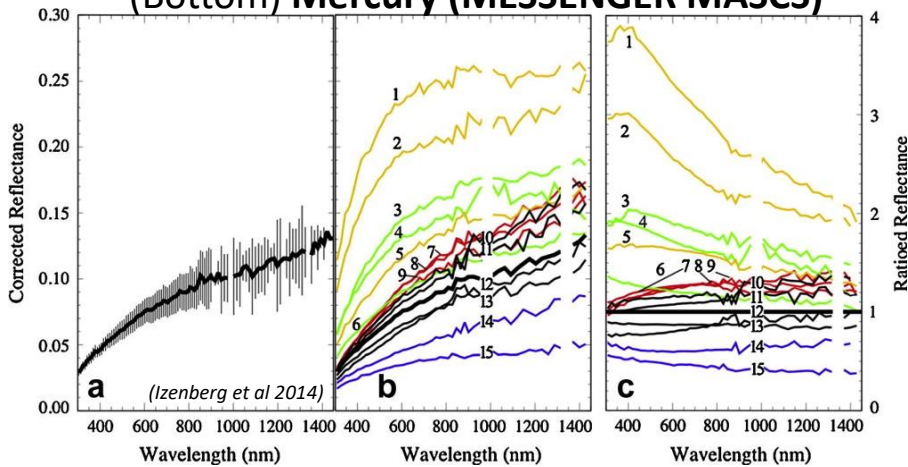


Figure 1.8. (Top) shows the lunar spectra (a) and its continuum removed counterpart (b) within the Aristarchus crater (23.7°N 47.4°W) obtained by Moon Mineralogy Mapper (M3) of Chandrayaan-1 mission represents the spectrally and mineralogically heterogeneous surface. The characteristic absorption bands and shapes near 1 μm and 2 μm spectral region due to the presence of Fe^{2+} the enables the mineral identification in the study by (Horgan *et al.*, 2014). (Bottom) shows the common featureless, red-sloped nature of Mercury spectra in the study by (Izenberg *et al.*, 2014) where (a) represents the average Mercury surface spectra, (b) and (c) represents the Mercury spectra across various surface units and its ratioed counterpart (individual spectra/average spectra) respectively which only show the differences in overall shape and slope without any indication of diagnostic absorption bands.

Various studies using MESSENGER data confirms the extreme depletion of Fe (in any form) on Mercury’s surface and deeper excavated materials (Izenberg *et al.*, 2014, Murchie *et al.*, 2015). The maximum wt% of Fe on Mercury surface is estimated to be 2.5wt% and could be present in the form of highly reduced phase as metal or sulfides (Trang *et al.*, 2017). These studies also suggest the silicate mineralogies of Mercury which possess insufficient Fe^{2+} to yield diagnostic features in the visible-infrared spectral region. However, the overall reflectance, spectral slope, and the scattering direction of MESSENGER reflectance spectra are

still used for insights to the elemental abundance and composition of the surface materials. For e.g., the UV spectral slope of the MDIS and MASCS spectra are used to characterise the hollow and pyroclastic materials on Mercury surface by various studies (Goudge *et al.*, 2014, Besse *et al.*, 2015, Besse *et al.*, 2020). On the whole, the surface composition of Mercury is still largely unknown.

This limitation of spectral reflectance of Mercury surface in visible-infrared spectral range strongly suggests for different spectral region that are capable of identifying the Fe-poor silicate mineralogy from the orbit. Chapter 6 presents the emissivity behaviour of such silicates studied under extreme Mercury daytime surface conditions as a function of temperature and under vacuum at 7-14 μm spectral region. This study will therefore support the global mineral mapping of Mercury surface for the first time by MERTIS instrument (Helbert *et al.*, 2010, Hiesinger *et al.*, 2010, Hiesinger *et al.*, 2020).

1.2.1.4 SURFACE MINERALOGY

Due to the insufficient capability of spectral reflectance of Mercury surface for mineral mapping, the data from the geochemistry suite (XRS, GRNS) onboard MESSENGER are used to derive indirect mineralogy of Mercury. Due to highly elliptical orbit of MESSENGER, the spatial coverage and resolution is highest at the northern hemisphere, this derived mineralogy is still limited only to the northern hermean hemisphere.

Previous studies (Peplowski *et al.*, 2015, Weider *et al.*, 2015, Vander Kaaden *et al.*, 2017) used XRS and GRNS data to identify nine major distinct geochemical terranes of Mercury (Fig. 1.9) which include, (1) a high-Mg region (HMR); (2) a sub-region of the HMR with the planet's highest Ca and S contents (HMR-CaS); (3) a subset of the northern volcanic plains (NP) with relatively high Mg content (NP-HMg); (4) a subset of the NP with relatively low Mg content (NP-LMg); (5) the Rachmaninoff basin (RB); (6) the planet's largest pyroclastic deposit, located northeast of the Rachmaninoff basin (PD); (7) high-Al regions southwest and southeast of the NP (HAI); (8) the smooth plains within the Caloris basin (CB); and (9) the intermediate terrain (IT), made up of intercrater plains and highly-cratered terrain.

Vander Kaaden *et al.* (2017) further used the normative mineralogy computation method to derive indirect mineralogy of these geochemical terrains based on the GRS, XRS and NS results and these are tabulated in Table 1.1.

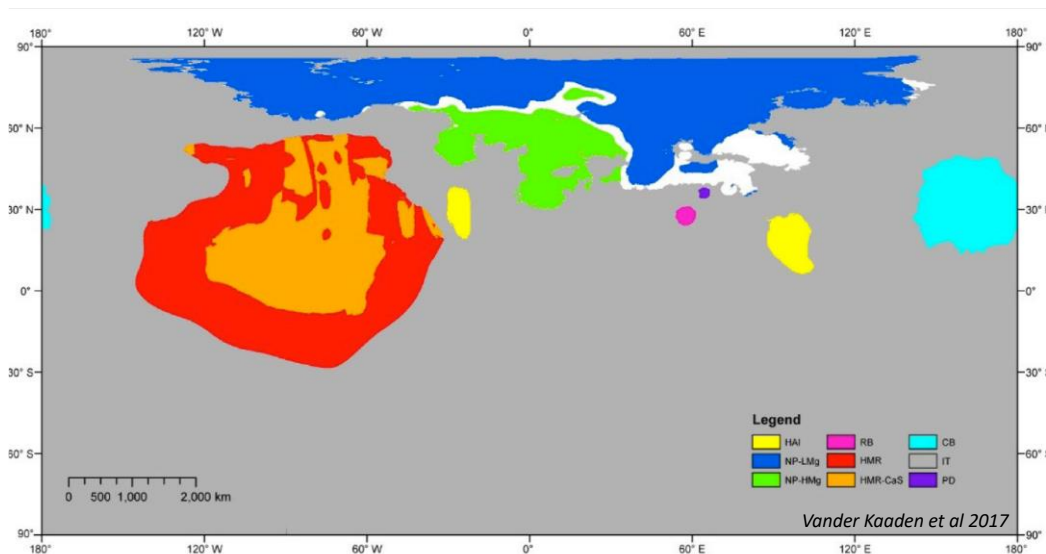


Figure 1.9 Geochemical terranes of Mercury taken from (Vander Kaaden *et al.*, 2017). Each color represents the distinct geochemical terrane mapped from the data obtained by XRS and GRNS spectrometer onboard MESSENGER mission.

On the other hand, Namur and Charlier (2017) took an experimental approach to derive the mineralogy of these geochemical units by taking advantage of the knowledge of the percentages of the oxides of the elemental abundances for each geochemical terrain using the results from the studies (Peplowski *et al.*, 2015, Weider *et al.*, 2015, Vander Kaaden *et al.*, 2017). The study (Namur and Charlier, 2017) conducted the magma crystallization experiments under reducing Mercury conditions representing each of these geochemically distinct terrains to derive a plausible silicate mineralogy for Mercury's surface and tabulated in Table 1.1 in comparison to normative mineralogy. Their study found that the oldest volcanic terrains (4.2-4.0 Ga), such as HMR and IT, are dominated by mafic minerals; where HMR is rich in forsterite and IT is comprised of forsterite, plagioclase, and enstatite. However, the youngest lavas (3.9-3.5 Ga), which mostly comprise the IT terrain, are dominated by plagioclase. Namur and Charlier (2017) suggest that Mercury's magma undergoes a temporal evolution where the source of the magma progressively gets shallower and the degree of mantle melting decreases over its geologic history.

Nevertheless, a direct mineralogic map of global Mercury, which characterizes the different mineralogical properties of the geochemical terrains, has yet to be constructed. Chapter 2 of this dissertation discusses the global multivariate analysis of MESSENGER MASCS

datasets and their relation to the various geochemical terranes of Mercury (Varatharajan *et al.*, 2020a). The study for the first time spectrally differentiates the NVP-LMg and NVP-HMg geochemical terranes using principal component analysis (PCA) approach.

Table 1.1 Comparison between experimental and normative mineralogy of various geochemical units of Mercury from MESSENGER datasets

Geochemical Terranes ^a	(Experimental) Silicate Mineralogy ^b					Normative Mineralogy ^a in wt%			
	volcanic	Basement (%)				Plg	Dominant pyx	Ol	sulfides
		Plg	Fo	Di	En				
NVP-LMg	dominantly Plg in addition to Fo and Di	>50	10-15	>15	-	>50	Hyp+Diop	<2	~4
NVP-HMg						<50	Hyp	~11	~4
HMR	May contain only Fo crystals	<40	>25	>20	<15	<50	Diop	~27	>5
HMR-CaS	-	-				<50	Diop	>30	~6.25
IT	Fo or Fo+Di	>45	-	-	>25	>50	Hyp	<2	~4
CB	-	>60	sub-equal amounts			>50	Hyp	-	~3.14
RB	NA	NA				<50	Diop	~24	>5
PD	NA	NA				<50	Diop	~29	~1.56
HAI – West	NA	NA				>50	Hyp	-	~4
HAI – East	NA	NA							

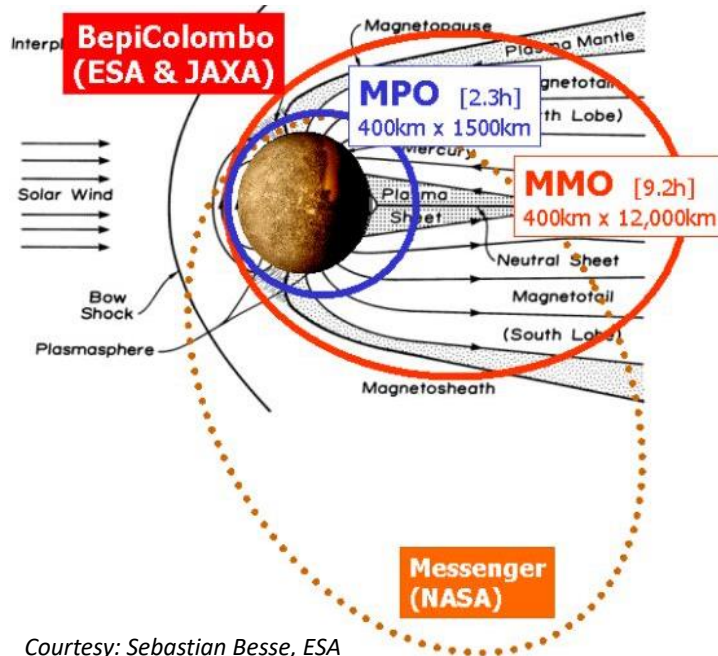
^aGeochemical terranes of Mercury surface and its normative mineralogy (Vander Kaaden *et al.*, 2017).

^bSilicate mineralogy derived from geochemistry laboratory experiments (Namur and Charlier, 2017)

1.2.2 BEPICOLOMBO AND ITS SPECTROMETERS FOR DIRECT SURFACE MINERALOGY STUDIES

BepiColombo is the second orbiter to Mercury which was launched on Oct 20, 2018 by European Space Agency (ESA) and Japanese Space Agency (JAXA). BepiColombo is known for its twin-satellite system carried by the Mercury Transfer Module (MTM) to Mercury. The twin satellites include Mercury Planetary Orbiter (MPO) by ESA and Mercury Magnetospheric Orbiter (MMO) by JAXA. Together BepiColombo has a larger and competent suite of instruments relevant for determination of the topographic, physical, chemical and mineralogical properties of Mercury's surface compared to MESSENGER spacecraft. Unlike MESSENGER which mapped Mercury surface at a highly elliptical angle and larger and varying phase angles (~80°), BepiColombo will make uniformly resolved observations in a near-

circular orbit and therefore mapping both northern and southern hemispheres at similar spatial resolution for the first time at nadir observations (phase angles $<20^\circ$) (Fig. 1.10).



Courtesy: Sebastian Besse, ESA

Figure 1.10. The relationship between MESSENGER and BepiColombo orbits for MPO and MMO. Source: <https://www2.mps.mpg.de/en/projekte/bepicolombo/>

This unique opportunity therefore offers the complete global mapping of Mercury at higher spatial resolution. On April 9th 2020, BepiColombo completed its first flyby with Moon and performed the first flyby with Venus on October 15th 2020.

BepiColombo will provide us with the first global mineralogical mapping of the Mercury surface which will be enabled by Mercury Radiometer and Thermal Imaging Spectrometer (MERTIS) payload onboard MPO of BepiColombo (Hiesinger *et al.*, 2010, Hiesinger *et al.*, 2020). MERTIS is the first hyperspectral imaging spectrometer ever flown to Mercury that will map the emissivity and the temperature of the surface in the thermal infrared (TIR) spectral region. MERTIS combines an imaging spectrometer covering the wavelength range from 7-14 μm mapping the surface mineralogy at spectral resolution of 90 nm (78 spectral channels) and spatial resolution of 500 m/pix, with a radiometer covering the wavelength range from 7-40 μm mapping the temperature and physical properties of the

surface at 2 km/pixel spatial resolution. Unlike visible-infrared spectral region where the diagnostic spectral features are dominated by the presence of transition metals like Fe and Ti, the TIR spectral region is influenced by the presence and the nature of Si-O bonds within the crystal lattice of the silicate minerals. Chapter 6 of this dissertation discusses the emissivity spectra of 10 Fe-poor silicate minerals belonging to five different families (olivine, pyroxene, plagioclase feldspar, K-feldspar, and feldspathoid) as a function of temperature under vacuum support MERTIS data analysis. The emissivity spectra and their spectral parameter plot discussed in the Chapter 6 shows that MERTIS can distinctly characterise the direct silicate mineralogy of Mercury due to the diagnostic spectral features within 7-14 μm spectral region. Chapter 4 of this dissertation further presents the emissivity behaviour of various sulfides under Mercury daytime surface conditions and shows that MERTIS can unique identify the sulphide mineralogies. The detailed description of MERTIS instrument and its first in-flight calibration results are discussed in Chapter 7.

MPO also carries a visible–near-infrared imaging spectrometer (VIHI) of Spectrometer and Imagers for MPO BepiColombo – Integrated Observatory SYStem (SIMBIO-SYS) which will map the surface mineralogy of Mercury in spectral range of 0.4-2 μm at spectral resolution of 6.25 nm (256 spectral channels) and spatial resolution of 100-375 m/pixel (Flamini *et al.*, 2010). Since spectral region beyond 1.5 μm is highly dominated by emissivity for Mercury daytime surface temperatures, the direct temperature measurement by MERTIS will support the thermal correction studies of SIMBIOSYS-VIHI instrument for spectral region beyond 1.45 μm .

By combining the direct measurements of the visible-near-infrared and emissivity measurements as a function of temperature from the orbit and the laboratory measurements of extensive Mercury analogues under the extreme environmental conditions of Mercury, BepiColombo will give the first insight to the crustal and mantle mineralogy of Mercury and its evolution over geologic history. In the recent publication by (Rothery *et al.*, 2020) on “Rationale for BepiColombo Studies of Mercury’s Surface and Composition” in “Space Science Reviews”, the detailed capabilities of the BepiColombo surface science is explained, in which I am one of the co-authors and I contributed text and figures related to PSL and emissivity studies of Mercury analogues under extreme environmental conditions within this publication.

1.3. SCOPE OF THIS THESIS

The work presented here was carried out as part of the MERTIS science onboard Bepicolombo mission to Mercury. The main objective of this PhD thesis is to constrain our understanding of the crustal and mantle mineralogy of Mercury through orbital spectroscopy of past and future missions. The major foundation of the thesis is focussed on the laboratory investigation of the reflectance and emissivity of various Mercury analogues which enable by their detection from the orbit by past and future missions. The main contribution of the thesis is highlighted in creating the unique and specialised temperature-dependent spectral library in the thermal-infrared (7-14 μm) spectral region of 17 Mercury analogues belonging to sulfides (7 minerals) and silicates (10 minerals belonging to olivines, pyroxenes, plagioclases, K-feldspars, feldspathoids). The thesis further evaluates the global multivariate spectral analysis of the existing MESSENGER MASCS datasets to constrain the global spectral diversity of the Mercury surface and its relation to the geochemical terrains constrained by XRS and GRNS instrument onboard MESSENGER. The results from this thesis supports the spectroscopy and surface science of Mercury from the data obtained by MERTIS and SIMBIOSYS-VIHI instrument onboard BepiColombo mission and MASCS and MDIS instrument onboard MESSENGER mission.

This work is a cumulative dissertation and the core of the dissertation includes six manuscripts. Out of six, one manuscript is published in peer reviewed journal (Chapter 4), two manuscripts are published in peer-reviewed conference proceedings (Chapter 3 and Chapter 7), one manuscript is under revision (Chapter 2), and two manuscripts are under review (Chapter 5 and Chapter 6). The included manuscripts correspond to the final, submitted versions prior to corresponding publications. For this dissertation the figures were re-positioned to correspond to the published, type-set versions of the articles. The references of all the manuscripts are attached to the end of each corresponding chapters, rather than listed at the end of the dissertation. This PhD work is funded as a part of DLR-DAAD PhD research fellowship programme.

Chapter 2 is currently under revision as “Global Multivariate Spectral Analysis of Mercury and the Identification of Geochemical Terrains: Derived from the MASCS Spectrometer onboard NASA’s MESSENGER Mission” in “Journal of Geophysical Research:

Planets” and its preprint is published in “Earth and Space Science Open Archive (ESSOAr)” (Varatharajan *et al.*, 2020a). This work presents the results from global multivariate spectral analyses of MESSENGER MASCS datasets by applying techniques include standard spectral parameter maps, k-means clustering, and principal component analysis (PCA) to spectrally characterize Mercury’s surface. I was the first author, wrote the article, wrote the program, performed, analysed, and interpreted all the results of the MASCS spectral analysis discussed in the manuscript. Python language is used for data analysis and visualisation. Mario D’Amore created the global MASCS datacube which is used in this manuscript. Jörn Helbert, Mario D’Amore, Deborah Domingue, and Alessandro Maturilli contributed constructive reviews to the manuscript prior to submission.

Chapter 3 is published as “The Planetary Spectroscopy Laboratory (PSL) – wide spectral range, wider sample temperature range” in “Proc. international society for optics and photonics (SPIE), Infrared Remote Sensing and Instrumentation XXVI” (Maturilli *et al.*, 2018c). This manuscript details the wide range of capabilities of Planetary Spectroscopy Laboratory (PSL) that enables the creation of the spectral library enabled by reflectance, transmission and emissivity measurements. PSL offer the unique opportunity to use the same spectrometer to perform spectroscopy under vacuum (or purged air), covering the whole spectral range from UV (0.2 μm) to the FIR (200 μm and above), and for sample temperature from 70K to 1000K. PSL’s is unique for its planetary emissivity chamber that allow us to study the emissivity of the planetary analogues under extreme environment conditions (100°C to 500°C) such as Mercury as a function of temperature. The resulting thermally weathered samples at the end of the emissivity measurements are further used for reflectance measurements for a wide spectral range (0.25 – 200 μm) and phase angle (13° - 80°) conditions. The results obtained by PSL is presented and discussed in the chapters 4, 5, and 6 of this dissertation. The first author of this manuscript is Alessandro Maturilli. My contribution as a co-author includes the contribution related to the emissivity and the reflectance capabilities of the PSL discussed in this chapter.

Chapter 4 is published as “Spectral Behavior of Sulfides in Simulated Daytime Surface Conditions of Mercury: Supporting past (MESSENGER) and future missions (BepiColombo)” in “Earth and Planetary Science Letters” (Varatharajan *et al.*, 2019a). This work presents the emissivity and reflectance spectral library of 7 synthetic sulfides includes MgS, FeS, CaS, CrS,

TiS, NaS, and MnS. For each sample, the emissivity measurements are performed in the thermal infrared range (TIR: ~7-14 μm) for sample temperatures from 100°C-500°C, covering the daytime temperature cycle on Mercury's surface. In addition, for each sample, the spectral reflectance of fresh and thermally processed sulfides are measured over a wide spectral range (0.2-100 μm) and at four different phase angles, 26°, 40°, 60°, 80°. The change in spectral behaviour of these sulfides under extreme thermal environment of Mercury is discussed in detail in this chapter. I was the first author, wrote the article, prepared the sample cups ready for measurements, performed the laboratory measurements for both emissivity and reflectance study, derived spectral parameters, and interpreted the results. Alessandro Maturilli and Jörn Helbert bought the synthetic samples used in this study. Jörn Helbert, Alessandro Maturilli, Harald Hiesinger, and Giulia Alemanno are involved with constructive reviews to the manuscript prior to submission. The importance of this work is weighted by its capability to map the distribution, abundance, and the nature of sulfides in and around hollows and pyroclastic deposits of Mercury surface. The results from this study is used in the recently published work on "Spectral Properties and Physical Extent of Pyroclastic Deposits on Mercury: Variability Within Selected Deposits and Implications for Explosive Volcanism" in "Journal of Geophysical Research: Planets" (Besse *et al.*, 2020) in which I am one of the co-authors and contributed the sulfide spectra and its derived spectral parameters presented in this specific study.

Chapter 5 is currently under review as "Thermal Stability and Emissivity Behavior (7-14 μm) of Ca-Sulfides under Simulated Daytime Surface Conditions for Multiple Mercury days: Implications for the formation of hollows and CaS detection by MERTIS onboard the BepiColombo mission" with "Earth and Planetary Science Letters". Chapter 4 showed that CaS sample cup possesses the most stable spectral behavior compared to its counterparts when heating upto 500 °C under vacuum for one Mercury. This work in Chapter 5 therefore tests the stability of the thermal behaviour of CaS while heating the sample cup for multiple Mercury daytime surface conditions. The importance of this work presents the stability of CaS under the extreme thermal environmental conditions and therefore acting as an important tracer of other sulfides those might be lost in the sublimation process. The spectral emissivity result therefore supports detection of CaS among hollows and pyroclasts in MERTIS datasets. I was the first author, wrote the article, prepared the sample cups ready for measurements,

performed the emissivity measurements for four Mercury days, derived spectral parameters, and interpreted the results. Claudia Stangarone and Sergio Speziale performed the XRD measurements of the fresh and thermally weathered CaS samples presented in this study. Jörn Helbert, Alessandro Maturilli, Harald Hiesinger, and Iris Weber contributed the constructive reviews to the manuscript prior to submission. Karin E. Bauch contributed globally modelled surface temperature of Mercury used in the study.

Chapter 6 is submitted as “Thermal Infrared Spectroscopy (7-14 μm) of Silicates under Simulated Mercury Daytime Surface Conditions and their Detection: Supporting MERTIS onboard the BepiColombo Mission” with “Icarus”. This work presents the extensive emissivity spectral library of finely grained (<25 μm grain size) silicate analogues of Mercury measured under extreme daytime conditions of Mercury surface. The emissivity spectra of ten terrestrial silicate minerals studied include one olivine (forsterite), two pyroxenes (diopside, hypersthene), four plagioclase feldspars (anorthite, labradorite, andesine, oligoclase), one K-feldspar (microcline), and one feldspathoid (nepheline) for five temperatures (100 °C, 200 °C, 300 °C, 400 °C, and 500 °C) under vacuum. The study further presents the relation between the spectral parameters such as Christiansen Feature (CF) position, first Reststrahlen band (RB1) position, RB1 emissivity, and RB spectral contrast and its temperature for all the silicates for their effective survey the Mercury surface mineralogy with MERTIS datasets from the orbit. The study introduces CF vs RB1 plot which can be used to effectively identify olivine, pyroxenes, and plagioclase feldspars and enable a quick first order surface mineral identification in MERTIS data and ground-based telescopic observations in the TIR spectral region. I was the first author, wrote the article, prepared the sample cups ready for measurements (except for forsterite and enstatite), performed the emissivity measurements (except for forsterite and enstatite), derived spectral parameters, and interpreted the results. Alessandro Maturilli and Jörn Helbert collected the samples used in this study. Claudia Stangarone performed the emissivity measurements of forsterite and enstatite as a part of her thesis (Stangarone, 2017). Claudia Stangarone and Franziska D.H. Wilke performed the EPMA measurements of the fresh silicates for their chemical characterisation which is presented in this study. Jörn Helbert, Alessandro Maturilli, Harald Hiesinger, and Iris Weber contributed the constructive reviews to the manuscript prior to submission.

Chapter 7 is published as “The mercury radiometer and thermal infrared imaging spectrometer (MERTIS) onboard BepiColombo: first inflight calibration results” in “Proc. international society for optics and photonics (SPIE), Infrared Remote Sensing and Instrumentation XXVII” (D'Amore *et al.*, 2019). This chapter summarizes the MERTIS instrument specifications and capabilities and also reports the first inflight calibration and performance results during the Near-Earth Commissioning Phase of BepiColombo mission. The study revealed no performance loss or misalignment and therefore promising the desired scientific results during the flybys of the Moon and Venus during the transit to Mercury. Mario D'Amore is the first author and wrote the manuscript. I am the co-author and contributed in the Quick Look Analysis of the first data of MERTIS which is used in this study. Python language is used for the analysis presented in this study. I am also Co-Investigator of the MERTIS instrument since May 2018.

The final chapter 8 summarizes the results of the six studies and presents the conclusions of this thesis.

GLOBAL MULTIVARIATE SPECTRAL ANALYSIS OF MERCURY AND THE IDENTIFICATION OF GEOCHEMICAL TERRAINS: DERIVED FROM THE MASCS SPECTROMETER ONBOARD NASA'S MESSENGER MISSION

I. Varatharajan^{1,2}, M. D'Amore¹, D. L. Domingue³, J. Helbert¹, and A. Maturilli¹

¹*Department of Planetary Laboratories, Institute of Planetary Research, German Aerospace Center (DLR), Berlin, Germany,* ²*Institute of Geological Sciences, Freie University (FU) Berlin, Germany,* ³*Planetary Science Institute, Tucson AZ, 85719, USA.*

Under Revision in Journal of Geophysical Research-Planets (JGR-Planets)

Preprint available at Earth and Space Science Open Archive (ESSOAr)

DOI: <https://doi.org/10.1002/essoar.10501760.1>

The author contribution is explained in the [Section 1.3](#).

KEY POINTS

- K-Means clustering of global MASCS hyperspectral datacube suggests that most of Mercury's surface fall into three contiguous regions.
- Principal component analysis (PCA) of MASCS datacube distinguishes the northern volcanic plains as consisting of high-Mg and low-Mg terranes.
- The 6th component of a Principal Component Analysis of MASCS data correlates with physical properties of Mercury surface associated with fine-grained, freshly exposed materials.

2.1 ABSTRACT

The visible-infrared spectra of Mercury's surface show little variation, displaying no distinct spectral features except for the possible spectral identification of sulfide within the hollows (Vilas et al. 2016). It is essential therefore to define and map any subtle spectral heterogeneity across Mercury's surface and to correlate these differences where possible to geomorphological features, such as impact craters, volcanic vents, and tectonic features. The Mercury Atmospheric and Surface and Composition Spectrometer (MASCS) instrument onboard MESSENGER spacecraft is the only hyperspectral reflectance spectrometer to date that has mapped Mercury's surface in the wavelength range 300 nm - 1450 nm. The limitation of MASCS is that it's a point spectrometer that mapped Mercury's surface at non-uniform spatial scale. In this study, we resampled the global MASCS hyperspectral dataset to a uniform equal-angular resolution of 1 pixel per degree. This enabled us to perform global multivariate analyses, including standard spectral parameter maps, k-means clustering, and principal component analysis (PCA) to spectrally characterize Mercury's surface. As the result of the PCA technique, the study for the first time presents the MASCS spectral heterogeneity map across Mercury correlating to both chemical and physical properties of the surface and also presents the spectral properties of the various geochemical terranes. The resulting map enables us to identify surface units based on grain size, the presence of amorphous materials, and space-weathering associated alterations. For the first time, we show that MASCS datasets effectively differentiate between the two northern plains' geochemical regions; the high-Mg and low-Mg terranes. This global spectral heterogeneity map derived from uniform equal-angular resolution MASCS datasets are a baseline for future investigation of the surface of Mercury with the MERTIS and SIMBIO-SYS/VIHI datasets of BepiColombo at higher spatial resolution and with a significantly wider spectral coverage.

2.2 INTRODUCTION

The MErcury Surface, Space ENvironment, GEochemistry, and Ranging (MESSENGER) mission was the first spacecraft to orbit Mercury. Over its 4 years at Mercury, beginning with its orbit insertion in 2011 (Solomon *et al.*, 2001), the instruments onboard this spacecraft globally mapped the planet. Among the seven scientific instrument suites, MESSENGER carried three spectrometers and one camera system. These included an X-Ray Spectrometer (XRS), a Gamma-Ray and Neutron Spectrometer (GRNS), the Mercury Atmospheric and Surface Composition Spectrometer (MASCS), and the Mercury Dual Imaging System (MDIS), all of which mapped the surface chemical and mineralogical properties of Mercury from 2011-2015.

The MDIS camera and the MASCS spectrometer are the only two instrument suites to have globally mapped Mercury's surface spectral characteristics. MDIS is comprised of two imaging cameras; the Narrow Angle Camera (NAC) that acquired monochrome (0.75 μm) data at a resolution of $\sim 200\text{-}500$ m/pixel and the Wide Angle Camera (WAC) that acquired global 8-channel multispectral datasets in the spectral range of 0.4-1 μm at the spatial resolution of ~ 5 km/pixel (Hawkins *et al.*, 2007). MASCS is a hyperspectral point spectrometer suite which consists of a small Cassegrain telescope with an aperture that simultaneously feeds the incoming reflected light from the surface to an Ultraviolet and Visible Spectrometer (UVVIS) and a Visible and Infrared Spectro-graph (VIRS). UVVIS mapped the surface at 0.115-0.6 μm at 1 nm spectral resolution. VIRS consists of two separate channels, one in the visible (0.3-1.05 μm) and another in the near-infrared (NIR: 0.85–1.45 μm) that mapped the surface at 5 nm spectral resolution (McClintock and Lankton, 2007). The elliptical orbit and spacecraft pointing constraints resulted in MASCS mapping the surface at dynamically varying spatial resolutions (100m – 7.5km) and high phase angles ($>80^\circ$); complicating the global hyperspectral characterization of Mercury at a uniform scale.

Global multispectral MDIS data reveals three areally dominant spectral units; low-reflectance material (LRM), moderate-to-high reflectance smooth plains (HRP), and spectrally intermediate terrane (IT) (Robinson *et al.*, 2008). HRP and IT terranes can be identified by a low reflectance, red-sloped, featureless spectrum suggesting the presence of iron-poor silicate minerals, which is supported by ground-based telescope measurements (Vilas and

McCord, 1976, McCord and Clark, 1979, Vilas *et al.*, 1984, Izenberg *et al.*, 2014). The absence of a 1- μm crystal-field absorption feature due to ferrous iron in silicates suggests the presence of 0.1-1 wt% of iron in the crustal silicates of Mercury (Lucey and Riner, 2011, Izenberg *et al.*, 2014, Murchie *et al.*, 2015). However, LRM exhibits a 600 nm absorption feature that seems to correlate (Murchie *et al.*, 2015, Klima *et al.*, 2018) with graphite abundance (Peplowski *et al.*, 2016) hinting at a carbon-bearing crust. In addition, the spectra of Mercury's hollows units suggest the presence of sulfides including magnesium-sulfides and calcium-sulfides (Helbert *et al.*, 2013a, Vilas *et al.*, 2016).

On the other hand, the geochemistry instrument suite (GRS, XRS, NS) onboard MESSENGER identified nine major geochemical terranes (Fig. 2.1) characterizing the chemical makeup of Mercury's surface (Vander Kaaden *et al.*, 2017). Due to the highly elliptical polar orbit of MESSENGER, the spatial coverage and resolution is highest at the northern hemisphere and that further affects the identification and distribution of these geochemical terranes. These geochemical terranes include: (1) a high-Mg region (HMR); (2) a sub-region of the HMR with the planet's highest Ca and S contents (HMR-CaS); (3) a subset of the northern volcanic plains (NP) with relatively high Mg content (NP-HMg); (4) a subset of the NP with relatively low Mg content (NP-LMg); (5) the Rachmaninoff basin (RB); (6) the planet's largest pyroclastic deposit, located northeast of the Rachmaninoff basin (PD); (7) high-Al regions southwest and southeast of the NP (HAI); (8) the smooth plains within the Caloris basin (CB); and (9) the intermediate terrane (IT), made up of intercrater plains and highly-cratered terrane. Vander Kaaden *et al.* (2017) also used the normative mineralogy computation method to derive indirect mineralogy of these geochemical terranes based on the GRS, XRS and NS results and these are tabulated in Table 2.1.

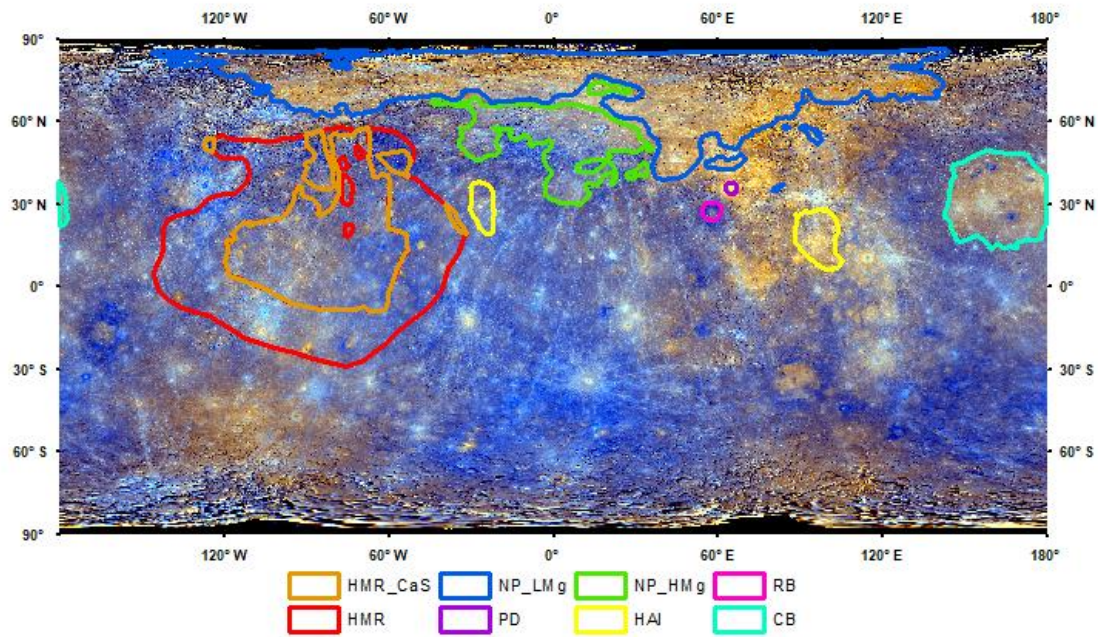


Figure 2.1. MDIS enhanced global color mosaic by Domingue et al. (2015) overlaid by the geochemical terranes mapped by (Vander Kaaden et al., 2017).

Namur and Charlier (2017) conducted magma crystallization experiments under reducing Mercury conditions for these geochemically distinct terranes (Peplowski *et al.*, 2015, Weider *et al.*, 2015, Vander Kaaden *et al.*, 2017) to derive a plausible silicate mineralogy for Mercury's surface. Their study found that the oldest volcanic terranes (4.2-4.0 Ga), such as HMR and IT, are dominated by mafic minerals; where HMR is rich in forsterite and IT is comprised of forsterite, plagioclase, and enstatite. However, the youngest lavas (3.9-3.5 Ga), which mostly comprise the IT terrane, are dominated by plagioclase. Namur and Charlier (2017) suggest that Mercury's magma undergoes a temporal evolution where the source of the magma progressively gets shallower and the degree of mantle melting decreases over its geologic history.

Nevertheless, a global mineralogic map of Mercury, which characterizes the different mineralogical properties of the geochemical terranes, has yet to be constructed due to the absence of diagnostic absorption features, such as those attributable to Fe²⁺-poor and Ti-poor minerals. Therefore, the spectroscopic and mineralogical properties of the distinct geochemical terranes on Mercury's surface have yet to be fully characterized.

It is therefore essential to examine the global variation of spectral properties, mainly as a function of geomorphological and geochemical terranes. Spectral analysis from the global coverage of Mercury's surface can characterize the minor variations corresponding to such spectral characteristics as albedo, slope, absorptions, and spectral components indicating the presence of opaques and glasses or space-weathering products.

With the availability of new and revised photometrically calibrated MASCS datasets (PDS MESSENGER Release 16 released on May 12, 2017), which involves radiance calibration, correction for viewing geometry and phase dependence, and photometric standardization of derived reflectance spectra (Izenberg *et al.*, 2014, Domingue *et al.*, 2019b, Domingue *et al.*, 2019a), it is now possible to conduct global multivariate analysis and derive global spectral parameter maps of Mercury. MASCS higher spectral resolution of 5 nm over more than 185 spectral bands is capable of resolving more subtle spectral variations than the 8-channel MDIS data.

In this study, we present the MASCS global hyperspectral datacube at 1 pixel/degree (42.58 km/pixel spatial resolution at equator) equal angular resolution (Section 2.3). We first examined standard spectral parameter maps, such as the uv-downturn position and the visible spectral slope (Section 2.4). We then applied an unsupervised clustering algorithm (Section 2.5.1) and Principal Component Analysis (PCA) (Section 2.5.2) to further investigate the global spectral heterogeneity across Mercury's surface. Finally, we compare in Section 2.7.1 the results obtained from the statistical analysis techniques in relationship to the various geochemical and geomorphological units.

The results and methodology from this study will be useful for analyzing the visible–near-infrared imaging spectrometer (VIHI) datasets of the Spectrometer and Imagers for Mercury Planetary Orbiter (MPO) BepiColombo – Integrated Observatory SYStem (SIMBIOSYS) onboard ESA/JAXA's BepiColombo mission. The mission launched on October 20, 2018 and is currently enroute to Mercury. VIHI will map the surface mineralogy in the spectral range of 0.4–2 μ m at a spectral resolution of 6.25nm and a spatial resolution of 100–375m/pixel (Flamini *et al.*, 2010), therefore enabling a higher spatial resolution analysis over a larger spectral range with a higher spectral resolution. In addition, BepiColombo's Mercury Radiometer and Thermal Imaging Spectrometer (MERTIS) will map the surface at a spatial resolution of 500 m/pixel over the 7–14 μ m spectral region (Hiesinger *et al.*, 2010, Hiesinger

et al., 2020). MERTIS observations will provide direct information on the abundance and nature of Si-O bonds within the bulk silicate mineralogy in addition to characterizing sulfide mineralogies (Maturilli *et al.*, 2017b, Varatharajan *et al.*, 2019a).

2.3 CREATION OF GLOBAL MASCS HYPERSPECTRAL CUBE

For the creation of the global spectral parameter maps, we first prepared a global hyperspectral datacube image made from the radiometrically calibrated (Holsclaw *et al.*, 2010) (Holsclaw *et al.*, 2010) and photometrically standardized (Domingue *et al.*, 2019a, Domingue *et al.*, 2019b) MASCS VIRS reflectance spectra which is corrected for instrument and radiance calibration, viewing geometry, phase dependence, and photometric normalisation of derived reflectance spectra (Holsclaw *et al.*, 2010, Izenberg *et al.*, 2014, Domingue *et al.*, 2019b, Domingue *et al.*, 2019a). We restricted our analysis to the VIS detector (0.3-1.05 μm) observations of the VIRS, because the NIR detector measurements show a lower signal-to-noise (SNR) ratio, which can influence the data classification in an unpredictable manner. To create the global hyperspectral map, we included VIS spectra collected between April 2011 and December 2013 (~4 million spectra). We excluded data with extreme observing geometries by limiting the observations to those with phase angles less than 85° . A side effect of this data selection is a reduction in the latitudinal coverage to within $\pm 80^\circ\text{N}$ and the exclusion of some off-nadir observations.

MASCS is a point spectrometer with varying field-of-views (FOVs) due to MESSENGER's elliptical orbit and pointing constraints, thereby resulting in spatially varying data coverage. This resulted in systematically varying size of the MASCS footprints with integration time, altitude, and slant angle to the surface, which ranges from 0.1 km x 3 km (cross-track x down-track) to over 6 km x 7 km (Izenberg *et al.*, 2014). Therefore, in order to provide the best compromise between coverage, data quality, and computational power needed for the creation of a hyperspectral cube, in this study, the MASCS data were spatially binned ($1^\circ/\text{pixel}$) on an equant surface grid in a simple cylindrical projection following a similar approach by (Trang *et al.*, 2017). All spectra in the datacube were resampled to the same 2 nm wavelength resolution ranging from 300 nm to 1050 nm. The median reflectance spectrum of all the data points with their FOV completely within each pixel is calculated for all pixels in the grid. The

number of spectral data points for each pixel in the global MASCS cube is shown in Fig. 2.10 of the supplementary materials. This results in the global MASCS datacube of uniform equal-angular resolution at 1 pixel/degree resolution (~ 42.58 km/pixel spatial resolution at the equator).

Due to the varying spatial footprint (both spatial resolution and number of pixels per degree) of MASCS datasets for northern and southern hemisphere, the uniform equal-angular resolution (1 pixel/degree) therefore helps us to systematically characterize the spectral variations across the Mercury surface irrespective of the size of the surface features and the availability/density of the MASCS datasets across the Mercury surface. Therefore, this uniform equal-angular resolution (1 pixel/degree) dataset aid us efficiently to map the qualitative representation of the spectral heterogeneity across Mercury surface including its various geochemical regions.

As a secondary product, we derived a standard deviation hyperspectral datacube for all spectra within a given pixel to use as a measure of data quality, since such a metric can serve as a proxy to monitor sub-pixel variations. The variability map at 700 nm is shown in Fig. 2.11 of the supplementary materials. These variations are a combination of true variability in spectral properties of the surface within a spatial bin and the measurement uncertainties of the instrument. Fig. 2.11 shows that only the regions approaching the limiting $\pm 80^\circ$ latitudes show high variability, due to the highly variable observational geometry in these zones (see, for example, the area at 80°N , 135°W , in Fig. 2.11).

We further assessed whether the spectral maps were insensitive to variations in temperature of the VIS detector at the time of measurement. Fig. 2.12 shows the distribution of the VIS detector temperature for all observations used in this study. This distribution does not reproduce any of the features seen in the global maps discussed below or in subsequent spectral classification products, confirming they are not instrumental artifacts.

The hyperspectral datacube obtained by this procedure was visually inspected to check for anomalies, such as those originating from regions with low coverage or from pixels with high sub-pixel variations, and none were found.

2.4 STANDARD SPECTRAL PARAMETER MAPS

2.4.1 UV DOWNTURN

In order to spectrally identify pyroclastic deposits, (Goudge *et al.*, 2014) introduced a spectral parameter called the UV downturn. The UV downturn calculates the UV depth of the ratioed reflectance spectra where $UV_{depth} = Depth_{300} + Depth_{325} + Depth_{350}$, as defined in (Goudge *et al.*, 2014). In this study we calculated the UV downturn parameter for each pixel of the MASCS global spectral cube (Fig. 2.2a). As the spatial resolution of the MASCS global spectral cube is very coarse (1 ppd = 42.58 km/pixel at the equator), the UV downturn parameter for the localized, sub-pixel resolution pyroclastic deposits has been overshadowed by the signature of the more abundant surrounding materials. The resulting global UV-downturn map shows no major UV-spectral units.

2.4.2 VISIBLE SLOPE AND NORMALIZED VISIBLE SLOPE

The VIS_{slope} parameter defined as $VIS_{slope} = (R_{550} - R_{750}) / (550 - 750)$ (Goudge *et al.*, 2014, Besse *et al.*, 2015) is also used to identify the presence of the pyroclastic deposits as these deposits exhibit redder spectral slope compared to its surrounding materials. Previous studies further show that the steepness of this spectral slope strongly decreases with the distance from the pyroclastic vents (Besse *et al.*, 2015, Besse *et al.*, 2020). In this study, VIS_{slope} was computed for each pixel to characterize the global spectral slope properties of Mercury's surface (Fig. 2.2b). The normalized visible slope map (Fig. 2.2c) was computed by ratioing the VIS_{slope} values to the average Mercury spectrum derived from the global MASCS data set (Besse *et al.*, 2015). Both of these parameters display very similar variations. However, compared to VIS_{slope} map (Fig. 2.2b), the normalized VIS slope map strongly highlights some notable spatial units, including the northern smooth plains (NP-LMg), Nathair Facula (27.5°N 57.4°E), peak-ring basin Eminescu (10.7°N 114.21°E), bright rayed crater Fonteyn (32.8°N 95.5°E), and bright spots within the Caloris basin (30.2°N 162.8°E) (Fig. 2.2c). Nathair Facula is a prominent volcanic vent located north of Rachmaninoff basin and shows the highest visible slope in the global VIS_{slope} map and also corresponds with the geochemical terrane PD defined by (Vander Kaaden *et al.*, 2017).

Therefore, it is likely that global visible slope and normalized visible slope maps of Mercury highlight three geochemical terranes, the northern plains (NP), Caloris basin (CB), and pyroclastic deposits (PD). However, these standard spectral parameters are still not efficient to spectrally distinguish, NP-LMg from NP-HMg terranes.

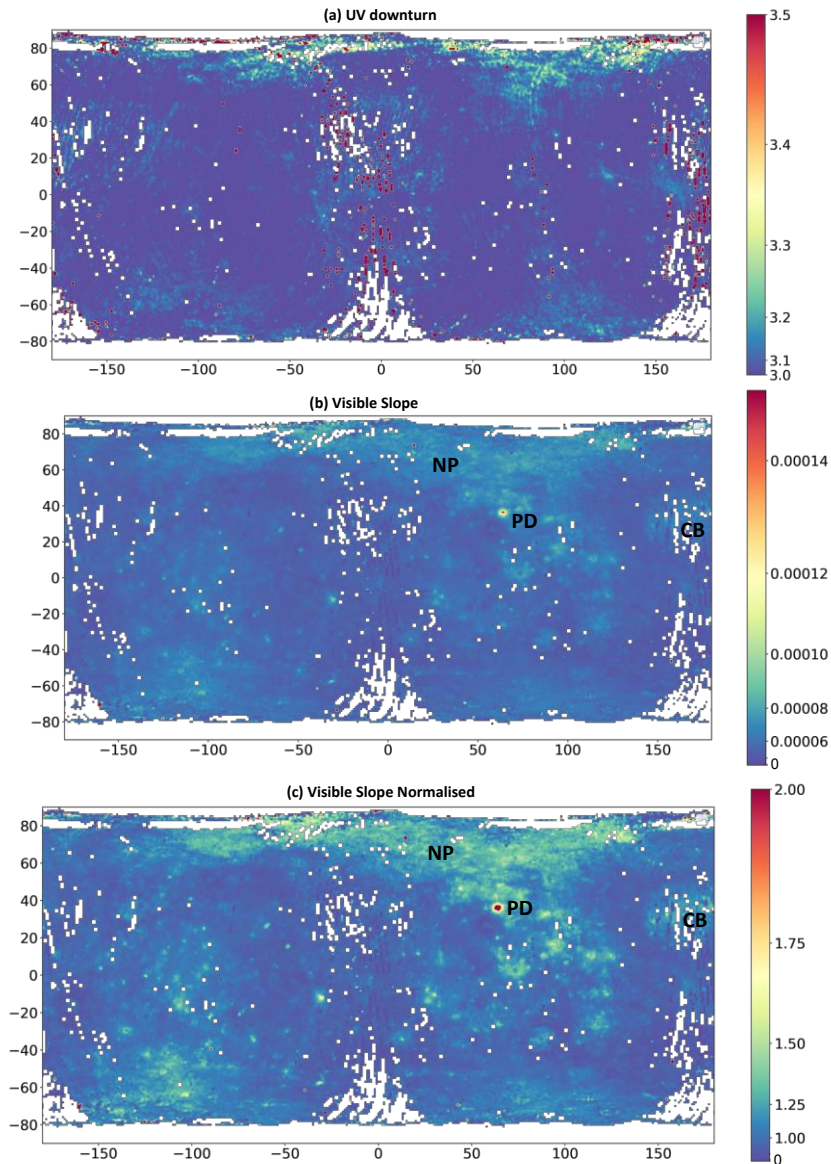


Figure 2.2. Standard spectral parameter maps derived from MASCs hyperspectral datacube. a) UV downturn map is derived using the UV_{depth} from (Goudge *et al.*, 2014) and shows at this spatial resolution no major surface units, b) Visible Slope Map is derived using the formula $VIS_{slope} = (R_{550} - R_{750}) / (550 - 750)$ and c) Normalized visible slope map is the ratio of VIS_{slope} to average Mercury spectrum (Goudge *et al.*, 2014, Besse *et al.*, 2015). Both b) and c) strongly highlight the very bright pyroclastic deposits (PD) located north of Rachmanioff basin as red units and also reveals the high reflectance northern plains (NP) and Caloris Basin (CB) as yellow units.

2.5 STATISTICAL ANALYSIS TECHNIQUES

The MASCS hyperspectral cube used in the multivariate analysis consists of a total of 58,493 pixels spreading across the surface at 1 degree/pixel spatial resolution with each pixel consisting of 296 spectral bands in the spectral range of 300 nm to 1050 nm at 2 nm spectral resolution. In order to find the global surface spectral variations embedded in the MASCS hyperspectral cube, we applied two multivariate analysis techniques; a) unsupervised clustering analysis (Section 2.5.1) and b) principal component analysis (PCA) (Section 2.5.2).

2.5.1 UNSUPERVISED CLUSTERING ANALYSIS

In this study, k-means clustering (MacQueen, 1967), the most widely used unsupervised multivariate partitional clustering algorithm, is used to characterize the global MASCS spectral datacube and identify possible spectral units. K-means is a centroid-based clustering technique, where each spectrum (vector) of the datacube is assigned to a specific cluster or central vector. The assignment to a cluster/vector is based by its proximity to the respective cluster/central vector. The parameter k refers to the desired number of clusters. The k-means clustering analysis uses an iterative approach to generate the clusters where the number of iterations is assigned manually.

For a given number of clusters, k, the K-means algorithm randomly chooses k central vectors in B, where B is the number of spectral bands in a MxNx B datacube. The algorithm then iteratively performs the following three steps for the given number of iterations; a) Computes the Euclidean distance between each spectrum in the datacube and the central vector for all k clusters (Bora *et al.*, 2014); b) Each pixel in the image is then assigned to the nearest central vector (cluster); c) Computes new central vectors by calculating the mean vector of all the spectra representing each cluster. The three steps are then repeated for the specified number of iterations. The k central vectors update their definition for each iteration, until they converge to a fixed set of values.

In this study, the initial MxNx B array of MASCS spectral data is 360x180x296 (longitude x latitude x spectral channels), the k-means algorithm then partitions the datacube into a kx B array of cluster centers such that the resulting intra-cluster spectral similarity is high but the inter-cluster similarity is low. The resulting image is an MxN (360x180=64800) array or a 1x1 degree orthogonal map where the values (1,2,..) are the index of the assigned cluster for each

pixel. In this study, the value of k is varied from 2 to 10 in steps of 1, and the k -means clustering was performed for each k value (Fig. 2.13).

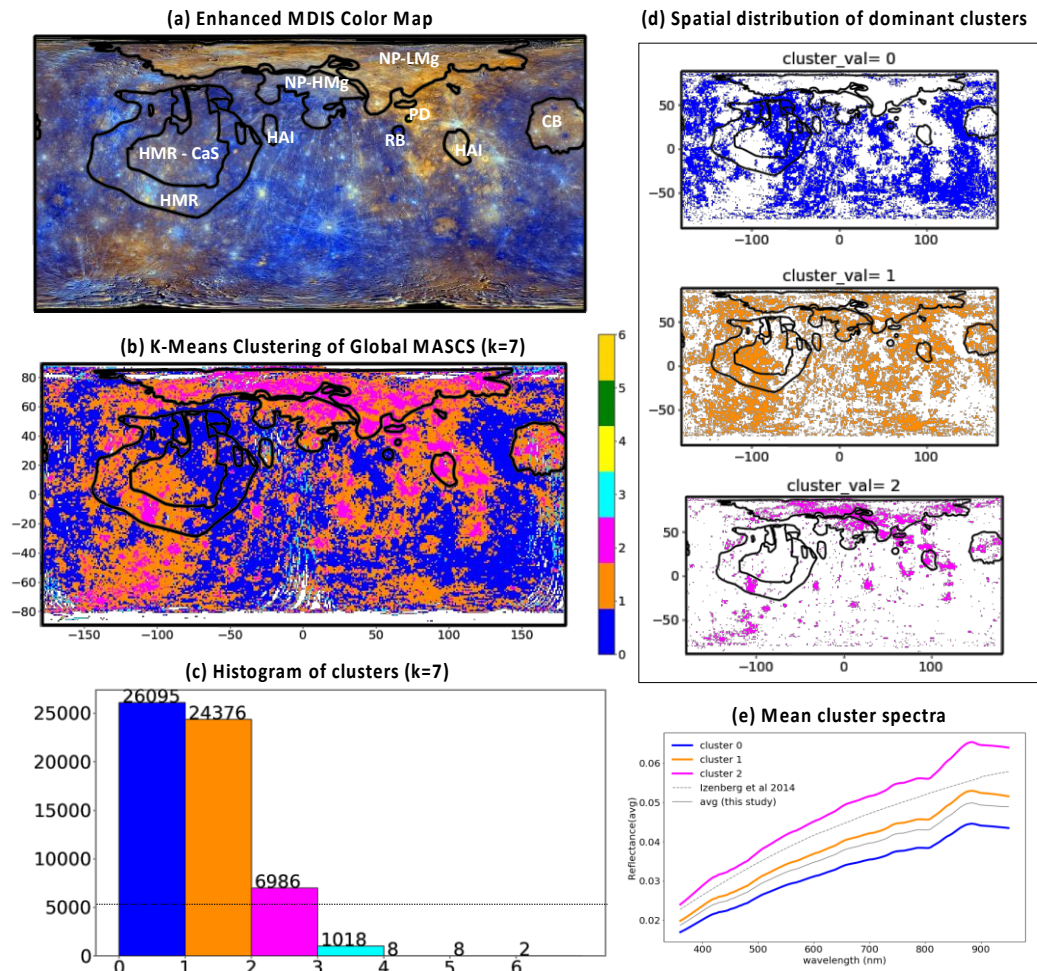


Figure 2.3. a) MDIS enhanced global color mosaic by Domingue et al. (2015), b) K-means clustering of global MASCS datacube for $k=7$ of Mercury, c) histogram showing the number of pixels per cluster, d) shows the spatial distribution of the three contiguous classes (0,1,2) against their respective color units (blue, orange, magenta) respectively, e) shows the mean spectra representing the clusters 0 (blue), 1 (orange), and 2 (magenta) units along with the the new global MASCS average spectra derived in this study (solid-gray) against the global MASCS average spectra in previous study (dashed-gray). The differences in the average Mercury spectra (Izenberg et al. (2014) vs this study) is due to the error in the earlier MASCS calibration pipeline which was reported and corrected for the new updated MASCS data products released by PDS.

For each resulting k -means cluster map, the number of pixels per cluster is plotted in Fig. 2.13. Fig. 2.13 shows that when increasing k from 2 to 6, the most of Mercury's surface falls only into two contiguous regions (Fig. 2.13; $k=2-6$). However, when increasing k from 7 to

10 (Fig. 2.13; $k=7-10$), clusters 0, 1, and 2 (where number of pixels per cluster > 10% of total number of pixels) for corresponding $k(=7-10)$, shows that the Mercury surface falls into three contiguous regions.

In this sub-section, Figures 3a and 3b compare the MDIS enhanced global color mosaic (Domingue *et al.*, 2015) and the MASCS k-means ($k=7$) cluster map, respectively. Fig. 2.3c shows the number of pixels per cluster (for $k=7$). Fig. 2.3d shows the spatial distribution of three contiguous clusters 0, 1, and 2 over Mercury surface. The mean spectra of the three MASCS clusters; clusters 0 (Fig. 2.3e; blue), 1 (Fig. 2.3e; orange), and 2 (Fig. 2.3e; magenta) units are computed and plotted against the global MASCS average spectrum derived from this study (Fig. 2.3e; solid-gray) and (Izenberg *et al.*, 2014) (Fig. 2.3e; dashed-gray).

Fig. 2.3 shows a strong correlation between the global MDIS data (Fig. 2.3a) and the clustered MASCS datacube (Fig. 2.3b) and their relation to the major geochemical terranes (Fig. 2.3d). The blue units (cluster=0; Fig. 2.3d) mainly comprise of the underlying material within intercrater terrane (IT) including low reflectance material (LRM). This suggests that the blue units mainly correspond to the older terranes exposed to greater degree of space weathering possessing the darkest spectral reflectance surface units (Fig. 2.3e; cluster 0; blue). The magenta units (cluster=2; Fig. 2.3d) includes the major part of the NP, the bright materials inside CB, and the bright rayed fresh craters and volcanic materials within the IT. This suggests that the magenta units (cluster 2; Fig. 2.3d) mainly corresponds to the fresh material exposed on the surface with less degree of space weathering possessing the brightest spectral reflectance surface units (Fig. 2.4e; cluster 2; magenta). The orange units (cluster=1; Fig. 2.3d) consists of the surrounding surface of magenta units of the northern plains (NP), and the floor of Caloris basin (CB). These units belong to the intermediate spectral reflectance surface units (Fig. 2.3e; cluster 1; orange).

Fig. 2.3e shows that the overall spectral shape of the three k-means spectral units (cluster 0,1, 2; blue, orange, magenta) are similar and nearly featureless. The average overall reflectance values of the clusters can be sorted as cluster 2 (magenta) > cluster 1 (orange) > cluster 0 (blue) and the slope of the spectra against the wavelength between the classes can be sorted as cluster 2 (magenta) > cluster 1 (orange) > cluster 0 (blue). Though k-means classification helps in understanding the spectral nature of the three major classes of Mercury

surface, this technique yet could not differentiate between the low-Mg (NP-LMg) and high-Mg regions (NP-HMg) of northern plains (NP).

Due to an error discovered in the photometric normalization section of the MASCS calibration pipeline (<https://pds-geosciences.wustl.edu/missions/messenger/index.htm>), the reflectance values of the global Mercury average spectra published in previous study (Izenberg *et al.*, 2014) were off by a factor of 2 (Fig. 2.3e; dashed-gray). Since this study uses the updated MASCS data products by PDS release which corrected for this offset, the reported global average reflectance (Fig. 2.3e; solid gray) shows that Mercury surface materials are darker (Fig. 2.2d) than reported earlier (Fig. 2.3e; dashed-gray) as in (Izenberg *et al.*, 2014).

2.5.2 PRINCIPAL COMPONENT ANALYSIS

In most cases, hyperspectral data (e.g., MASCS) represent more information by preserving the spectral band shape of the minerals; whereas, multispectral data (e.g., MDIS) only contain spectral information from a non-continuous limited number of bands. However, the mean MASCS spectra from the three major clusters resulting from the k-means analysis (Fig. 2.3e) show that the typical Mercury spectrum is nearly featureless and red-sloped. In this study, we used principal component analysis (PCA), a common multivariate statistical technique, to effectively disentangle the variance among these highly correlated reflectance values for each spectrum in the MASCS datacube (Jolliffe, 2011, Goodfellow *et al.*, 2016). In other words, PCA projects the input vectors (or spectra) composing the datacube into a new orthogonal coordinate system defined by the eigenvectors of the covariance matrix of the original dataset. The first principal component retains the largest variance in the data and the succeeding components represents the highest remaining data variance under the condition that it is orthogonal to the preceding components. Each datapoint of the eigenvector is thus represented by the coefficients relative to each principal component.

In this study, we reduced the 296-channel MASCS datacube to a 9-channel datacube of principal component coefficients. These first 9 coefficients retain 99% of the original variance and are shown in Fig. 2.4. Fig. 2.4 (a-i) shows the global principal components PC1, PC2, PC3, PC4, PC5, PC6, PC7, PC8, and PC9 along with their eigen-vectors and are explained below. All the PC maps in Fig. 2.4 are presented on a uniform scale with values ranging from -5 to 5 and the representative colormap uses a power law scale ($y=x^\gamma$, where $\gamma=5$).

a) The PC1 map (Fig. 2.4a), which represents the highest variance for each MASCS spectra, is similar to the two major clusters obtained from k-means clustering (Fig. 2.2b) of the MASCS datacube (explained in detail in [Section 2.6.1](#)).

b) The PC2 map (Fig. 2.4b), which represents the second highest variance and is orthogonal to PC1 map (Fig. 2.4a), interestingly displays similar clusters as the k-means clustering (Fig. 2.2b), but the inverse of what is seen in the PC1 map. The spectral significance of PC2 map is explained in detail in [Section 2.6.2](#).

c) The PC3 (Fig. 2.4c), PC4 (Fig. 2.4d), and PC5 (Fig. 2.4e) maps show no significant correlation with surface units, displaying little spatial variance among these principal components. These PCs (Fig. 2.4 c-e) are dominated by variation between 800 and 950 nm which are likely instrumental artifacts (channel to channel offsets not removed by instrument calibration) and not geological information.

d) PC6 (Fig. 2.4f) shows localized spectral units that represent specific surface characteristics and its discussed in detail in [Section 2.6.3](#).

e) PC7 (Fig. 2.4g), PC8 (Fig. 2.4h), and PC9 (Fig. 2.4i) also show no significant correlation with surface regions and may correspond to the noise in the data from spectra of the high northern and southern latitudes.

2.6 REGIONAL AND GLOBAL PERSPECTIVE OF MASCS PRIMARY PCs

As discussed in [Section 2.5.2](#), MASCS PCA analysis reveals three primary principal component coefficients, PC1, PC2, and PC6 (Fig. 2.4), that correlate with geomorphologically and geochemically distinct terranes on Mercury. The significance of these primary PCs is discussed below.

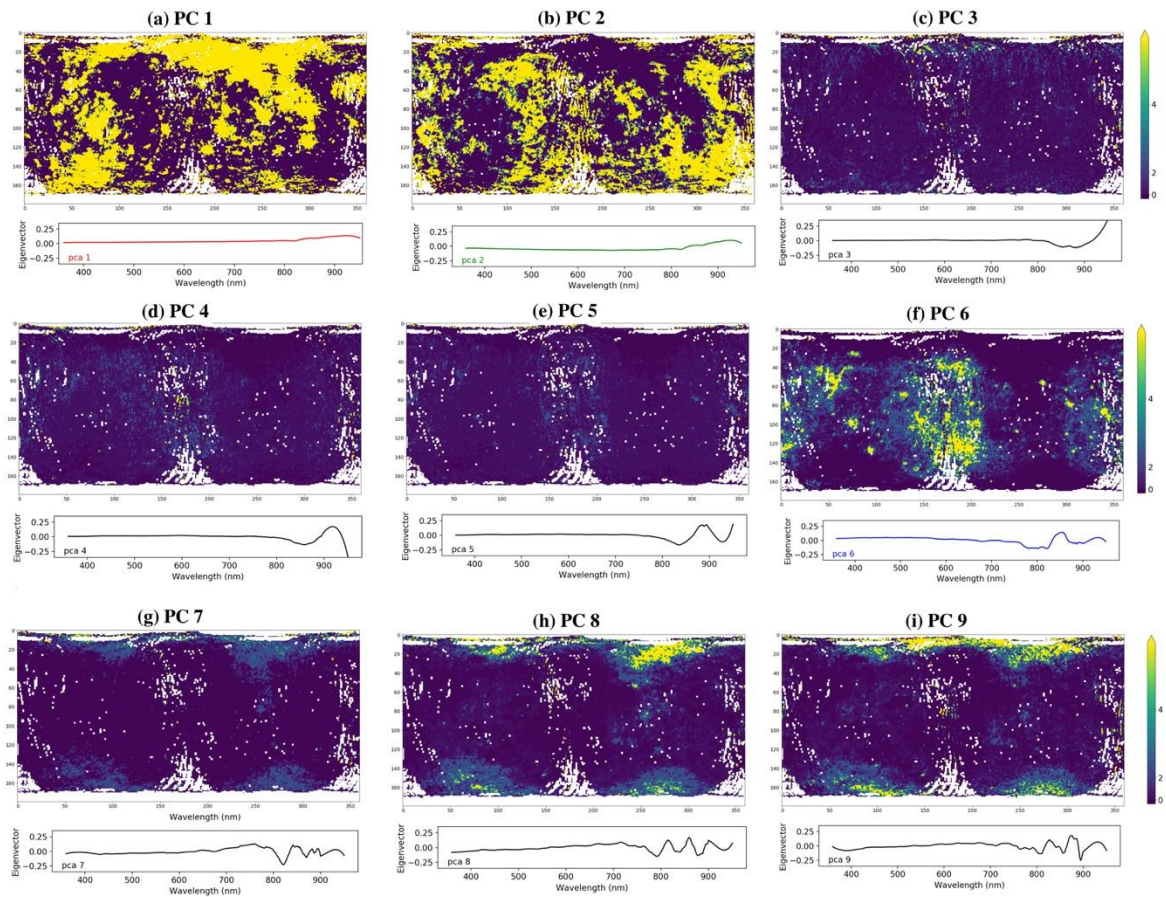


Figure 2.4. (a-i) Top box of each panel shows the PCA coefficients maps for components PC1 to PC9 respectively represented by a uniform scale with values ranging from -5 to 5 and the representative colormap uses a power law scale ($y=x^\gamma$, where $\gamma=5$). Bottom box: shows the corresponding eigen vector of each principal component. PC1 and PC2 are orthogonal to each other and further representing two contiguous spectral clusters as K-Means map (Fig. 2.2b). PC6 shows localized spectral units that represent specific surface characteristics (see Fig. 2.7) and discussed in detail Section 2.6. The rest of the PCs show no significant correlation with surface units, displaying little spatial variance among these principal components.

2.6.1 PRINCIPAL COMPONENT (#1)

The MASCS PC1 map (Fig. 2.5) is closely associated with the global reflectance map at 750 nm. For example, the PC1 values corresponding to yellow pixels in Fig. 2.5a (PC1) closely resembles the global reflectance (at 750 nm) map (Fig. 2.5b), suggesting brighter surface materials with albedo $\sim >0.05$ at 750 nm are distinguished by PC1. The PC1 map also strongly resembles the global k-means cluster map of Mercury (Fig. 2.2b; Section 2.5.1). Notable geochemical terranes associated with this component includes the northern volcanic plains (NP), Caloris basin's (CB) interior, and pyroclastic deposits (PD). This suggests that PC1 may be correlated with younger Mercury terranes which include volcanic plains, fresh impact crater units, bright pyroclastic deposits, and fresh bright hollows.

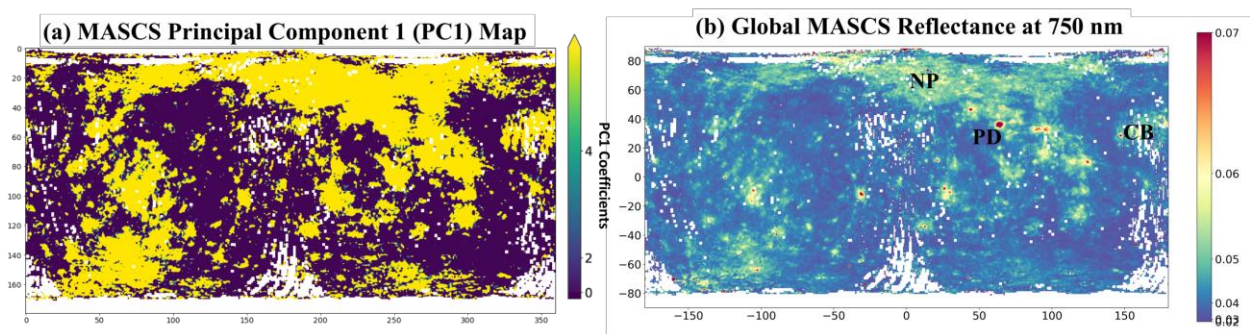


Figure 2.5. a) PC1 map represents the highest variance for each MASCS spectra and is similar to the two major clusters obtained from k-means clustering (Fig. 2.2b) b) Global MASCS reflectance at 750 nm highlighting three major geochemical terranes which includes northern plains (NP), caloris basin (CB), and pyroclastic deposits of Nathair Facula (PD). Comparison of a) and b) shows that the yellow units in PC1 map represents the surface with reflectance value $\sim >0.05$ at 750 nm.

2.6.2 PRINCIPAL COMPONENT (#2)

In contrast to PC1, PC2 correlates with darker underlying materials, representing the oldest terranes (>4 Ga) on Mercury (Fig. 2.7a). Comparisons of the PC2 map with the derived space weathering map (Fig. 2.7b) (Trang *et al.*, 2017), show correlations with weathered units with abundances of nanophase iron $>1.167\%$, as derived by (Trang *et al.*, 2017) from the MASCS VIRS data. This suggests that, PC2 seems to be correlated with older Mercury terranes which include intermediate terranes (IT), low reflectance materials (LRM) units, and Caloris exterior smooth plains.

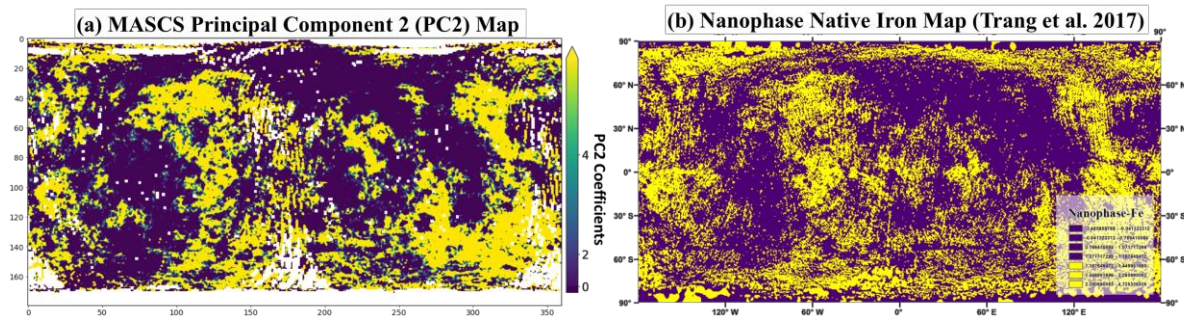


Figure 2.6. a) PC2 map represents the second highest variance for each MASCs spectra and is orthogonal to PC1 map as shown in Fig. 2.5a and b) nanophase iron map from (Trang *et al.*, 2017). The comparison between a) and b) shows that yellow units represented by PC2 map closely relates to the surface materials with higher degree of space weathering.

2.6.3 PRINCIPAL COMPONENT (#6)

The PC6 map is in Fig. 2.7 overlaid on the MDIS color basemap to better understand the spectral surface characteristic represented by this particular principal component. Comparisons of the PC1 map (Fig. 2.4a) and the PC6 map (Fig. 2.7a) show that the PC6 represents units that are a subset of those represented by PC1. A few of the surface features represented by PC6 are discussed below (Fig. 2.7b-k). Using the MDIS color basemap, the bright and dark surface features highlighted by yellow regions of PC6 map are marked in white and black arrows respectively in the figures 6b-k (left). Within the PC6 map (Fig. 2.7a-k), the blue regions generally surround the yellow regions and the violet units have the lowest PC6 values.

Northern Volcanic Plains (NP, Fig. 2.7b): The NP are the largest smooth plains unit on Mercury, hosting two geochemical regions; a) a low-Mg terrane (NP-LMg) that covers most of Borealis planitia, and b) a high-Mg terrane (NP-HMg) that extends over a smaller portion of the NP to the south of the crater Hokusai (D=114 km, 57.86°N 16.63°E) (Vander Kaaden *et al.*, 2017). Within the NP, PC6 highlights surface materials within the NP-HMg regions, which include both brighter (white arrows) and darker (black arrows) materials seen in the MDIS color map. Morphologically, there are no clear borders that distinguish the PC6 units from rest of the NP. The brighter PC6 units include the rim and floor of Hokusai crater and a portion of its ejecta rays, two fresh bright-rayed unnamed craters (labeled unnamed crater 1 & unnamed crater 2 in Fig. 2.7b left). Some of the darker materials highlighted by PC6 include darker plains in the north of unnamed crater 1 and the northern crater wall and floor of unnamed crater 3 (Fig. 2.7b left), possibly contaminated with brighter ejecta materials from nearby fresh craters.

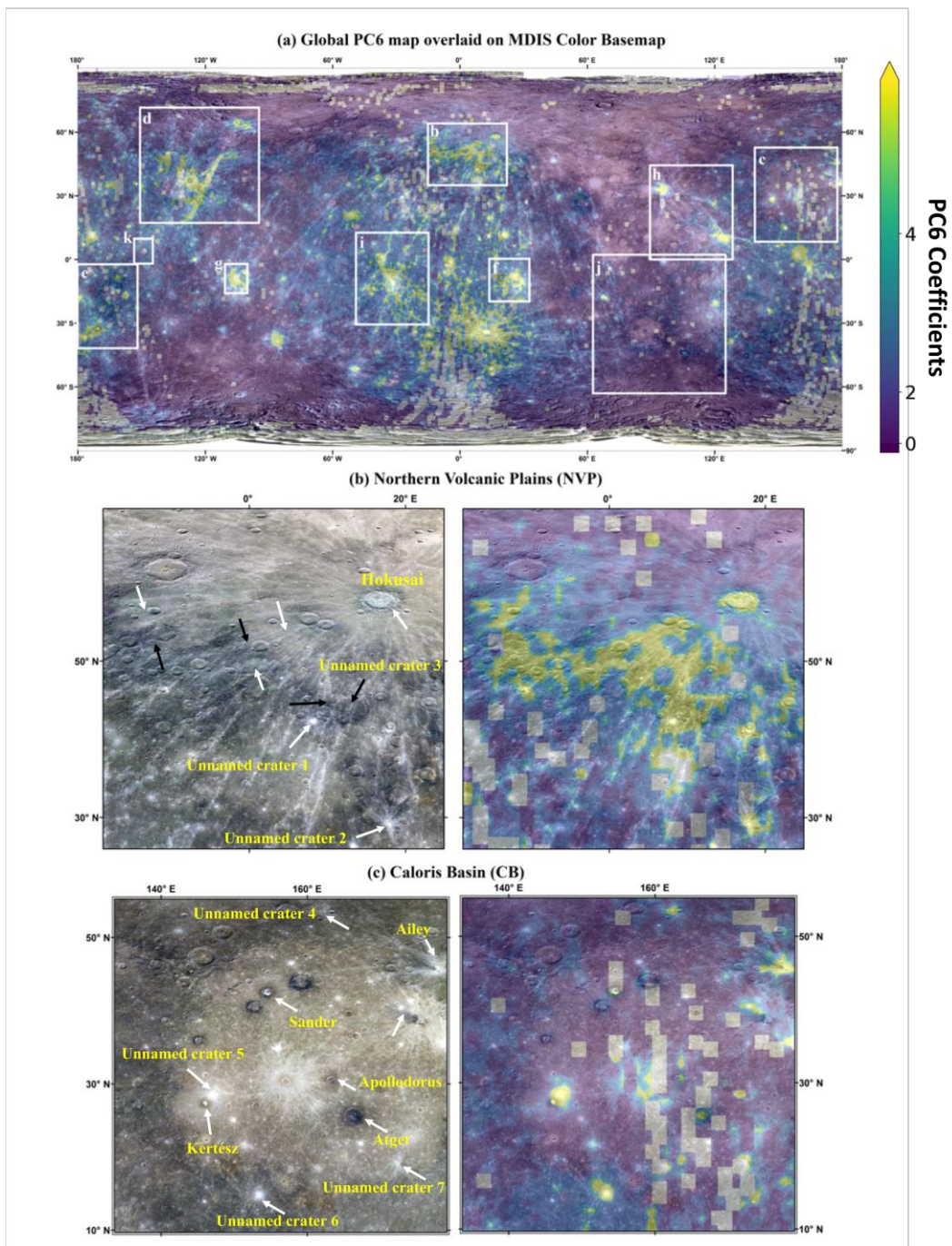


Figure 2.7. a) PC6 map is overlaid on the MDIS 8-color basemap and the white boxes corresponds to study regions shown in b) northern volcanic plains, c) Caloris basin, The white and black arrows in each MDIS color map in b-c corresponds to the bright and dark surface units respectively those belong to yellow regions in PC6 map (b-c; right).

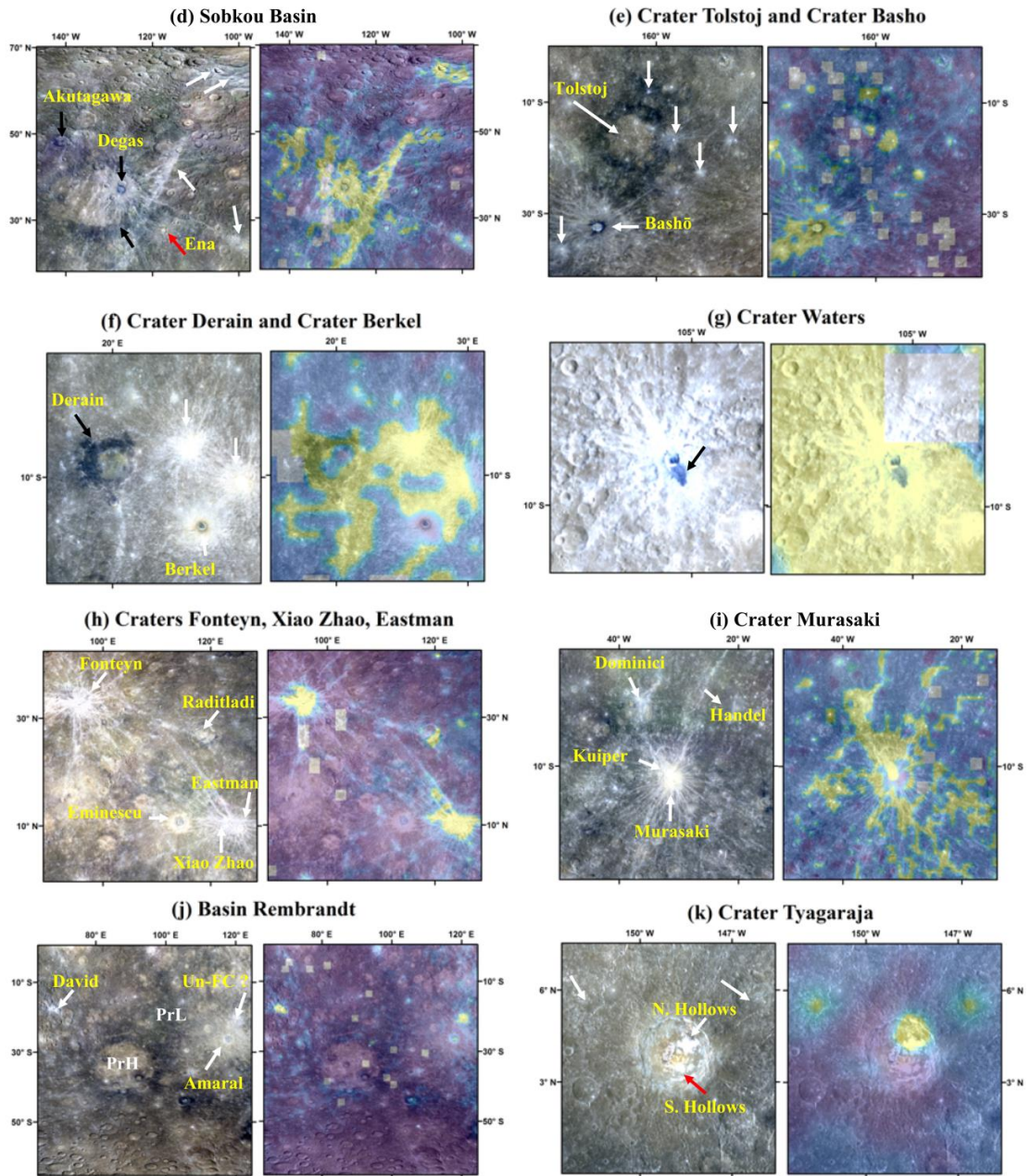


Figure 2.7. (contd) d) Sobkou basin, e) craters Tolstoj and Basho, f) craters Derain and Berkel, g) crater Waters, h) craters Fonteyn, Xiao Zhao, and Eastman, i) crater Murasaki, j) basin Rembrandt, and k) crater Tyagaraja. Left images in b-k corresponds to MDIS color basemap of each study region and those on the right to its corresponding PC6 map. The white and black arrows in each MDIS color map in b-k corresponds to the bright and dark surface units respectively those belong to yellow regions in PC6 map (b-k; right).

Caloris Basin (CB, Fig. 2.7c): Caloris is the youngest and largest impact basin ($D \sim 1550$ km, 31.84°N 162.45°E) on Mercury, preserving the post-volcanically and -tectonically modified landforms within its interior HRP (Murchie *et al.*, 2008). Associated with Caloris is the presence of a radial magnetic anomaly (Hood, 2016). Caloris planitia also hosts craters, such as Sander ($D = 47$ km, centered at 42.44°N 154.60°E) and Kertész ($D = 32$ km, centered at 27.40°N 146.10°E), which contain hollows units within their LRM floors. The hollows units have been shown to host volatile-rich materials (Blewett *et al.*, 2013, Helbert *et al.*, 2013a, Vilas *et al.*, 2016). Along the entire CB floor, the PC6 units correlate only with brighter surface features, such as bright rayed fresh/immature craters (for example crater Ailey ($D = 23$ km, centered at 45.58°N 177.93°E)), the hollow materials within craters Kertész and Sander, and the bright central peaks of craters Atget ($D = 100$ km, centered at 25.58°N 166.37°E) and Apollodorus ($D = 41.5$ km, centered at 30.55°N 163.39°E). The Caloris basin interior smooth plains (HRP) and the LRM units within such craters as Munch ($D = 57$ km, centered at 40.46°N 152.75°E) and Poe ($D = 77$ km, centered at 43.76°N 159.09°E) are not correlated with PC6. Examination of the PC6 map within Caloris basin (Fig. 2.7c) suggests that irrespective of the differences in the compositions among the varying morphologies (hollows, fresh craters, central peaks) correlated to this principle component, the PC6 units may only highlight materials (yellow units) which are relatively fresh or immature.

Sobkou Basin (Fig. 2.7d): The ~ 4.0 Gy old Sobkou Basin ($D=770$ km; 35°N 225°E) lies in Sobkou Planitia which is associated with two magnetic anomalies (Hood, 2016). It possesses a stronger magnetic anomaly that is correlated with surrounding dark LRM ejecta materials, and a weaker magnetic anomaly within the basin floor HRP materials that are volcanic in origin (Hood, 2016). Within Sobkou planitia lies the Degas crater ($D=45$ km). Degas is one of the freshest bright-rayed craters on Mercury's surface. It is surrounded by LRM along its rim and contains bright hollows within its crater floor (Blewett *et al.*, 2013, Thomas *et al.*, 2014a, Bott *et al.*, 2019). PC6 (Fig. 2.7d) correlates with the brighter materials within Degas crater and with the crater's ejecta, including the darker rim. PC6 (Fig. 2.7d) also correlates with regions of darker albedo materials, such as the rim of Akutagawa ($D=106$ km 48.25°N 141.03°W) crater, in addition to other brighter albedo regions such as the bright ejecta streak on the eastern rim of the older basin in Sobkou planitia. Like CB, PC6 units within Sobkou planitia highlight compositionally different surface units.

Tolstoj Basin and Basho Crater (Fig. 2.7e): Tolstoj (D=355 km, 16.2°S 165°W) is a ~3.9-4.0 Gy old basin characterized by LRM-rich ejecta and a basin floor filled with HRP volcanic plains, and is thus one of the highest color contrasting features on Mercury's surface (Robinson *et al.*, 2008). In contrast, Basho crater (D=64 km, 32.4°S 170.5°W), located southwest of Tolstoj, has bright-rayed ejecta and a dark, LRM-containing rim, thus exposing compositionally heterogeneous upper crustal materials (Robinson *et al.*, 2008). In the PC6 map (Fig. 2.7e), the Tolstoj region, including both the LRM and HRP materials, show no correlation with even the lowest PC6 values. On the other hand, the LRM rim, bright crater floor, and bright ejecta materials from the younger crater Basho, are strongly correlated to PC6. The white arrows in Fig. 2.7e indicate additional small fresh/immature craters which both expose brighter materials and are strongly correlated with PC6.

Derain and Berkel Craters (Fig. 2.7f): Derain crater (D=175 km; 9°S, 19.7°E) is a pit-floored "unfilled" crater formed between the Mansurian (~3-3.5 Ga) and Tolstojan (~3.9-4.0 Ga) eras (Hargitai *et al.*, Herrick *et al.*, 2018). It is well known for the presence of an asymmetric annular distribution of LRM along its rim (Denevi *et al.*, 2009, Xiao *et al.*, 2013, Mancinelli *et al.*, 2015) and shallow pits with irregular and scalloped walls which conform to its central peak. Intriguingly, the PC6 component within this crater correlates only with the LRM material covering the crater rim. Also noted in the PC6 map of this region is a correlation of this component with another asymmetric dark-rayed fresh crater (D = 21.28 km; 11.9°S, 20.1°E) south of Derain (marked by a black arrow in Fig. 2.7f).

Like the LRM discussed above, the fresh material excavated by two bright-rayed craters, un-fc1 (D= <166m, 8.19°S, 25.75°E) and un-fc2 (D=27.7km, 10.32°S, 29.83°E) (marked by white arrows in Fig. 2.7f) are also correlated with PC6 (Fig. 2.7f). However, the dark crater floor and the bright ejecta of Berkel crater (D=23 km, 13.7°S 26.8°E) within this same region shows no correlations in the PC6 map. Independent of the heterogeneity in the composition, depth, freshness of the excavated material, and the close proximity of these craters, the higher PC6 values (yellow pixels) indicate a similar physical structure for these diverse surface materials, possibly an indicator of a fine-grained component to the surface regolith in these regions.

Waters Crater (Fig. 2.7g): Waters crater is a geologically young, 15 km diameter, bright-rayed, fresh crater (centered at 8.96°S 105.45°W) that possess a 20 km long, dark

impact-melt flow feature (Blewett *et al.*, 2014, D’Incecco *et al.*, 2015), which is indicated by the black arrow in Fig. 2.7g. Within this spatial scale both Waters crater and the melt-flow are contained in the same spatial pixel; however, this is the very important target for the high spatial resolution data. The phase-ratio analysis of Waters crater suggests that this particular low reflectance melt-flow has a different photometric character than the surrounding terranes (Blewett *et al.*, 2014). The melt-flow displays an increase in reflectance with decreasing phase angle; suggesting that the melt-flow is comprised of coarse-grained regolith compared to the finer-grained regolith in the surrounding units. (D’Incecco *et al.*, 2015) suggests that the color differences between the crater and its melt-flow could also be explained by compositional heterogeneities, shock metamorphism, and/or space weathering effects. However, the PC6 map displays no differences between the crater, its ejecta, and the melt-flow. This may be due to the low spatial resolution of global MASCS data (42.58 km/pixel).

Raditladi Region (Fig. 2.7h): The region covered in Fig. 2.7h is known for the presence of hollows within the peak-ring and floor of Raditladi basin (D=258 km, 27.17°N 119.12°E) and within the central peak and peak-rings of Eminescu crater (D=129 km, 10.66°N 114.19°E) (Blewett *et al.*, 2011). The PC6 map displays correlations only with the fresh hollow materials exposed in the south-eastern peak ring of Raditladi basin. The hollows within the peak-rings of Eminescu are not seen in the PC6 map, which could be due to the coarse spatial resolution of the MASCS spectral datacube. The two bright rayed fresh craters Fonteyn (D=29 km, 32.82°N 95.52°E) and Xiao Zhao (D=24 km, 10.59°N 123.79°E), along with their ejecta rays, are distinguishable in the PC6 map. This suggests that irrespective of compositional differences, for example hollows or crustal material, it is the immature nature of the surface regolith that is highlighted in the PC6 map.

Kuiper and Murasaki Craters (Fig. 2.7i): Kuiper (D=62 km, 11°S, 31.5°W) is one of the brightest Mercurian features, possessing prominent bright ejecta-rays. It sits on the north-western topographic rim of the older and more degraded Murasaki crater (D=132 km, 12.5°S, 30.4°W) (Hapke *et al.*, 1975, De Hon *et al.*, 1981, Harmon *et al.*, 2007, D’Incecco *et al.*, 2015). Kuiper marks the beginning of the youngest chronostratigraphic period on Mercury (~1 Ga; Kuperian) (Spudis and Guest, 1988). Mariner 10 data suggests the excavation of material with a low-opaque content for both Kuiper and Murasaki (Robinson and Lucey, 1997, Blewett *et*

al., 2007, Blewett *et al.*, 2009). In the PC6 map (Fig. 2.7i), the ejecta rays of both young Kuiper and older Murasaki display a strong correlation to PC6. The PC6 map also shows a correlation between PC6 and Dominici crater (D=20 km, 1.38°N 323.5°E). A 629 nm absorption feature detected in the MDIS color data (Vilas *et al.*, 2016) suggest the presence of sulfides (CaS, MgS) in the fresh hollows on Dominici's southern rim/wall. Overall, in Fig. 2.7i, the PC6 map suggests correlations between PC6 and surfaces hosting immature and/or low-opaque materials.

Rembrandt Basin (Fig. 2.7j): Rembrandt is the second largest impact basin after Caloris and is one of the youngest impact basins, with a similar age to Caloris basin (~3.9 Ga) (Watters *et al.*, 2009). This ~715 km diameter basin (32.9°S 87.9°E) impact event led to the formation of two spectrally and morphologically distinct units; a) a rough textured impact melt deposit identified by low-reflectance exterior plains (PrL) and b) a smooth textured volcanic infilling identified by high-reflectance interior smooth plains, which formed in quick succession with the basin formation (Whitten and Head, 2015). Therefore, the PC6 map does not display any correlation with either of the spectrally distinct units within Rembrandt basin.

Also, within the region shown in Fig. 2.7j is the bright-rayed, ringed-peak cluster basin Amaral (D=105 km, 26.5°S 117.8°E), which is Kuiperian in age (~1 Ga) (Kinczyk *et al.*, 2016). There are varying correlations within this basin that are distinguishable in the PC6 map, with the ringed-peak clusters having the strongest correlation. Spatially resolvable are fresh bright-rayed craters such as David (D=23 km, 17.7°S 67.9°E) and an unnamed fresh crater (D=17.25 km, 20.4°S 120.6°E); both showing strong signatures in the PC6 map. This suggests that irrespective of the type of composition (volcanic or crustal), the PC6 component highlights the physical properties of the surface, especially those containing very fresh material identifying regions which have experienced the least amount of regolith processing.

Tyagaraja Crater (Fig. 2.7k): Tyagaraja crater (D=97 km, 3.9°N 148.9°W), formed in the Mansurian (~3.0-3.5 Ga) to Kuiperian (~1.0 Ga) period (Kinczyk *et al.*, 2016, Jozwiak *et al.*, 2018), is well known for having excavated subsurface LRM. This crater also contains extensive bright-halo hollows (N. hollows and S. hollows; Fig. 2.7k) on its crater floor alongside probable pyroclastic vents (Blewett *et al.*, 2011). In the PC6 map, the regions covering the north-eastern crater rim, wall, and the floor covering part of the N. Hollows are distinguishable. The remainder of the crater, including the pyroclastic vents and the S. Hollows are not

distinguishable in the PC6 map due to the coarser spatial resolution. The PC6 map also correlates with two areas on either side of the northern region of the crater; however, morphologically, these two areas are not correlated to any unique morphologically or geochemically distinct units.

2.7 GLOBAL MULTIVARIATE SPECTRAL ANALYSIS

In this study, we created a global MASCS false color composite (FCC) map using PC1, PC2, and PC6, where each component was assigned to a color channel (red, green, and blue, respectively, Fig. 2.8a) to understand the spectral heterogeneity of the Mercury surface and its relation to Mercury's geochemistry and mineralogy. The boundaries of the geochemical terranes found by (Vander Kaaden *et al.*, 2017) are overlaid on the FCC (Fig.7a, black) to examine any correlations between the geochemical terranes and the MASCS spectral units. The white boxes in Fig. 2.8a corresponds to the PC6 study regions discussed in Section 2.6.3. The MASCS' FCC map was then overlaid on the MDIS 3-color (R: 1000nm, G: 750nm, B: 430nm) global map (665 m/pixel spatial resolution) for a comparative analysis of the spectral and color terranes of Mercury, shown in Fig. 2.8. Table 2.1 summarizes the MASCS PC color units from Fig. 2.8a and its corresponding derived mineralogy from (Namur and Charlier, 2017) and (Vander Kaaden *et al.*, 2017) for each geochemical terrane which are further discussed in Section 2.7.1.

The global MASCS PC color composite shown in Fig. 2.8a can be visually characterized by five distinct color units:

a) red units correspond to spatial regions belonging to the highest values (yellow regions) in the PC1 map (Fig. 2.5a), and lowest values (violet regions) in the PC2 (Fig. 2.6a) and PC6 (Fig. 2.7a) maps (PC1>>PC2~PC6).

b) green units correspond to spatial regions belonging to the highest values (yellow regions) in the PC2 map (Fig. 2.6a), and lowest values (violet regions) in the PC1 (Fig. 2.5a) and PC6 (Fig. 2.7a) maps (PC2 >> PC1~PC6).

(a) MASCS Color Composite R:PC1 G:PC2 B:PC6

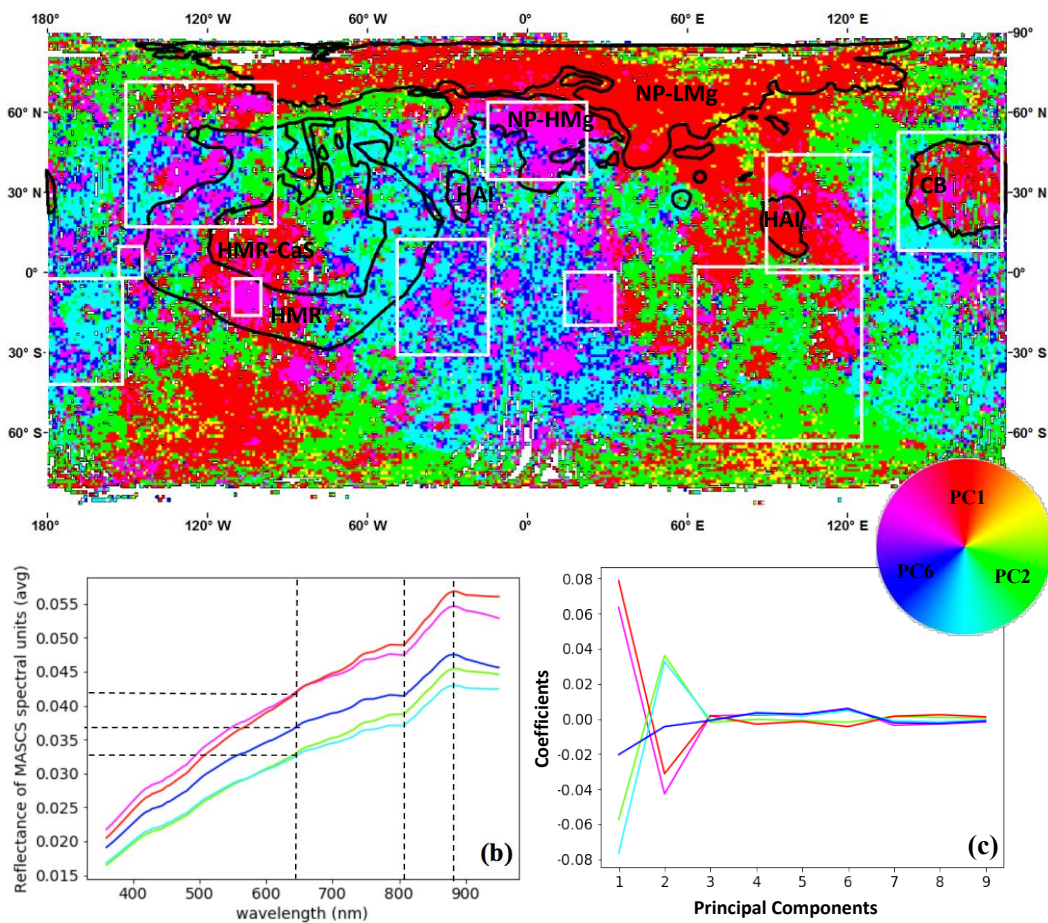


Figure 2.8. a) MASCS false color composite (FCC) map created by assigning red, green, and blue channels to PC1, PC2, and PC6 respectively. MASCS FCC shows that Mercury's surface can be broadly characterized into 5 color units; red, green, magenta, cyan, and blue. The white boxes correspond to the study regions mapped in PC6 map, shown in Fig. 2.7a, where the magenta units within the white boxes correspond to the yellow units in PC6 map in Fig. 2.7a. The black boundaries correspond to various geochemical terranes mapped by (Vander Kaaden *et al.*, 2017). The northern volcanic plains having high-Mg (NP-HMg) and low-Mg (NP-LMg) are characterized as two distinct spectral units, magenta and red respectively, in MASCS FCC. b) the average spectra of each color units in FCC. The vertical dotted line along 650 nm is used to classify these color units: high reflectance units (red, magenta), low reflectance units (green, cyan), and intermediate reflectance units (blue). The intermediate reflectance units generally envelope the magenta units. The average spectra of all color units display two minor absorption features near ~ 450 nm and ~ 800 nm along with a downward slope after ~ 890 nm. c) the plot between each principal component and the coefficients of each color unit.

c) magenta units correspond to common areas within the yellow regions in the PC1 map (Fig. 2.5a) and PC6 map (Fig. 2.7a) respectively (PC1~PC6 >> PC2). All the magenta regions within the white boxes in Fig. 2.8a correlates with the yellow regions in PC6 map in Fig. 2.7a.

d) cyan units correspond to common areas within the yellow regions in the PC2 map (Fig. 2.6a) and intermediate values (blue regions) in PC6 map (Fig. 2.7a) respectively (PC2~PC6 >> PC1).

e) blue units don't share any common properties of PC1 and PC2 and commonly surrounds magenta and cyan units (PC6 >> PC1~PC2).

From the context of Mercury's surface as characterized by the PC1, PC2, and PC6 components (discussed in [Section 2.6](#)), the five distinct color units in the MASCS' FCC map segregate Mercury's surface into; 1) red units; high reflectance spectral units (HRPs) mainly representing young volcanic smooth plains, including the northern smooth plains and the Caloris interior plains, 2) magenta units; representing some of the younger and immature surface regolith typically believed to contain low-opaque materials and have experienced the minimum amount of space weathering (such as hollows, fresh bright-ejecta craters, brighter peak rings, and some of the exposed LRM units), 3) green units; representing some of the oldest terranes such as dark, LRM-containing surface materials, 4) cyan units; generally representing darker LRM terranes contaminated by ejecta from surrounding young craters, and 5) blue units; commonly surrounding both magenta and cyan units.

For each of these five color units, the corresponding average spectra and their coefficients of nine principal components are shown in Fig. 2.8b and Fig. 2.8c, respectively. In terms of spectral shape (Fig. 2.8b), all five of the color units from the MASCS' FCC map (Fig. 2.8a) display a positive spectral slope with two minor absorption features; near ~450 nm and ~740 nm respectively. The spectral feature between 800 nm and 900 nm are due to the systematic uncalibrated instrument artifact (regular channel to channel offset) and not due to the target surface reflectance. In terms of MASCS' spectral reflectance at ~650 nm, Mercury's surface can be broadly divided into three spectral clusters (highest-intermediate-lowest reflectance units):

1) red and magenta units with 650 nm reflectance values of ~ 0.0425 (highest). The overall spectra of the magenta units display a slightly shallower slope compared to the red units.

2) blue units with 650 nm reflectance values of ~ 0.0375 (intermediate)

3) green and cyan units 650 nm reflectance values of ~ 0.0325 (lowest). Spectrally, the slope and the reflectance value of the cyan units are similar to the green units up to ~ 650 nm, and afterwards the spectral slope decreases in comparison.

The average coefficient values of nine principal components representing each color unit in the MASCS PC color composite are plotted in Fig. 2.8c, clearly revealing these three families of spectral units across Mercury's surface.

2.7.1 COMPARATIVE ANALYSIS OF MASCS-DERIVED SPECTROSCOPY, MINERALOGY, AND MORPHOLOGY OF VARIOUS GEOCHEMICAL TERRANES OF MERCURY

The MASCS derived spectral nature of the geochemical terranes on Mercury and its context to inferred surface mineralogy is discussed in detail in the following sub-sections. The indirect mineralogy of these geochemical terranes derived from the MESSENGER geochemical observations using normative mineralogy computation method (Vander Kaaden *et al.*, 2017) and magma crystallization experiments under reducing Mercury conditions (Namur and Charlier, 2017) are summarized in Table 2.1. The following sub-sections discuss the spectral nature of the major geochemical terranes with respect to their representative color units in the MASCS color composite map (Fig. 2.8a, Table 2.1).

(a) Global MASCS Color Composite Map

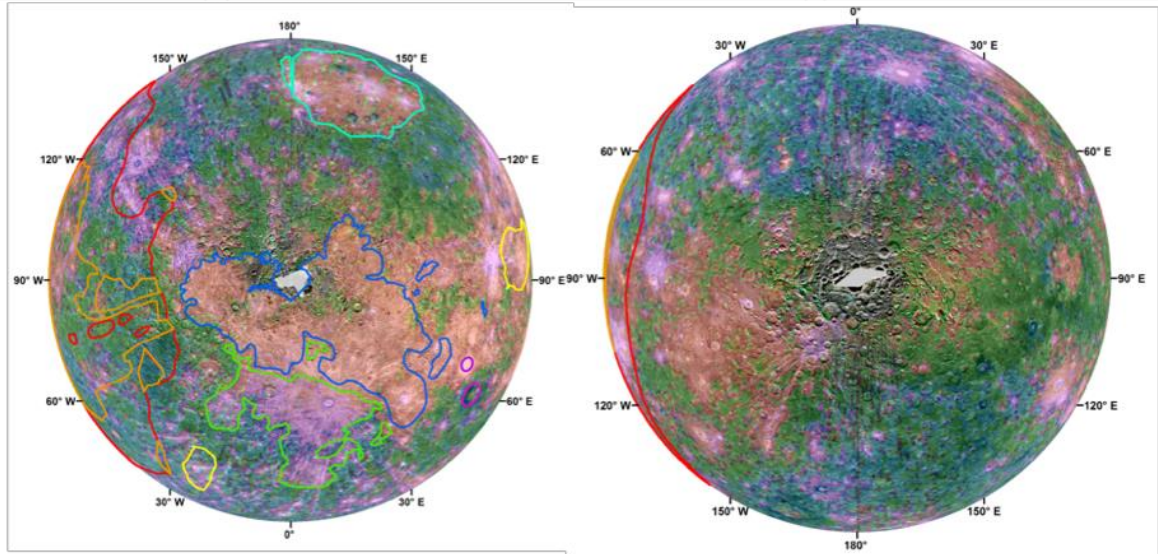
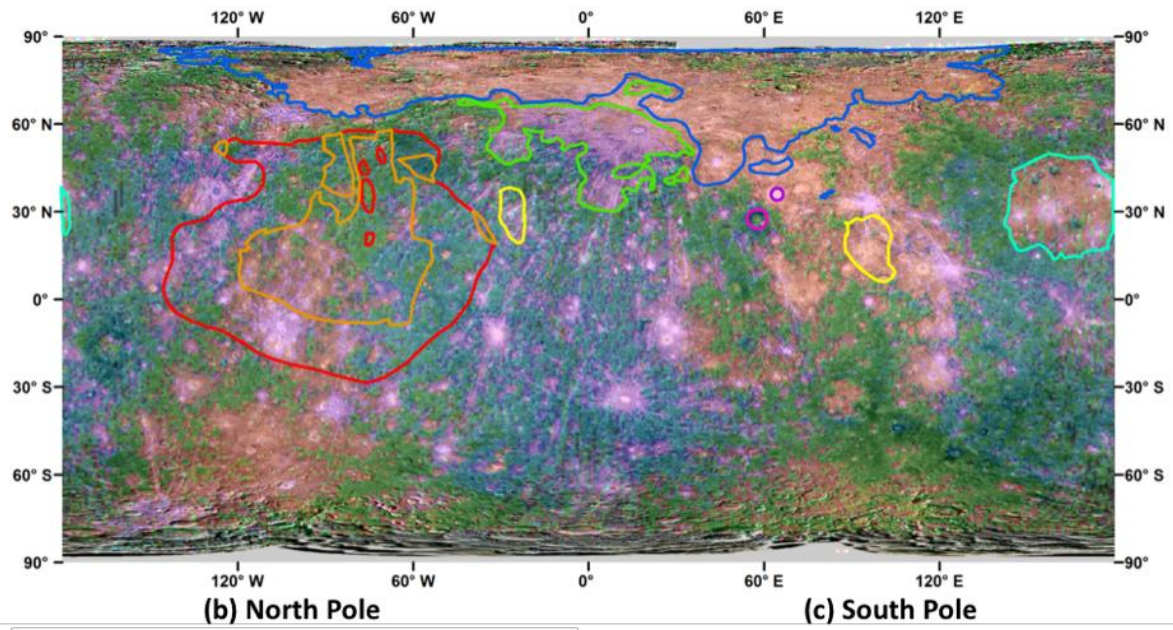

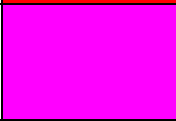
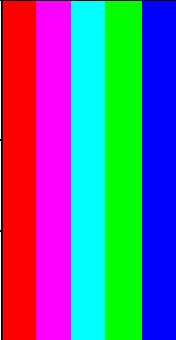
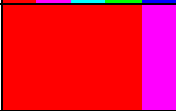






Figure 2.9. a) Global MASCS False Color Composite Map shown in Fig. 2.8a along with the boundaries of nine geochemical terranes defined by Vander Kaaden et al. (2015) overlaid on the MDIS color basemap. b) and c) corresponds to the north and south polar stereographic projection of (a) respectively.

Table 2.1. Comparative analysis of spectral, inferred mineralogical and geochemical units of Mercury from MESSENGER datasets

Geochemical Terranes ^a	*MASCS PC Color units	(Experimental) Silicate Mineralogy ^b				Normative Mineralogy ^a in wt%				
		volcanic	Basement (%)				Plg	Dominant pyx	Ol	sulfides
			Plg	Fo	Di	En				
NP-LMg		dominantly Plg in addition to Fo and Di	>50	10-15	>15	-	>50	Hyp+Diop	<2	~4
NP-HMg							<50	Hyp	~11	~4
HMR		May contain only Fo crystals	<40	>25	>20	<15	<50	Diop	~27	>5
HMR-CaS		-	-				<50	Diop	>30	~6.25
IT		Fo or Fo+Di	>45	-	-	>25	>50	Hyp	<2	~4
CB		-	>60	sub-equal amounts			>50	Hyp	-	~3.14
RB		NA	NA				<50	Diop	~24	>5
PD		NA	NA				<50	Diop	~29	~1.56
HAI – West		NA	NA				>50	Hyp	-	~4
HAI – East		NA	NA							

*Correlation of MASCS PC color units; red (PC1>>PC2~PC6); magenta (PC1~PC6 >> PC2); green (PC2 >> PC1~PC6); cyan (PC2~PC6 >> PC1); blue (PC6 >> PC1~PC2) (See Section 2.7). Note that, for geochemical terranes HMR, HMR-CaS, IT, CB, HAI-West, the representation of the proportions of the color units are not quantitative in order.

^aGeochemical terranes of Mercury surface and its normative mineralogy (Vander Kaaden *et al.*, 2017). Range of Plg is 37.52 % (HMR-CaS) – 58.35 % (NP-LMg)

^bSilicate mineralogy derived from geochemistry laboratory experiments (Namur and Charlier, 2017)

2.7.1.1 ONE COLOR UNITS: NP, RB, PD, HAI-EAST

The geochemical terranes NP-LMg, NP-HMg, RB, PD, and HAI-East each display homogeneous spectral characteristics in the MASCS color composite map (Fig. 2.8a; Table 2.1). Among them, NP is the largest volcanic plains unit on Mercury; hosting two categories of volcanic units: NP-LMg and NP-HMg. These two volcanic units are distinguished purely by the amount of Mg in their chemical composition (Vander Kaaden *et al.*, 2017). In the MASCS FCC map (Fig. 2.8a, 9a), the NP-LMg and NP-HMg terranes are uniquely characterized by two discrete spectral units, the red and magenta units that share boundaries with these geochemical terranes (Vander Kaaden *et al.*, 2017). However, these two terranes are not discernable in the global MDIS color composite map (Domingue *et al.*, 2011, Denevi *et al.*, 2013, Domingue *et al.*, 2015). (Vander Kaaden *et al.*, 2017) suggest that the NP-HMg composition is characterized by a higher presence of orthopyroxenes and olivines than the NP-LMg (Table 2.1). Spectrally, these two terranes share similar shape and reflectance at 650 nm, however, the slope of the NP-HMg (magenta) is slightly lower compared to NP-LMg (red) (Fig. 2.8b) consistent with the compositional difference proposed by (Vander Kaaden *et al.*, 2017).

Geochemically, RB and PD share roughly similar inferred silicate mineralogies with plagioclase, diopside, and olivine, however they differ in the abundance of sulfides (Table 2.1). RB is a ~3.6 Ga old basin (D=305 km, centered 27.39°N 58.56°E) hosting some of the youngest lava flows on Mercury (Marchi *et al.*, 2011). PD is located NE of RB and contains some of the brightest and largest pyroclastic deposits, which are associated with Nathair Facula (centered 35.97°N 65.47°E). At this spatial resolution in the MASCS FCC map (Fig. 2.7a), PD displays a red color similar to the NP-LMg region while RB displays a green color associated with PC2, that represents space-weathered, older Mercury terranes. Spectrally, PD and RB terranes represent the two extreme spectral unit endmembers, highest and lowest 650 nm spectral reflectance, respectively (Fig. 2.8b; red, green). On the other hand, HAI in the eastern longitude (HAI-East) shares similar MASCS color characteristics as PD (red), however, HAI differs significantly in its derived mineralogy, as it is associated with the absence of olivines and comparatively greater amounts of sulfides (Table 2.1).

2.7.1.2 TWO-COLOR UNITS: CB, HAI-WEST

Geochemically, CB and HAI-West have very similar inferred mineralogies; with plagioclase, clinopyroxenes, 3-4 wt% sulfides, and no olivine component (Table 2.1). However, in the MASCS FCC map (Fig. 2.8a, 9a; Table 2.1), CB and HAI-west are dominated by red and magenta units, respectively. This suggests that PC1 is a major spectral component for both CB and HAI-west regions, as is also apparent for the HAI-east region (see section 2.7.1; Table 2.1). Within CB (Fig. 2.9a), the bright-rayed ejecta craters and fresh bright hollow materials are displayed as magenta units whereas dark-floor crater Atget is displayed as a cyan unit due to contributions from PC6 (see Section 2.6.3; Fig. 2.7c). However, in the case of HAI-west, there are no clear morphological boundaries between the magenta and cyan units (Fig. 2.9a).

2.7.1.3 MULTI-COLOR UNITS: HMR, HMR-CAS, IT

Morphologically, HMR, including HMR-CaS, terranes are not distinguishable from the older Mercury IT terranes (IT). Nevertheless, geochemical analysis shows that HMR possess the planet's highest Mg abundance (Vander Kaaden *et al.*, 2017). Table 2.1 shows that both HMR and HMR-CaS regions are dominated by clinopyroxenes (diopside) and contain <50 wt% plagioclase, > 25 wt% olivine, and >5 wt% sulfides. Whereas, IT is dominated by orthopyroxenes (hypersthene) and contain >50 wt% plagioclase, <2 wt% olivine, and ~4 wt% of sulfides (Table 2.1). In the MASCS FCC map (Fig. 2.8a; Table 2.1), all three terranes display heterogeneous spectral characteristics, containing all five PC color units, irrespective of their geochemical and mineralogical differences. This suggests that these terranes possess complex geology units, comprised of diverse surface materials with varying silicate mineralogies.

2.8 SUMMARY AND CONCLUSIONS

In this study, we produced a global hyperspectral cube of uniform equal-angular (1 ppd) and spectral resolution from the MASCS observations and applied both standard spectral ratio, slope, and multivariate spectral analysis techniques to understand the compositional and textural diversity of Mercury's regolith. Among the standard spectral analyses, we created visible-slope and visible-slope normalized maps, which highlighted the PD deposits, CB, and

the NP regions. UV-downturn examinations did not differentiate any particular spectral units due to the very coarse spatial resolution of the MASCS datacube.

Among the multivariate spectral analysis techniques, the k-means clustering results revealed three major spectral classes (Fig. 2.4) where blue units (cluster=0) mainly consists of the underlying material within intercrater terrane (IT) including low reflectance material (LRM), orange units (cluster=1) represents the regions surrounding the magenta units (cluster=2) along with the northern plains (NP), and the floor of Caloris basin (CB), and the magenta units (cluster=1) represents the major part of the NP, the bright materials inside CB, and the bright rayed fresh craters and volcanic materials within the IT. However, K-means clustering spectrally could not differentiate the high-Mg (NP-HMg) and low-Mg regions (NP-LMg) of northern plains.

On the other hand, the FCC map made from the principal component analysis (PCA) highlighted variations associated with reflectance, unit age, and regolith texture. Some of the key highlights from this PC color composite analysis includes:

a) Irrespective of the varying geochemical and formation history of the NP-LMg, CB, PD, and HAI-E geochemical units, their spectral properties derived from PCA are similar (Fig. 2.8a, 9a). This suggests that PCA results may correspond closely with similar physical properties of the surface materials (regolith) of these geochemical terranes rather than their chemical composition.

b) Though RB is predominantly characterized by the green FCC unit, closer inspection finds one pixel of the red (PC1) unit in the basin center and one also sitting on top of the pyroclastic deposits (Suge Facula; 26.09°N 59.68°E) near the southern-eastern rim, in addition to a cyan pixel along the rim (Fig. 2.8a, 9a). This suggests some geochemical heterogeneity within the RB terrane.

c) NP-HMg is the only geochemical terrane that is predominantly associated with the magenta FCC unit, whereas the HAI-west geochemical unit displays both magenta and green FCC units.

d) One of the key findings of the MASCS FCC map is the clear distinction between the NP-LMg (red FCC unit) and NP-HMg (magenta FCC unit) terranes, which is the first spectrally

derived distinction between the two geochemical units. This distinction is not observed in the k-means cluster analysis and associated map.

e) Fig. 2.9a clearly shows that the magenta FCC units mainly represent bright-rayed, fresh craters and fresh hollow materials. Cyan FCC units represent some of the darker LRM observed along the rim of the basins. These correlations suggest that, the PCA results are more representative of the physical properties of the regolith rather than its chemical composition. PCA tends to identify regions associated with freshly exposed materials.

f) Among the geochemical terranes, the IT, HMR and HMR-CaS display mixed, heterogeneous characteristics in the MASCS FCC (Fig. 2.8a, 9a), suggesting both physically and compositionally heterogeneous properties.

Among the multivariate analysis adopted in this study, the principal component analysis (PCA) of MASCS data proves to be an efficient tool which brings out the spectral heterogeneity among the various geochemical terranes of Mercury. One of the major results of this study is the distinction between the low- and high-Mg terranes of the northern volcanic plains seen in the FCC map. However, a direct investigation of the surface mineralogy is still missing. In order to achieve this, the spectral range beyond the VNIR coverage provided by MESSENGER is required. Here the ESA/JAXA BepiColombo mission can build and extend on MESSENGER. The mid-infrared (MIR; 7-14 μm) spectral region could provide a direct measure of the Si-O abundance of the bulk silicate mineralogy, in addition to identifying the sulfide mineralogy within the hollows. This will be achieved by the MERTIS spectrometer onboard the BepiColombo mission to Mercury. The radiometer channel of MERTIS will investigate the regolith physical properties, such as grain size and thermal inertia, and test the correlation of PC6 with fine-grained, least space-weathered surface materials. VNIR data from the SIMBIO-SYS-VIHI will further add to our understanding of Mercury's VNIR spectral characteristics with its mapping at a higher spatial resolution. In preparation for the BepiColombo measurements at Mercury, future analysis of the MASCS data will focus on detailed spectral mapping of localized surface units, based on the results from this study. In addition, laboratory spectral measurements of fresh and thermally weathered Mercury analogue materials in the VNIR will be used to derive plausible mineral components within the hollows, volcanic materials, and LRM in preparation for the discoveries by BepiColombo. With BepiColombo on its way to Mercury, the global multivariate analysis of the very high spatial resolution hyperspectral

VNIR+MIR data from SIMBIO-SYS VIHI and MERTIS will further help to understand the spectral and mineralogical diversities within various geochemical units of Mercury.

2.9 ACKNOWLEDGEMENTS

The authors would like to thank Dr. Myriam Lemelin and the anonymous reviewer for the constructive reviews that improved the paper. I. Varatharajan thank the DLR/DAAD Doctorate Fellowship for funding her PhD work at PSL-DLR. D. Domingue was supported by NASA's Solar System Workings (SSW) Program, grant 80NSSC18K0521. All MESSENGER data used in this paper are publicly available at the NASA Planetary Data System (PDS).

2.10 SUPPORTING INFORMATION

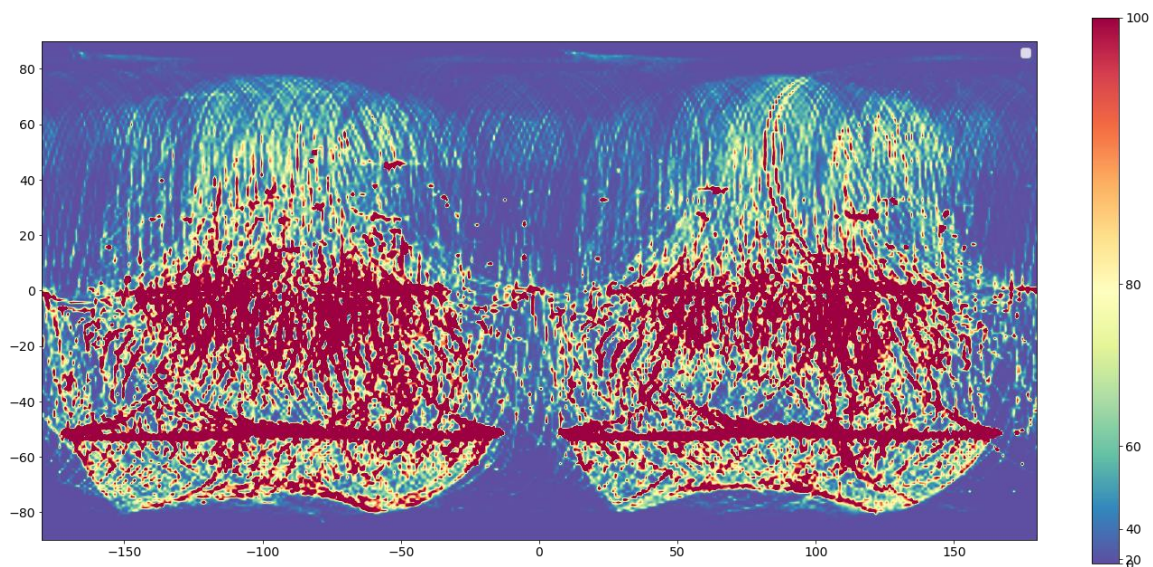


Figure 2.10. The available number of MASCS spectra per pixel ($1^\circ\text{lat} \times 1^\circ\text{lon}$) used to create the resulting global MASCS spectral cube represented on the colormap which uses power law scale ($y=xy$, where $y=3$). Figure highlights the non-uniform spatial distribution of available MASCS spectra per pixel per degree (which is equivalent of ~ 42.5 km/pixel along the equator). In order to create the global MASCS datacube of uniform spatial resolution of 1 pixel per degree used in the study, the median of the spectra falling within this angular resolution of $1^\circ\text{lat} \times 1^\circ\text{lon}$ is computed.

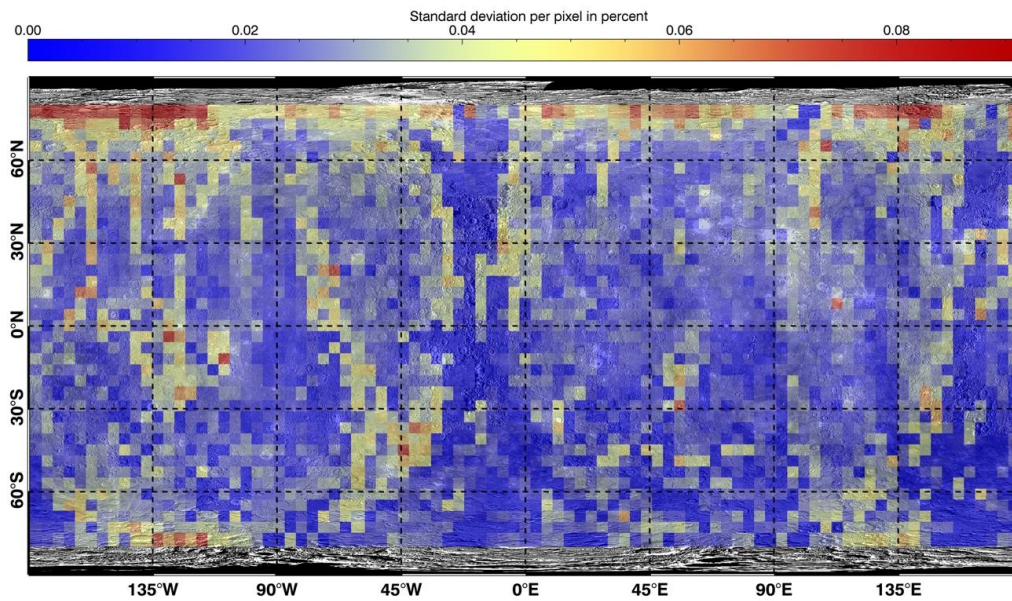


Figure 2.11. Shows the variability map at 700 nm. Variability here is defined as standard deviation of the reflectance at 700 nm in percentage for the available MASCS spectra per pixel (1°lat x 1°lon) as shown in Fig. 2.10. Figure shows that only the regions approaching the limited $\pm 80^\circ$ latitudes show high variability due to the highly variable observational geometry in these zones.

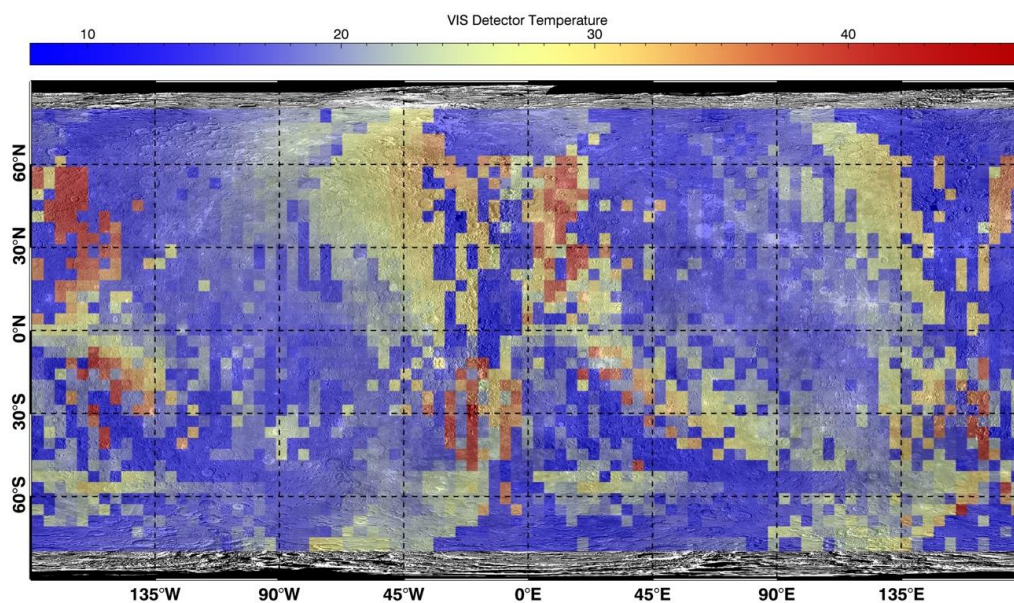


Figure 2.12. Shows the distribution of visible detector temperature for all observations used in this study. These distribution does not produce any of the features seen in global maps including the variability map in Fig. 2.11. This further confirms that there are no instrumental artifacts that affects the spectral analysis in the study. The visible detector temperature data is available in the downloaded MASCS spectra from PDS.

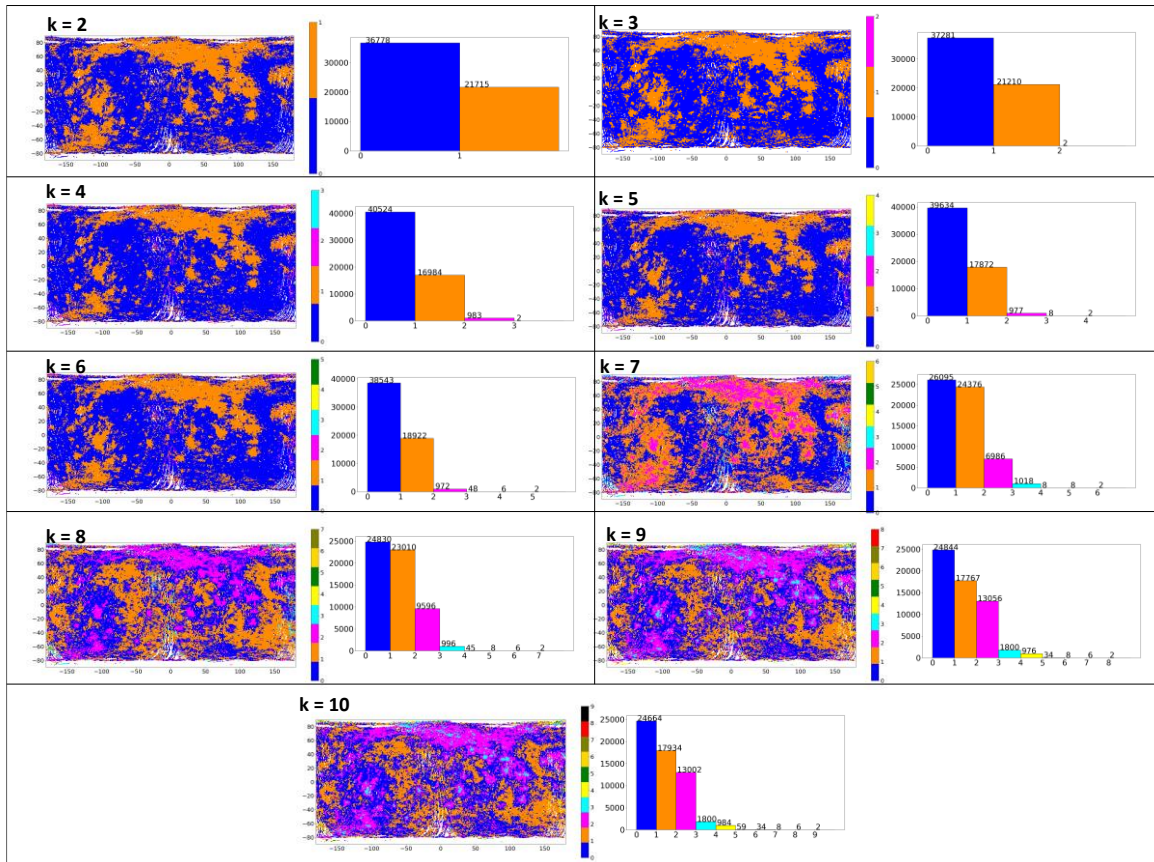


Figure 2.13. Shows the random K-means clustering map for each k values i.e., number of clusters where $k=2,3,4,5,6,7,8,9,10$ and its corresponding histogram showing the number of pixels per cluster for each k. It shows that irrespective of the k value, most of Mercury surface fall into three contiguous regions for $k=7$ to 10.

3

THE PLANETARY SPECTROSCOPY LABORATORY (PSL) – WIDE SPECTRAL RANGE, WIDER SAMPLE TEMPERATURE RANGE

A. Maturilli¹, J. Helbert¹, M. D'Amore¹, **I. Varatharajan**^{1,2}, Y. Rosas Ortiz¹

¹*Department of Planetary Laboratories, Institute of Planetary Research, German Aerospace Center (DLR), Berlin, Germany,* ²*Institute of Geological Sciences, Freie University (FU) Berlin, Germany*

Published in SPIE Proceedings 10765, Infrared Remote Sensing and Instrumentation XXVI, September 2018

DOI: <https://doi.org/10.1117/12.2319944>

The author contribution is explained in the Section 1.3.

4

SPECTRAL BEHAVIOR OF SULFIDES IN SIMULATED DAYTIME SURFACE CONDITIONS OF MERCURY: SUPPORTING PAST (MESSENGER) AND FUTURE MISSIONS (BEPICOLOMBO)

I. Varatharajan^{1,2}, A. Maturilli¹, J. Helbert¹, G. Alemanno¹, H. Hiesinger³

¹Department of Planetary Laboratories, Institute of Planetary Research, German Aerospace Center (DLR), Berlin, Germany, ²Institute of Geological Sciences, Freie University (FU) Berlin, Germany, ³Institut für Planetologie, Westfälische Wilhelms-Universität Münster, Germany

Published in Earth and Planetary Science Letters (EPSL), May 2019

DOI: <https://doi.org/10.1016/j.epsl.2019.05.020>

The author contribution is explained in the [Section 1.3](#).

KEY POINTS

- Emissivity of sulfides under simulated Mercury Daytime conditions is studied
- Reflectance of fresh and thermally processed sulfides at wide spectral range (0.3-100 μm) is measured.
- Sulfides show strong and distinct spectral features in thermal IR (7-14 μm) spectral region
- UVVIS (0.3-0.6 μm) spectral region is immune to thermal weathering for sulfides

4.1 ABSTRACT

To detect the mineral diversity of a planet's surface, it is essential to study the spectral variations over a broad wavelength range at relevant simulated laboratory conditions. The MESSENGER (Mercury Surface, Space Environment, Geochemistry, and Ranging) mission to Mercury discovered that irrespective of its formation closest to the Sun, Mercury is richer in volatiles than previously expected. This is especially true for sulfur (S), with an average abundance of 4 wt%. It has been proposed that sulfur in the interior of Mercury can be brought to the surface through volcanic activity in the form of sulfides as slag deposits in Mercury hollows and pyroclastic deposits. However, comprehensive spectral library of sulfide minerals measured under vacuum conditions in a wide spectral range (0.2-100 μm) was lacking. This affects the detectability and understanding of the distribution, abundance, and type of sulfides on Mercury using remote-sensing spectral observations. In the case of Mercury, the effect of thermal weathering affecting the spectral behavior of these sulfides must be studied carefully for their effective detection. In this study, we present a spectral library of synthetic sulfides including MgS, FeS, CaS, CrS, TiS, NaS, and MnS. For each sample, we performed emissivity measurements in the thermal infrared range (TIR: \sim 7-14 μm) for sample temperatures from 100°C-500°C, covering the daytime temperature cycle on Mercury's surface. In addition, for each sample we measured the spectral reflectance of fresh and thermally processed sulfides over a wide spectral range (0.2-100 μm) and at four different phase angles, 26°, 40°, 60°, 80°. This spectral library facilitates the detection of sulfides by past and future missions to Mercury by any optical spectrometer of any spectral range. Specifically, the emissivity measurements in this study will support the Mercury Radiometer and Thermal Imaging Spectrometer (MERTIS) instrument on the ESA/JAXA BepiColombo mission, which will study the surface mineralogy over a wavelength range of 7-14 μm at a spatial resolution of 500 m/pixel. The measured reflectance of these sulfides in 0.2-100 μm at various phase angles will support the interpretation of measurements from past (MDIS, MASCS on MESSENGER) and future missions (SIMBIO-SYS on BepiColombo).

4.2 INTRODUCTION

The Gamma Ray Spectrometer (GRS), X-Ray Spectrometer (XRS), Neutron Spectrometer (NS), Mercury Atmospheric and Surface Composition Spectrometer (MASCS), and Mercury Dual Imaging Spectrometer (MDIS) of NASA's MESSENGER (Mercury Surface, Space Environment, Geochemistry, and Ranging) mission mapped the surface chemistry and mineralogy of the Mercury from 2011-2015. The MASCS instrument had two channels, mapping the surface at high phase angles ($>80^\circ$) and spatial resolution of 100m - 7.5km; a) ultraviolet-visible spectral region (UVVIS; 0.115-0.6 μm) at 1 nm spectral resolution and b) visible (VIS: 0.3-1.025 μm) -infrared (IR: 0.95–1.45 μm) spectral region (VIRS) at 5nm spectral resolution.

MESSENGER revealed that Mercury (unlike the Moon) has been formed in a highly reducing environment with high magnesium and surprisingly high sulfur abundances (Nittler *et al.*, 2011). (Namur *et al.*, 2016) performed high temperature and high to low pressure experiments to study the sulfur solubility in materials representative of Mercurian lavas (reduced mafic silicate melts) to understand the nature of S brought to the surface, i.e., either as sulfide minerals or sulfur itself during their ascent. Interestingly, the study concluded that Mercurian lavas did not carry sulfide melts based on the lack of spectral evidence of sulfides detected by MESSENGER. In an earlier study, the Planetary Spectroscopy Laboratory (PSL) performed measurements on VIS-IR reflectance of MgS, CaS, MnS powdered samples at Mercury's daytime temperature (500°C), in vacuum, and at a high phase angle (80°) to search for their detection in hollows and pyroclastic deposits (Helbert *et al.*, 2013a), and therefore support the presence of sulfides. Based on this laboratory work, the presence of low-density MgS was reported at two hollows from MDIS data (Vilas *et al.*, 2016) .

Sulfide minerals have long been proposed as components of Mercury's regolith (Sprague *et al.*, 1995). The thermochemical and experimental evidence indicates that CaS is the major lithophile sulfide on Mercury and sulfides in the shallow regolith probably include major amounts of FeS and CaS with minor MnS and NaCrS₂ (Vaughan, 2013). Correlations between Fe, Ca, and S abundances (as well as largely uncorrelated Mg and S abundances) in MESSENGER's XRS data suggest that relevant abundances of FeS and CaS are present in Mercury's regolith (Nittler *et al.*, 2011, Weider *et al.*, 2016). MESSENGER also suggests the

presence of MnS, FeS, CrS, and TiS on the surface (Vander Kaaden *et al.*, 2017). Global mapping of the mineral diversity and spatial heterogeneity of these sulfide minerals will therefore help improve the numerical models that study the chemical and thermal evolution of Mercury.

The Mercury Planetary Orbiter (MPO) of ESA/JAXA's BepiColombo mission to Mercury will carry two spectrometers to map Mercury's surface at nadir conditions (phase angle <20°). The Mercury Radiometer and Thermal infrared Imaging Spectrometer (MERTIS), which will map the emissivity of surface minerals in the spectral range of 7-14 μm at a spectral resolution of 90nm and a spatial resolution of 500m/pixel (Hiesinger *et al.*, 2010). The visible–near-infrared imaging spectrometer (VIHI) of the Spectrometer and Imagers for MPO BepiColombo – Integrated Observatory SYStem (SIMBIO-SYS), will map the surface mineralogy in the spectral range of 0.4-2 μm at a spectral resolution of 6.25nm and spatial resolution of 100-375m/pixel (Flamini *et al.*, 2010).

To effectively detect sulfides using these spectrometers or any future spectrometer, it is essential to understand the spectral behavior of possible sulfides under simulated Mercury conditions for different phase angle settings. In this study, we measured the emissivity of these sulfides at five temperatures (100, 200, 300, 400, 500°C) in the spectral range of 7-14 μm . These measurements directly support the sulfide detection by MERTIS. We then measured the spectral reflectance of these sulfides from low to high phase angles (26-80°) for both fresh (before heating) and thermally processed (500°C) sulfides for the wide spectral range of 0.2-100 μm , thereby supporting the sulfide detection by visible-NIR spectrometers onboard MESSENGER (MASCS and MDIS) and BepiColombo (SIMBIO-SYS/VIHI) missions.

In summary, the study covers laboratory measurements of the emission spectra of different, chemically pure, synthetic sulfides over a spectral range of 7 - 14 μm for temperatures from 100°C to 500°C and the reflectance values of both fresh and thermally weathered samples after emissivity measurements covering a spectral range of 0.2 - 100 μm over the phase angles of 26°, 40°, 60°, 80°. It is important to note that the band assignments of spectral features of the fresh and thermally weathered sulfides from UV-FIR reflectance and MIR emissivity measurements is not well documented. The experimental data on stability diagrams of the sulfide phases that support the change in thermal spectral behavior of these sulfides upon heating under vacuum is least understood (Dilner, 2016). Future work of this

study will focus on the X-ray diffraction of the fresh and thermally-weathered sulfides to better understand the change in spectral behavior of these sulfides upon heating at Mercury surface conditions.

4.3 SAMPLES

Guided by results provided by the geochemistry suite on MESSENGER, we selected the following sulfides for this study; iron sulfide (FeS), calcium sulfide (CaS), chromium sulfide (CrS), titanium (IV) disulfide (TiS₂), disodium sulfide (Na₂S), manganese (II) sulfide (MnS), and magnesium sulfide (MgS) from two vendors (MgS-1 and MgS-2). The measurements are carried out on synthetic samples of at least 99% purity procured from certified industrial suppliers (Table 4.3 in the supplementary material). Using pure synthetic samples mitigates uncertainties and ambiguities introduced by impurities present in natural samples. Mercury's regolith is generally composed of very fine particles (e.g., (Shevchenko, 2002, Domingue *et al.*, 2014b), therefore, we used powdered sulfide samples having grain sizes of about ~10 μm for this study.

4.4 METHODS

The emissivity of the synthetic sulfides in the thermal infrared (TIR) spectral region is measured as a function of the varying Mercury daytime temperatures (100-500°C) in vacuum. During this process, these sulfides are continuously monitored using a webcam to study the chemical, physical, and morphological weathering of fresh sulfides to their thermally processed/weathered (T-processed) counterparts. Before and after the emissivity measurements, the reflectance of both fresh and then T-processed sulfides are measured at room temperature in vacuum over a wide wavelength range including ultraviolet (UV), visible-near infrared (VIS/NIR), TIR, and far infrared (FIR) for varying phase angles (26°-80°).

4.4.1 FACILITY – PLANETARY SPECTROSCOPY LABORATORY (PSL)

PSL is located at the Institute of Planetary Research (PF) at the German Aerospace Center (DLR) in Berlin, Germany. Over more than 15 years, the PSL has been operating in

various configurations to provide emissivity, reflectance, and transmission spectra of various rocks/minerals for the study of planetary and minor bodies surfaces (Maturilli *et al.*, 2008, Helbert and Maturilli, 2009, Sprague *et al.*, 2009, Helbert *et al.*, 2013a, Helbert *et al.*, 2013b). Fig. 4.1 shows the current PSL setup. Details of the emissivity and reflectance spectroscopy setups at PSL are described in Section 4.9.1 in the supplementary material. All of the spectral measurements of sulfides were performed at the PSL. A graphical flowchart of the methodology is shown in Fig. 4.2(top) and is detailed below.

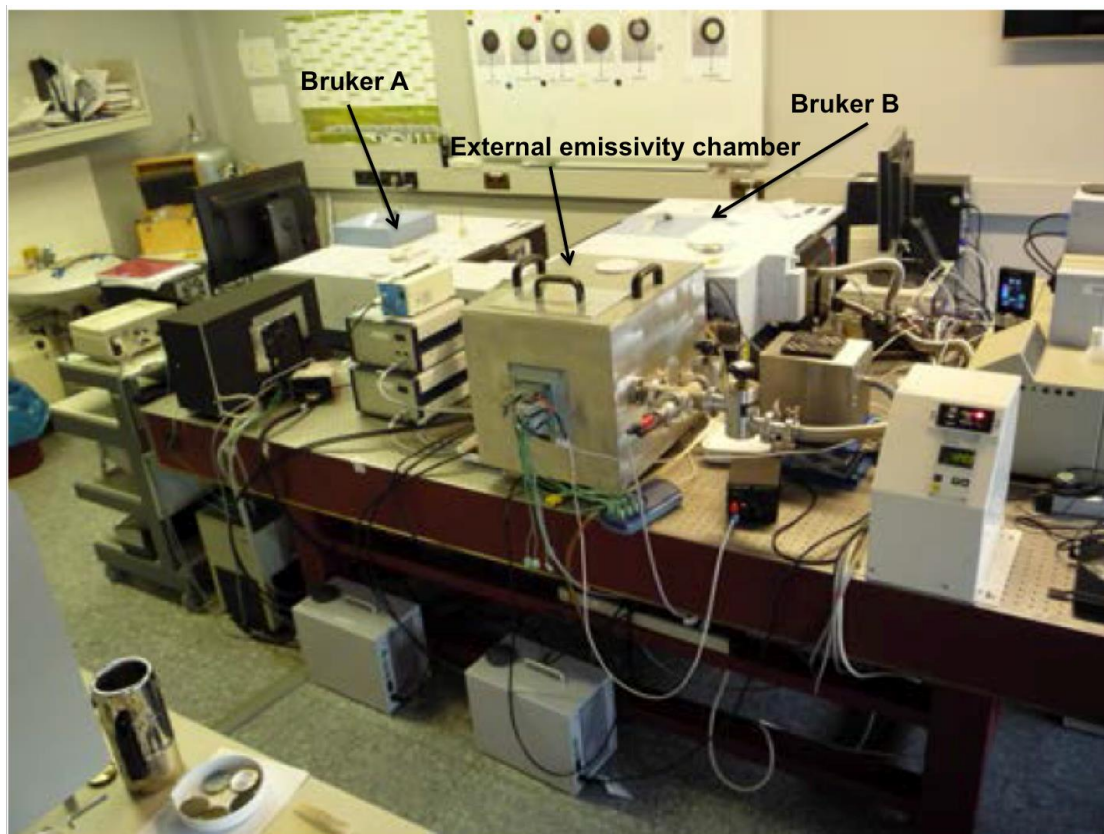


Figure 4.1. Laboratory set-up at PSL. Both Bruker A and Bruker B are Bruker Vertex 80V FTIR spectrometers. Bruker A is optimized for measurements in UV, VIS-IR, TIR spectral range and Bruker B is optimized for measurements in FIR spectral range. Bruker B is also attached to an external emissivity chamber for direct emissivity measurements at very high temperatures. The detectors and beamsplitters used for collecting spectra at respective spectral ranges are tabulated in Table 4.4 in supplementary file.

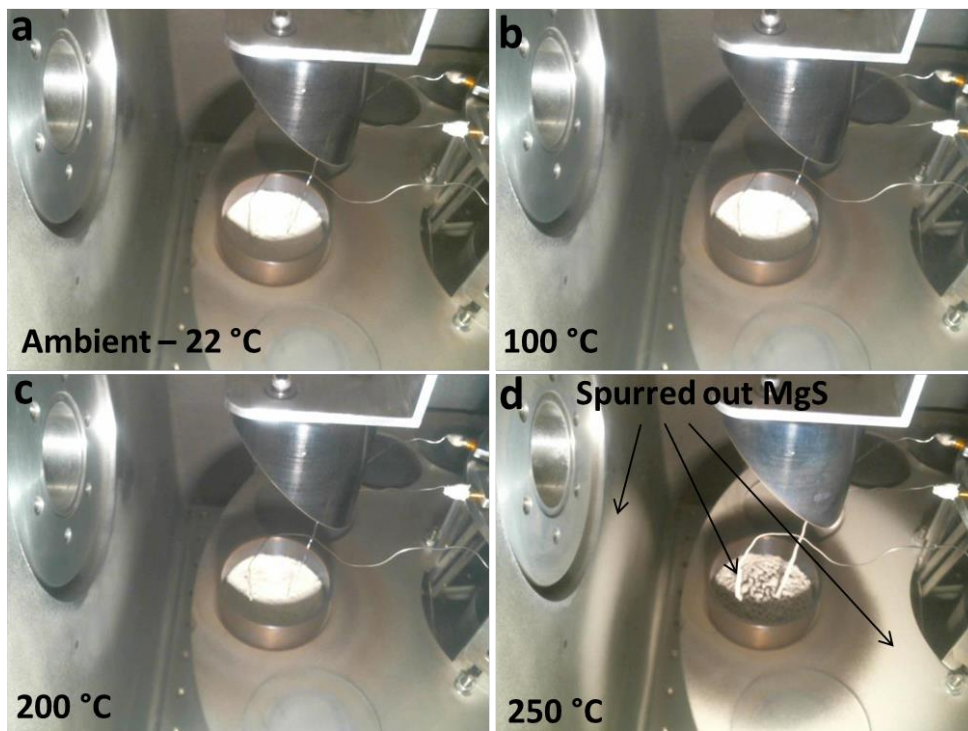
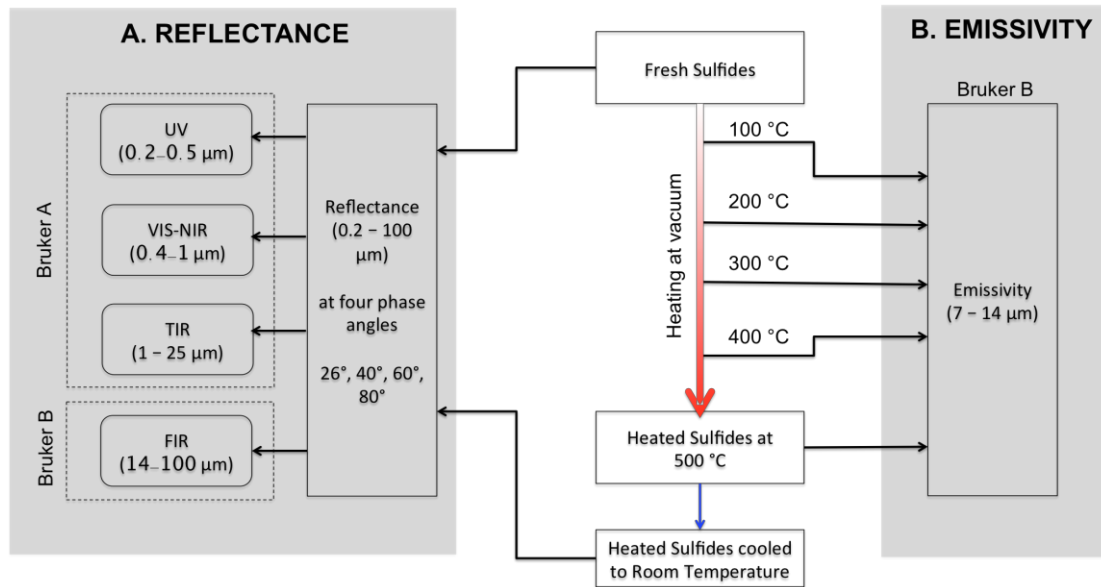


Figure 4.2. (Top) Graphical summary of the methodology used in the study to measure the emissivity and reflectance spectra. (Bottom) a) Experiment setup before heating any sample (in this case MgS), b) MgS at 100 °C, c) MgS at 200 °C, d) MgS spurred out while reaching the temperature of 250 °C which is deposited in the side wall, thermophiles, and the rotating carousel.

4.4.2 EMISSIVITY

The measurement of the emissivity of the sulfides will facilitate their detection by MERTIS. To achieve this spectral need, the Bruker Vertex 80V (Bruker B see Fig. 4.1) with a MCT HgCdTe detector (cooled by liquid nitrogen) and KBr beamsplitter (see Table 4.4 in the supplementary material) was used to measure emissivity in the spectral range of 700–1400 cm^{-1} ($\sim 7\text{--}14\ \mu\text{m}$) at a spectral resolution of 4cm^{-1} . This spectrometer is attached to an external chamber where the sulfides are placed in stainless steel cups as described in (Helbert *et al.*, 2013a). Induction heats the whole sample cup to a homogenous temperature effectively suppressing thermal gradients in the sample. The experimental setup for emissivity measurements is shown in Fig. 4.2(bottom). Samples were heated from 100 to 500°C (100°C steps) in vacuum and emissivity is measured at each step (for details Section 4.9.2 of the supplementary material). At the end of the measurements, all the sulfides are thermally processed (T-processed) under peak Mercury daytime temperature.

4.4.3 REFLECTANCE

For the detection of sulfides by reflectance spectrometers (e.g., MDIS and MASCS UV-VIS, VIS-IR spectrometers in MESSENGER, SIMBIO-SYS/VIHI on BepiColombo) and to understand their spectral behavior changes across wide wavelength regions due to exposure to extremely high temperatures at wide wavelength regions, the reflectance of both fresh and thermally processed sulfides were measured under varying phase angle conditions.

In this study, we collected biconical reflectance spectra of fresh and thermally processed sulfides in the whole spectral range ($\sim 0.2\text{--}100\ \mu\text{m}$) using both instruments: the Bruker A (see Fig. 4.1 & Fig. 4.2) spectrometer for the UV, VIS-IR, and TIR spectral range (0.2–25 μm) and the Bruker B spectrometer for the FIR spectral range ($\sim 16\text{--}100\ \mu\text{m}$). The details of the beamsplitter and detector used for each spectral subset are tabulated in Table 4.4. The reflectance of fresh and thermally processed sulfides was measured using a spot size of 2mm at phase angles 26°, 40°, 60°, and 80° at a spectral resolution of $\sim 4\text{cm}^{-1}$. The references used for calibration in each spectral range are listed in Table 4.4. The measured reflectance spectrum of each sulfide at each phase angle is divided by the corresponding reflectance spectrum of the reference at the respective phase angle. For details on reflectance measurements, see Section 4.9.3 of the supplementary material.

4.5 RESULTS

The results of emissivity and reflectance spectroscopy of sulfides from this study are discussed in the following subsections.

4.5.1 EMISSIVITY

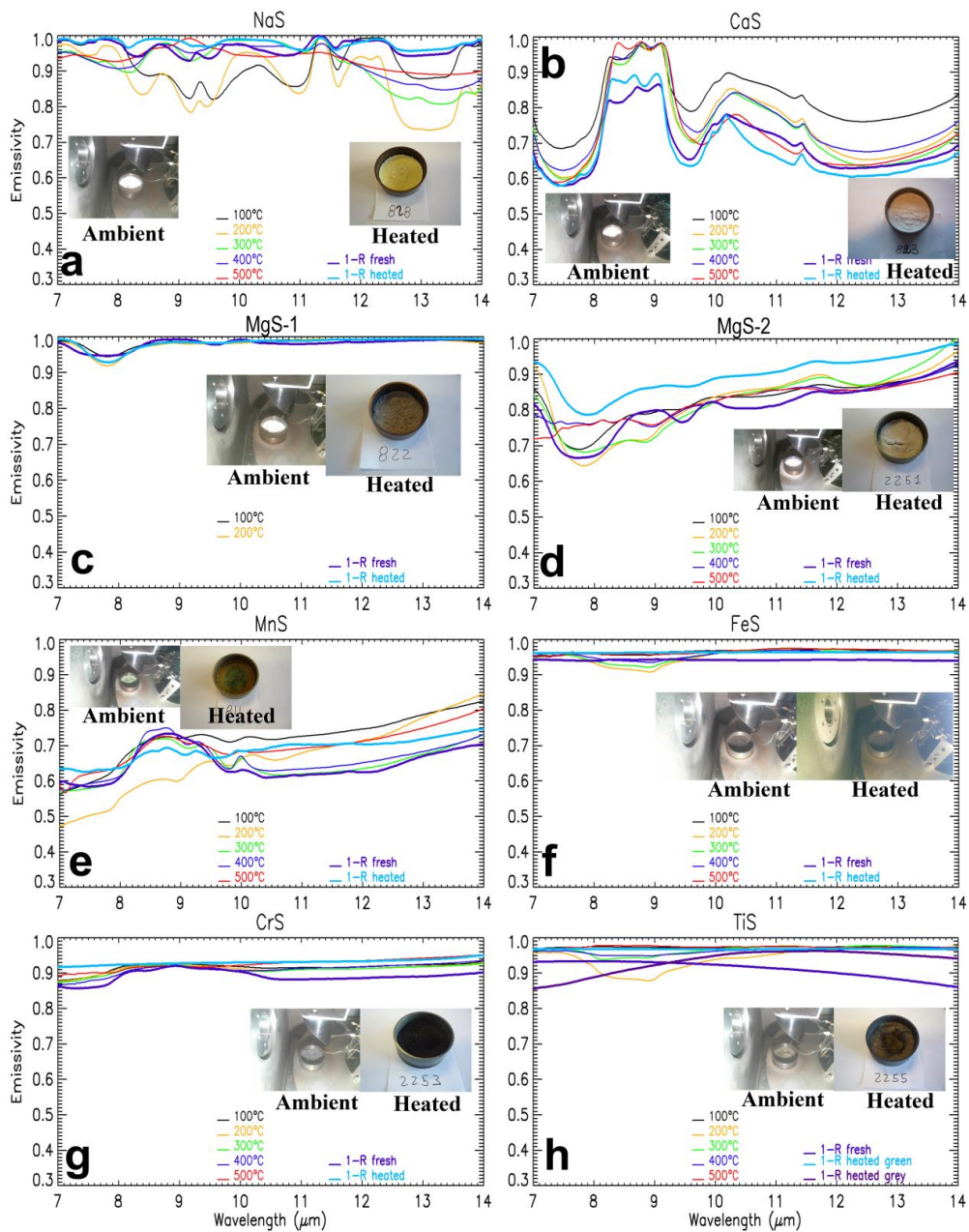


Figure 4.3. Emissivity of the sulfides measured at 100 °C, 200 °C, 300 °C, 400 °C, and 500 °C at spectral range of 7-14 μm. The emissivity spectra is also compared with the emissivity derived from the reflectance measurements ($E=1-R$; Kirchhoff's law) for the fresh and heated sulfides.

The emissivity spectra of all sulfides measured at 100°C, 200°C, 300°C, 400°C, and 500°C for the spectral range 7-14 μm are plotted in Fig. 4.3. These emissivity measurements are also compared with the derived emissivity spectra from reflectance measurements (emissivity=1-reflectance; Kirchhoff's law) for both fresh and heated sulfides (Fig. 4.3). The reflectance measurements are taken using the Bruker A and B and the experimental parameters are listed in the MIR (reflectance) column of Table 4.4. For each sulfide sample studied, changes in the spectral absorption bands with respect to the temperature are observed (e.g., Fig. 4.3a, NaS). Emissivity as a function of temperature for each sulfide samples is discussed below.

Among all the samples studied, CaS and MgS alone show noticeable spectral features after T-processing.

- 1) Sodium sulfide (NaS, Fig. 4.3a) shows a very dynamic change in its emissivity spectra with temperature. The dynamic behavior of the emissivity spectra is strongly correlated with the change in color of the samples throughout the experiment (Fig. 4.3a; ambient and heated).
 - a) 100°C: The emissivity of NaS measured at 100°C shows three strong absorption features and two minor bands; the three strong absorption features include, a) a broad four-component absorption feature having spectral shoulders at 7.9 and 11.3 μm with the spectral bands centered near 8.4, 9.2, 9.5, 11 μm , b) a narrow but sharp absorption feature centered at 11.6 μm , and c) a single broad absorption centered at 13 μm (with spectral shoulders at 12.4 and 13.7 μm); and two minor bands centered near 7.5 and 13.9 μm .
 - b) 200°C: When the temperature is increased to 200°C, a) the spectral absorption feature near 8.4 μm sharpens and slightly shifts to shorter wavelength, b) the 9.2 μm feature shifts to slightly longer wavelength and the 9.5 μm feature shifts to slightly shorter wavelength, therefore, forming a doublet feature near 9.3 μm , c) the 11.6 μm feature sharpens and is slightly extended to longer wavelength, d) the 13 μm feature strongly increases in strength up to ~25% absorption and the minor bands near 7.5 and 13.9 μm are slightly strengthened.
 - c) 300°C: With the increase in temperature to 300°C, the overall depth of the spectral features is reduced and the spectral bands tend to merge together. The band near 7.5

μm shifts to longer wavelength, and the band near $8.4 \mu\text{m}$ shifts to shorter wavelength, therefore forming a broad two-component absorption with spectral shoulders at 7.1 and $8.8 \mu\text{m}$. The two absorption bands near 9.2 and $9.5 \mu\text{m}$, merge together to form a single wider band centered near $9.2 \mu\text{m}$. The sharp band near $11.6 \mu\text{m}$, the broad $13 \mu\text{m}$ and a minor $13.9 \mu\text{m}$ bands merge together to form a broad band with the spectral shoulder at $11.4 \mu\text{m}$.

- d) 400°C : When the temperature is further increased to 400°C , the converged bands from 300°C spectra are further smoothed.
 - e) 500°C : The absorption band near $9.2 \mu\text{m}$ completely disappears. The final spectrum has three broad minor absorption features around 8 , 10 , and $13 \mu\text{m}$ with spectral shoulders near 9.2 and $11.3 \mu\text{m}$.
 - f) *Comparison with reflectance measurement*: The derived emissivity ($e=1-R$) from room temperature reflectance measurements (MIR measurements using Bruker A) of fresh samples gives us a very flat spectra with minor spectral bands near 7.3 , 8.3 , 9.1 , 9.5 , 10.8 , 11.6 , and a broad $13 \mu\text{m}$ absorption. The derived emissivity of heated samples from reflectance measurements at room temperature shows similar spectral behavior to derived emissivity from fresh samples, where a) the $8.3 \mu\text{m}$ band shifts to shorter wavelength to $8.1 \mu\text{m}$, b) 9.1 and $9.5 \mu\text{m}$ bands merge to form a broad minor band near $9.3 \mu\text{m}$, and c) the $10.8 \mu\text{m}$ band shifts to longer wavelength to $11.1 \mu\text{m}$.
- 2) Calcium sulfide (CaS, Fig. 4.3b) proves to be the most stable sulfide on the Mercury's surface with emissivity spectra retaining their characteristic absorption features for both fresh and heated CaS samples. In general, measured emissivity spectra of CaS samples possess characteristic spectral bands near $7.5 \mu\text{m}$, a doublet near $8.8 \mu\text{m}$ with spectral shoulders at 8.3 and $9.1 \mu\text{m}$, a slightly narrower at $9.6 \mu\text{m}$ band, a broad absorption after $10.2 \mu\text{m}$ (spectral shoulder) with a minor spike at $11.4 \mu\text{m}$. This emissivity spectral behavior of CaS near $7-14 \mu\text{m}$ remains constant irrespective of the temperature of the sample. The color of the CaS sample did not change throughout the experiment (Fig. 4.3b; ambient and heated) and this strongly supports the stability of CaS at Mercury surface conditions.

When increasing the sample surface temperature from 100 to 500°C , a) the spectral emissivity near $7.5 \mu\text{m}$ and $9.1 \mu\text{m}$ shows no linear correlation to temperature, with the order of decreasing emissivity for 100°C , 400°C , 200°C , 300°C , and 500°C ; b) the band

center near 7.5 μm remains constant until heating up to 400 $^{\circ}\text{C}$ but drops shortwards to ~ 7.4 μm at 500 $^{\circ}\text{C}$; c) the spectral emissivity is at maximum for the doublet near 8.8 μm where the spectral feature does not change in strength and position when heating from 100 $^{\circ}\text{C}$ to 400 $^{\circ}\text{C}$, whereas at 500 $^{\circ}\text{C}$, the emissivity near the 8.3 μm spectral shoulder slightly increases; d) the band center near 9.6 μm does not change until heating up to 300 $^{\circ}\text{C}$ but linearly shifts to longer wavelength from 300 $^{\circ}\text{C}$ to 500 $^{\circ}\text{C}$; e) the spectral shoulder near 10.2 μm and spectral spike near 11.4 μm slightly increase linearly with increasing temperature from 100 to 500 $^{\circ}\text{C}$. The general shape of the bands remains constant for the CaS emissivity spectra irrespective of the temperature (Fig. 4.3b).

The derived emissivity (1-R) from the reflectance measurements of fresh and heated CaS samples shows similar behavior to their emissivity spectra with decreased emissivity at all spectral channels.

- 3) Two sample sets of MgS (Fig. 4.3 c,d; MgS-1, MgS-2; Table 4.3 for sample properties) from two different vendors show slightly different emissivity behavior. However, they both have a characteristic emissivity minimum centered near 7.8 μm . Both MgS-(1,2) samples show physically effusive behavior on heating; however, the sample MgS-2 seems to be more stable than the MgS-1. MgS-1 started to gush out (see Fig. 4.1(bottom)) at $T > 200$ $^{\circ}\text{C}$ leaving us only with two emissivity measurements (Fig. 4.3c). The heated MgS-2 seems to have a physical crack on the surface layer because of this effusive activity (Fig. 4.3d). The most likely explanation for such activity could be that MgS starts to dissociate at high temperatures and therefore releases S to the atmosphere. This dissociation physically changes the surface morphology of the sulfide samples. This observation therefore suggests that thicker deposits of MgS on Mercury's surface might display thermally fractured floors. The search for such features in very high spatial resolution images of BepiColombo will open new doors in understanding the role of volatiles in surface mineralogy and morphology (see Fig. 4.6 in Helbert et al., 2013a)
 - a) MgS-1 (Fig. 4.3c): The derived emissivity spectrum (1-R) of fresh sulfide shows a broad band centered near 7.8 μm (with spectral shoulders at 7 and 8.8 μm) and a very weak absorption near 9.5 μm . On heating to $\geq 100^{\circ}\text{C}$, the radiance measured at 7.8 μm got stronger and narrower, and the weak 9.5 μm almost disappeared.
 - b) MgS-2 (Fig. 4.3d): In the derived emissivity spectrum of fresh MgS-2 (1- R fresh), the strength of the 7.8 μm and the 9.5 μm spectral absorption features are prominent with

broad and minor absorption feature near 13 μm . On heating to 100°C, the measured radiance (emissivity) spectra possess all the spectral absorption features except for the 7.8 μm band, which completely disappeared. However, an additional minor and very weak absorption is noticed at 8.9 μm . On further heating to 200°C and 300°C, the 7.8 and 8.9 μm bands merge together with the inflection near 8.9 μm . On further heating to 400°C and 500°C, the 7.8 μm absorption feature disappeared and left us with the minor absorption near 9 μm . However, the derived emissivity of heated sample (1-R heated) still preserves the 7.8 μm band with no 9 μm absorption. This clearly shows that the 7.8 μm and 9 μm features are completely temperature dependent.

- 4) Manganese sulfide (MnS, Fig. 4.3e) shows lower emissivity in the entire spectral range of 7-14 μm compared to the other sulfides studied. The derived emissivity (1-R fresh, Fig. 4.3e) shows a broad emissivity maximum centered near 8.8 μm (spectral shoulders at 8 and 9.7 μm) and a weaker absorption feature near 9.8 μm . On heating to 100°C, the spectral contrast of the bands gets weaker and the slope of the spectra is slightly increased (redder) shape. With further heating to 200°C, the slope of the spectra gets much redder with four minor absorption features near 7.8 μm , 9 μm , 9.8 μm , and 10.5 μm . Heating to 300°C and 400°C, the spectral behavior starts to look more similar to the derived fresh sulfide spectra (1- R fresh) but the spectral contrast of the kink feature near 9.2 μm gets sharper. Interestingly, the heating of the sample to 500°C subdues the contrast of all the characteristics spectral bands (emissivity maximum near 8.8 μm , and a weaker band near 7.1 μm). In general, spectrally the MnS can be identified by a emissivity maximum near 8.8 μm and a lower emissivity.
- 5) Iron sulfide (FeS, Fig. 4.3f) shows absolutely no characteristic spectral bands for both fresh (1- R fresh) and heated sulfides (100-500°C, 1 – R heated). However, the radiance measured at 200°C, shows a very weak and broad absorption feature (up to 9 %) centered near 8.8 μm (spectral shoulders at 7.8 μm and 10 μm). This feature further loses its spectral contrast linearly on heating to 300°C (8% absorption) and 400°C (6% absorption), and finally the spectra again become flat when measured at 500°C.
- 6) Chromium sulfides (CrS, Fig. 4.3g) show a very similar spectral behavior (nearly flat) of the radiance measured at all temperatures with a very weak emissivity maximum band (5% emissivity strength) centered around 9 μm (spectral shoulders at 7.8 μm and 10.4 μm).

7) Titanium sulfides (TiS_2 , Fig. 4.3h) show generally a very flat spectral behavior at all wavelengths. However, the radiance measured at 200°C shows a slightly stronger and a very broad spectral absorption from $7.4\text{-}11.2\ \mu\text{m}$ with the strongest absorption near $8.1\text{-}9\ \mu\text{m}$ (up to 12% strength). This feature linearly decreases with increasing surface temperatures and the spectra become completely flat at 500°C , similar to the spectra measured at 100°C . During heating, the traditional green color of the sulfides closer to walls of the sample cup turns to grey compared to the material in the center of the sample cup, indicating either a phase change or a change of the valence state (Fig. 4.3h). It is known that upon heating, TiS_2 release sulfur forming titanium(III) derivative (Ti_2S_3) which is a black powder (Mckelvy *et al.*, 2007). The radial difference is due to the differences in the temperature; as, for a given time, the samples closer to the sidewalls of the sample holder received higher temperature than the samples at the center of the cup. This implies that the traditional green color of the sulfides turn to grey on increased heating. The terms TiS (green) and TiS (grey) in Fig. 4.3h for heated sulfides refers to these thermally processed color morphologies. The derived emissivities ($1 - R$ heated green, $1 - R$ heated grey) at Fig. 4.3h show no distinctive spectral bands. However, the spectral slope of the grey exterior material (heated to $>500^\circ\text{C}$) of TiS shows a redder spectral slope upto $11.5\ \mu\text{m}$ and a bluer spectral slope at larger wavelengths.

4.5.2 REFLECTANCE

At PSL, the instrumentation provides spectral reflectance measurements over a wide spectral range that allows us to understand the spectral nature of the samples.

4.5.2.1 ULTRAVIOLET-VISIBLE (UV/VIS): 0.2 - 0.6 MICRONS

The UV/VIS spectral range corresponds to the MESSENGER'S MASCS UV/VIS spectrometer. The spectral behavior of the studied fresh sulfides and T-processed sulfides measured at four phase angles 26° , 40° , 60° , and 80° for this spectral range are plotted in Fig. 4.4a and Fig. 4.4b, respectively. The instrument specifications of the measurements are tabulated in Table 4.4. The measured spectra of both fresh and heated sulfides in Fig. 4.4 clearly show that the spectral characteristics of the respective sulfides do not change strongly with respect to phase angle but do change significantly because of thermal weathering.

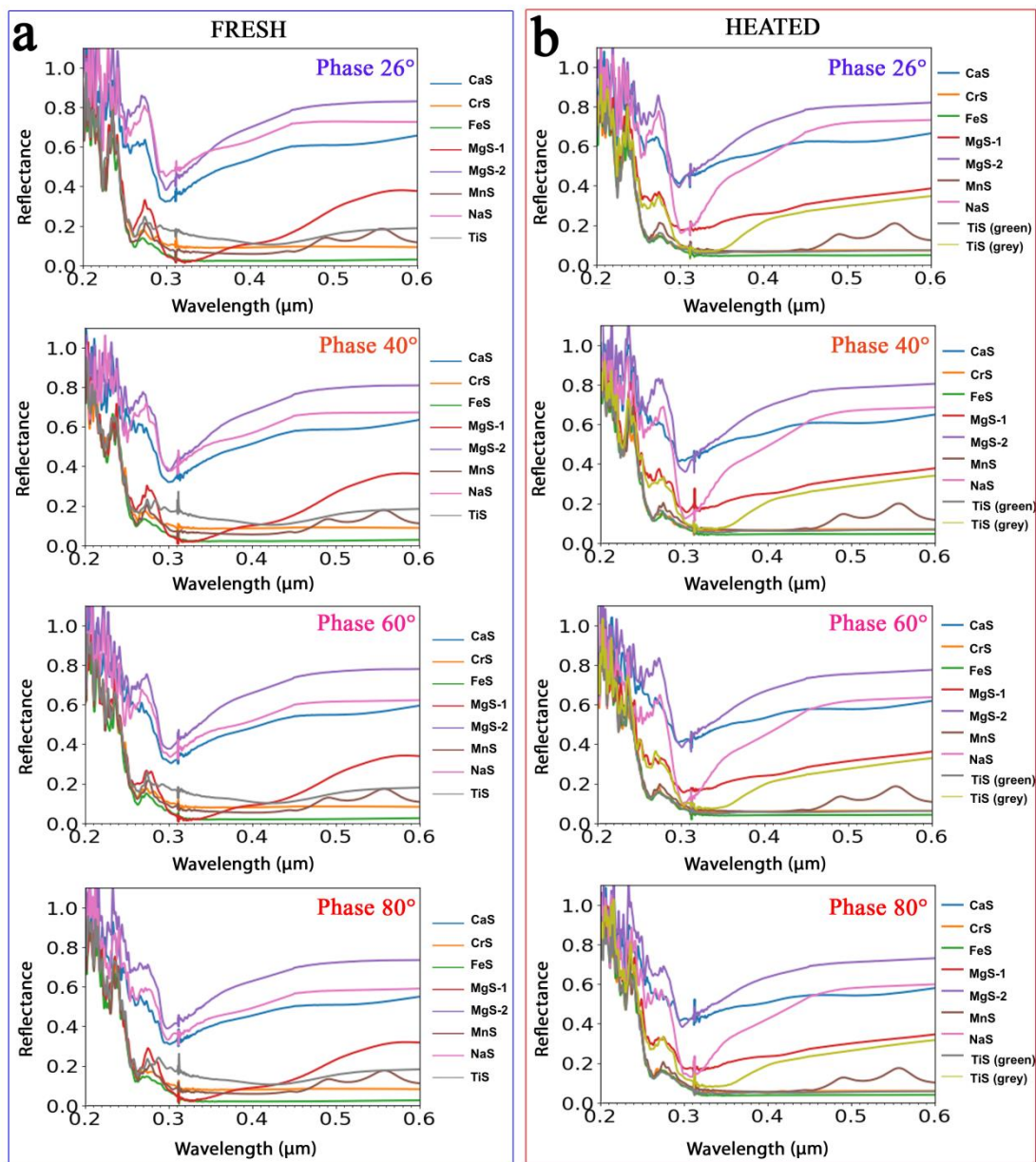


Figure 4.4. Measured reflectance at four phase angles 26°, 40°, 60°, and 80° at UVVIS spectra range (0.2 – 0.6 μm) of (a) fresh and (b) T-processed sulfides

4.5.2.1.1 Fresh sulfides

Fig. 4.4a shows that UV/VIS spectra of fresh sulfides show no significant change in the spectral band centers with respect to phase angle. However, the band strengths near 0.3 μm are slightly reduced with increasing phase angles. The UV/VIS spectral parameters of the studied sulfides are detailed below.

a) CaS, NaS, and MgS-2 show similar spectral behavior with three characteristic spectral features; two minor but sharper absorptions near 0.22 and 0.25 μm and one stronger/major absorption feature centered at 0.3 μm with spectral shoulders at 0.28 and 0.35 μm .

b) CrS, MnS, FeS, and TiS show no significant absorption features. Between 0.3-0.6 μm , the spectra are nearly flat and dark and they have a steep bluer slope in the 0.2-0.3 μm spectral region. However, two minor spectral absorption features can be identified along with higher reflectance at 0.22 and 0.26 μm . Unlike CrS, FeS, and TiS, MnS displays two additional minor bands near 0.52 μm (spectral shoulders at 0.49 and 0.56 μm) and 0.6 μm .

c) MgS-1 displays a broad 0.3 μm band centered around \sim 0.32 μm with two minor bands near 0.22 and 0.26 μm , respectively, and their spectral characteristic is evidently different from that of MgS-2. This further confirms the differences in the MgS used in the study.

4.5.2.1.2 T-processed sulfides

Similar to fresh sulfides, band strength of the \sim 0.3 μm band decreases with increasing phase angles (Fig. 4.4b). The CaS spectrum (Fig. 4.4b; Phase 80°) becomes nearly flat beyond 0.3 μm due to the increase in phase angle. However, the other bands are nearly unaffected irrespective of the phase angle of the observation.

Among all the heated (T-processed) sulfides studied, NaS displays sharper and stronger UV spectral features (0.25 and 0.3 μm) compared to its fresh spectra counterparts at all phase angles. Compared to the fresh sulfide counterparts (Fig. 4.4a), the heated CaS and MgS-2 (Fig. 4.4b) retain their band center positions but have slightly subdued spectral contrasts. Therefore, heated NaS, CaS, MgS-2 display band centers near 0.22, 0.25, 0.3 μm for their absorption features.

CrS, MnS, FeS, and TiS (green) show literally no spectral feature and are completely dark and flat beyond 0.3 μm . Except for FeS (hexagonal), CrS (hexagonal), TiS (Octahedral) the rest of the sulfides have cubic structure. The crystal structure of all these sulfides are now added to the Table 4.3 of supplementary material. The respective spectra retain their minor bands near 0.22 and 0.26 μm . However, heated TiS (grey) displays a broad 0.3 μm feature

centered near 0.32 μm . Similar to fresh spectra counterparts, heated MnS retains its additional bands near 0.52 and 0.6 μm for all phase angle measurements.

Unlike fresh MgS-1, heated MgS-1 shows no absorption near 0.3 μm and it displays slightly redder spectra beyond 0.3 μm along with additional bands near 0.22 and 0.26 μm . Also, the spectrum of heated MgS-1 is different from that of MgS-2, as is its fresh spectra counterpart.

4.5.2.2 VISIBLE-INFRARED (VIS-IR): 0.3 – 1 MICRONS

The measured reflectance in the VIS-IR (0.3–1 μm) spectral range for all fresh and heated sulfides at all phase angles is plotted in Fig. 4.5a and Fig. 4.5b, respectively. Though the spectral behavior of these sulfides at 0.3-0.6 μm is discussed in the previous subsection, the 0.3-1 μm range is chosen to support the MESSENGER's MASCS VIS spectrometer observations. From the spectra plotted in Fig. 4.5, it is important to note that both fresh and heated samples of CaS, NaS, and MgS-2 have high albedo that could be detected from the visible camera images of sulfide deposits. TiS, FeS, and CrS are not only much darker in albedo, they also do not have any characteristic spectral features in this spectral range. Thus, they are harder to detect on the Mercury's surface. The spectral behavior of these sulfides is discussed below.

Among the fresh sulfides (Fig. 4.5a), only MnS displays two distinctive spectral absorption bands centered near 0.52 and 0.6 μm with a redder (increased spectral gradient) slope. CrS, FeS, and TiS show no spectral feature and display a very flat spectrum across the entire VIS-IR spectral range. CaS, NaS, and MgS-2 possess redder slopes from 0.3 to 0.45 μm but display flat spectra at longer wavelengths. MgS-1 spectrum shows a redder slope throughout with two minor broad spectral bands near 0.43 and 0.63 μm , and a sharp but very weak spectral kink near 0.97 μm .

For the heated sulfides (Fig. 4.5b), the spectral band strength of MnS increases mainly for the 0.6 μm absorption feature. The minor spectral features in fresh MgS-1 are completely lost in reflectance measurements of their heated counterparts and the spectra are redder. Similar to fresh CrS, FeS, and TiS (green), the spectra of the heated counterparts are completely flat, showing no spectral features. However, the TiS (grey) spectra display a strong absorption near 0.33 μm . The spectral gradient between 0.3-0.45 μm becomes such redder

for heated NaS, compared to its fresh counterpart. CaS and MgS-2 display similar spectral behavior to their fresh spectra counterparts.

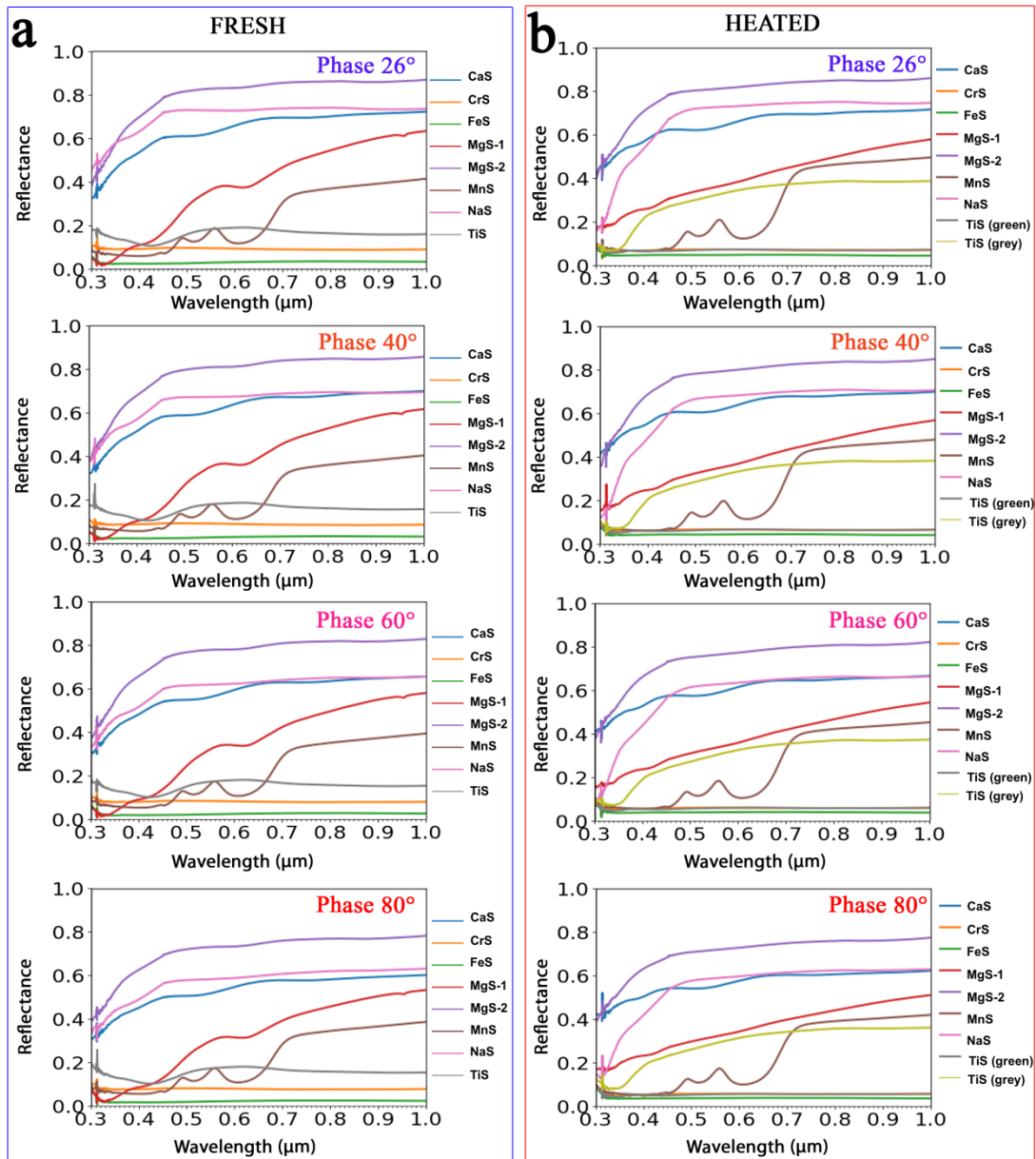


Figure 4.5. Measured reflectance at four phase angles 26°, 40°, 60°, and 80° at VIS-IR spectra range (0.3 – 1 μm) of (a) fresh and (b) T-processed sulfides

Though most of the sulfides do not have distinctive spectral bands in the VIS region, the high albedo of the CaS, NaS, MgS-2 will greatly increase the likelihood of detection of these sulfide deposits among the average darker albedo of the Mercury's surface.

Additionally, Fig. 4.5 also clearly shows that there is no significant influence of the phase angle on the measurements for both fresh and heated sulfides in the VIS-IR spectral range.

4.5.2.3 NEAR INFRARED (NIR): 1-6 MICRONS

The measured reflectance in the NIR spectral range of 1-6 μm for both fresh and heated sulfides is shown in Fig. 4.6. For this spectral range, the strength of the absorption bands for each sulfide (fresh and heated) is noticeably subdued with increasing phase angle, however, the band centers do not show any effect.

Fresh MgS-1 and MgS-2 show four characteristic spectral absorptions; the strongest and broad absorption around 3 μm (with a sudden drop in reflection around 2.6 μm) and three other significant sharp and narrow bands near 1.1, 2, and 2.4 μm including a minor inflection near 2.3 μm . However, the strengths of each of these bands is subdued for MgS-2 as compared to MgS-1. For the heated MgS samples, the band centers of these absorptions do not change, however, the spectra are smoothed and the 3 μm absorption is considerably intensified.

Fresh CaS samples (Fig. 4.6a) show a characteristic broad spectral band at $\sim 3 \mu\text{m}$ and two minor inflections near 3.5 and 4.6 μm . On heating (Fig. 4.6b), the 3 μm band is highly subdued and thereby strengthening the inflections at 3.5 and 4.6 μm .

Fresh MnS samples (Fig. 4.6a) have a strong, narrow, characteristic band centered at 2.8 μm and a very weak and minor band near 4.7 μm . However, for the heated MnS samples (Fig. 4.6b) the spectrum is nearly flat with a small hint of 2.8 μm spectral absorption.

Fresh CrS (Fig. 4.6a) shows a bluer spectral slope between 1 and 2 μm and a nearly flat spectrum at longer wavelengths with a weak band around $\sim 3 \mu\text{m}$. On heating (Fig. 4.6b), CrS shows no spectral absorption, however the general trend of the spectra is preserved.

Fresh TiS and FeS samples (Fig. 4.6a) have no spectral absorptions in this spectral range and relatively dark albedo. On heating (Fig. 4.6b), FeS and TiS (green) are again spectrally flat; however, TiS (grey) shows a spectrally broad and relatively weak 3 μm absorption band.

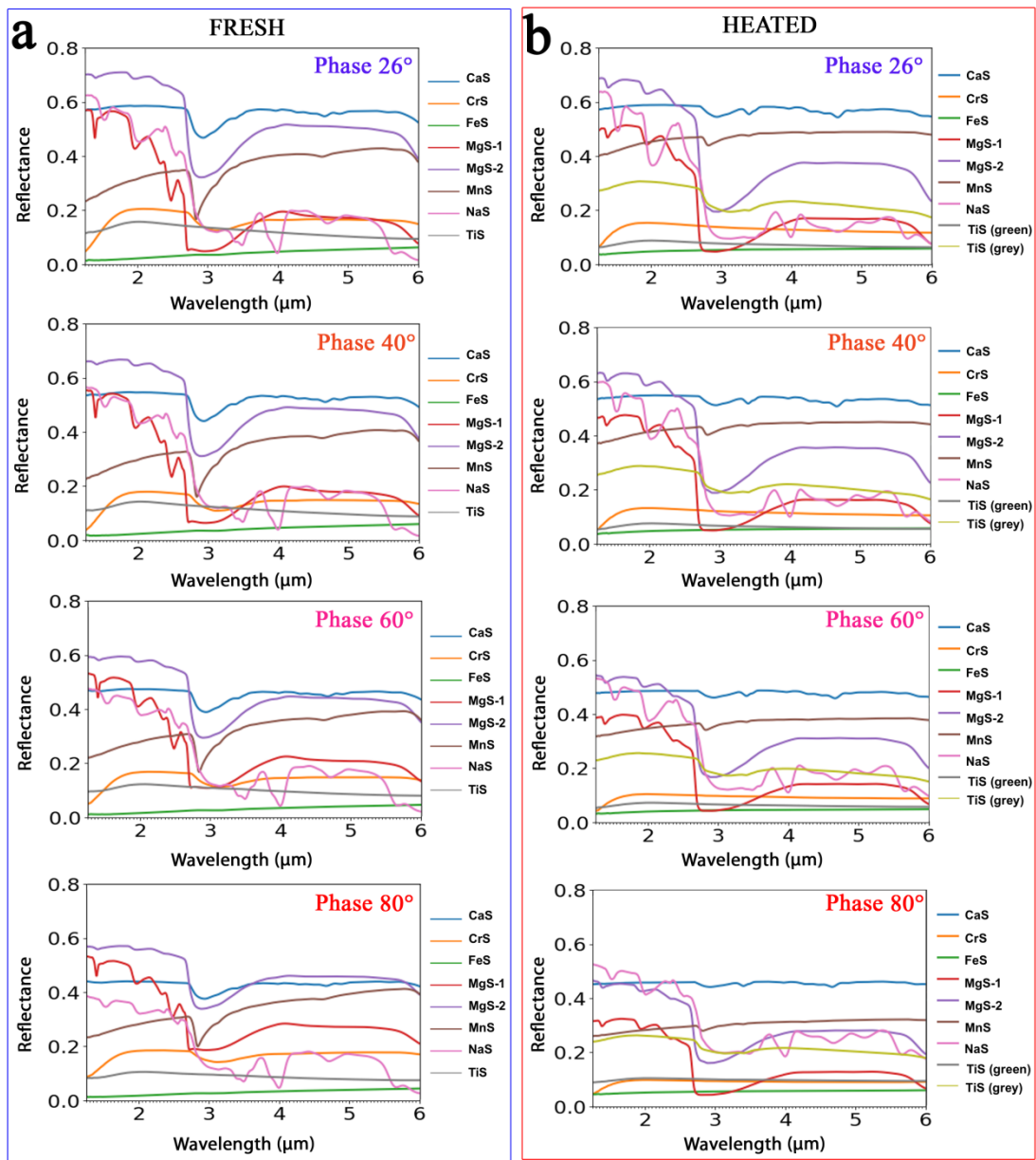


Figure 4.6. Measured reflectance at four phase angles 26°, 40°, 60°, and 80° at NIR spectra range (1 – 6 μm) of (a) fresh and (b) T-processed sulfides

Fresh NaS (Fig. 4.6a) possesses many diagnostic spectral bands in this spectral range; the main noticeable spectral bands include a) a minor 1.3 μm band, b) a relatively strong absorption around 2 μm , c) a weak inflection near 2.5 μm , d) a sudden drop in reflectance after 2.6 μm , e) an absorption at 3.4 μm , f) a strong and narrow 4 μm feature, g) a weak 4.6 μm feature, and h) an inflection near 5.6 μm . The reflectance measured for the heated NaS (Fig. 4.6b) shows a similar behavior of the spectral bands except (a,b) gets stronger in absorption strength, (e, f) combines to form a broad spectral band around 3 μm (2.8-3.6 μm wide), (f) gets weaker, and (g) gets relatively stronger and wider.

In general it is safe to say that sulfides measured across the NIR spectral range show an evident 2.8/3 μm absorption band except for FeS and maybe TiS. On increase of phase angle, all of these bands show a noticeable decrease in absorption strength for both fresh and heated sulfides in NIR spectral range.

4.5.2.4 MID INFRARED/THERMAL INFRARED (MIR/TIR): 7-14 MICRONS

Fresh sulfides: Among all the sulfides measured (Fig. 4.7a), only three samples show significant characteristic spectral absorption in this wavelength region; a) CaS has two strong absorption bands around 8.5 and 10.3 μm , b) MnS has one broad and strong absorption near 8.8 μm , and c) MgS-2 shows a bluer spectral slope beginning at 7.9 μm (a spectral bump) with minor inflections near 8.9, 10, and 11.6 μm . MgS-1 has similar inflection pattern than MgS-2, however it has a very flat spectral slope. CrS has flat spectra with very wide spectral absorption around 9 μm . NaS shows a ripple-like flat spectrum with minor absorption features at 7.8, 8.8, 10, 11.5, and 14 μm . TiS has no characteristic spectral absorption features with a redder spectral gradient. FeS has a flat spectrum with no spectral absorptions whatsoever.

Heated sulfides: In heated sulfides (Fig. 4.7b), CaS preserves its strong absorption features (8.5 and 10.3 μm). The MnS characteristic band at 8.8 μm is significantly subdued with a slight shift in its band center to shorter wavelength of ~ 8.7 μm and a bluer spectral slope. MgS-1 and MgS-2 preserve their spectral bump near 7.9 μm with flat and blue spectral gradients respectively. The ripple-like spectral nature of fresh NaS (Fig. 4.7a) is still preserved after heating (Fig. 4.7b). Heated samples of FeS, CrS, and TiS show a very flat spectral gradient throughout the spectral range.

Fig. 4.7 also shows that the spectral contrast decreases with increasing phase angles of the measurements in this spectral range for both fresh and heated sulfides.

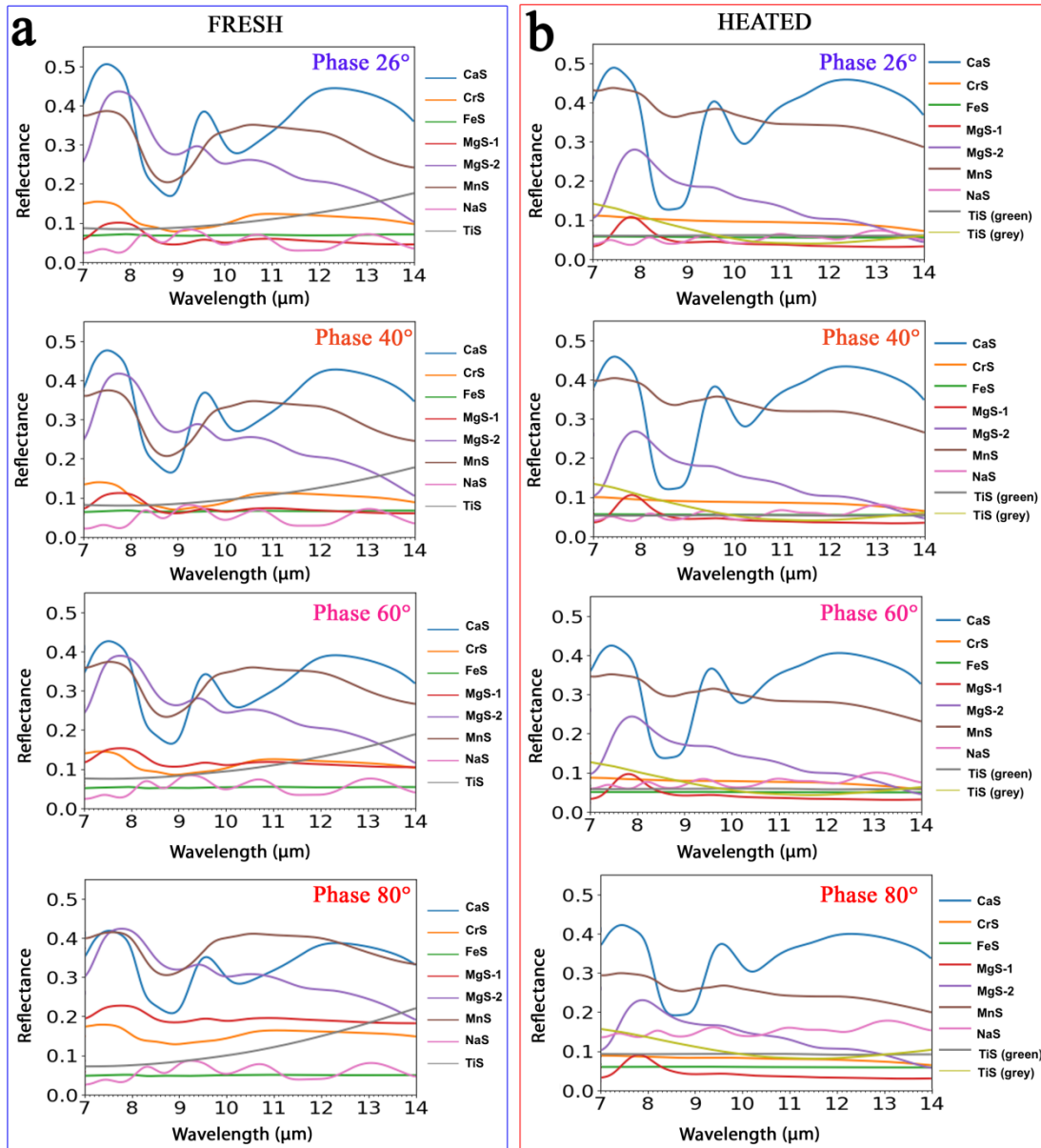


Figure 4.7. Measured reflectance at four phase angles 26°, 40°, 60°, and 80° at MIR/TIR spectral range (7 – 14 μm) of (a) fresh and (b) T-processed sulfides

4.5.2.5 FAR INFRARED (FIR): 15-100 MICRONS

The measured reflectance for the FIR spectral range (15-100 μm) for both fresh and heated samples is plotted in Fig. 4.8a and Fig. 4.8b, respectively.

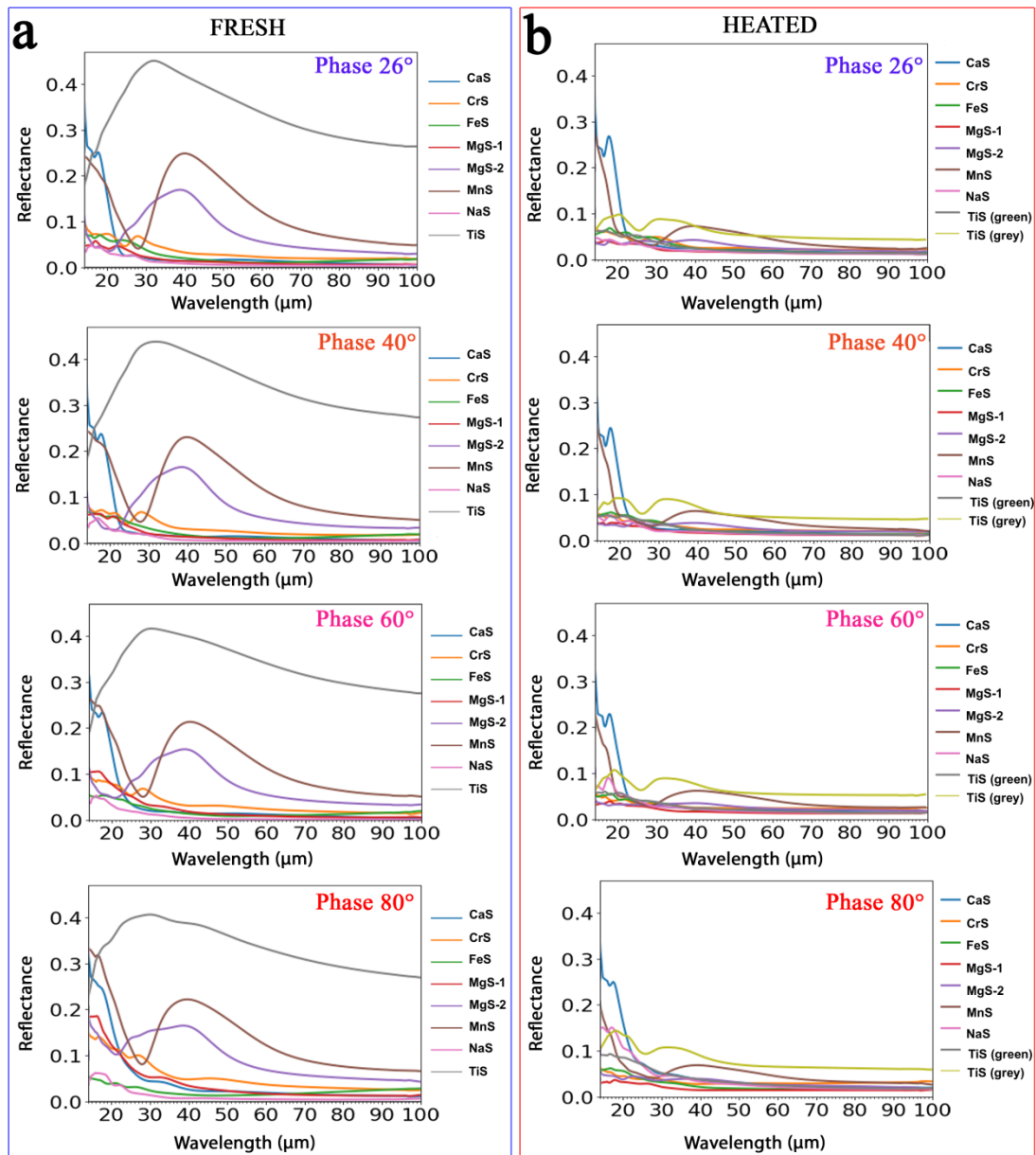


Figure 4.8. Measured reflectance at four phase angles 26°, 40°, 60°, and 80° at FIR spectra range (15 – 100 μm) of (a) fresh and (b) T-processed sulfides

Fresh sulfides (Fig. 4.8a): TiS has a strong spectral shoulder (bump/reflectance maximum) at 30 μm . MnS has a strong, narrow spectral absorption feature centered at ~ 28 μm (with spectral shoulders at 15 and 40 μm). CaS spectrum is characterized by sudden drops in reflectance at 18 μm (bump) and a flat behavior beyond 23 μm . MgS-2 has a spectral absorption at 18 μm with the reflectance maximum (bump) near 40 μm , however, MgS-1 shows no spectral feature and has a flat and dark spectral gradient. CrS has flat and dark spectra with a minor bump near 28 μm . TiS, CaS, FeS, and NaS have no significant spectral signatures and a flat spectral gradient.

Heated sulfides (Fig. 4.8b): MnS show a reflectance maximum around 15 μm and the spectra get flat at wavelengths longer than 23 μm with a minor bump near 40 μm . CaS spectra show a steep and sudden inflection beyond 18 μm similar to their fresh spectra counterparts. TiS (grey) spectra show a minor weak band near ~ 25 μm . The remaining heated sulfide samples (CrS, FeS, MgS-1, MgS-2, NaS, TiS (green)) do not show any distinctive spectral absorption features and they have flat spectral slopes. However, NaS (at Phase 80°, Fig. 4.8b) shows bluer spectral gradient for the spectral range of 15-30 μm .

4.6 DISCUSSIONS

Studying the spectral behavior of possible Mercury analogues at a range of Mercury dayside surface temperatures will help us to create a standard spectral library useful for BepiColombo and MESSENGER data analysis (Maturilli *et al.*, 2017a).

4.6.1 BEPICOLOMBO MERTIS

Our emissivity measurements (Fig. 4.3) show that slowly heating the sulfides to Mercury's surface temperature (500°C) changes the spectral signature (and potentially the crystal structure) of the sulfides. The sulfide samples and their characteristic spectral bands are tabulated in Table 4.1. Sulfide mineralogy will be easily detected in the upcoming MERTIS dataset (7-14 μm) on the basis of distinctive absorption centers and spectral shapes. Among the sulfides studied, CaS and MgS preserved their strong absorption features even after heating to high temperatures. CaS can be identified by their strong absorptions near 7.4 and 9.6 μm with an emissivity maximum near 8.8 μm . MgS has a distinctive 7.8 μm absorption.

Though this feature disappears at 400° and 500°C, it reappears when the surface is cooled below ~350°C and therefore increases the chance of detection at the locations where the surface temperature is less than ~350°C. Irrespective of its distinctive spectral feature, MgS tends to break down when heated to higher temperature, which may suggest the loss of spectral signature of these deposits over the age of their formation. MnS and CrS have an emissivity maximum near 9µm; MnS has a slightly narrower feature centered near 8.8µm compared to the wide spectral feature of CrS. TiS and FeS are difficult to detect because they have no distinctive and strong spectral features in this spectral region. Advantageously and unlike the Moon, Mercury's surface is deficient in Fe and Ti abundance, thus, making it unlikely to encounter these species on Mercury surface in relevant abundances. This study reveals that Mercury can be best mapped for its sulfides in the TIR region. Because our sample cups are placed flat while taking the measurements, this configuration closely matches to the nadir observation of MERTIS. Thus, MERTIS is capable of identifying and mapping sulfide deposits (Helbert et al., 2013a) within the hollows and also the S-related pyroclastic deposit distribution on the surface, irrespective of the local time of observation. MERTIS will be a powerful instrument not only to identify the silicate mineralogy but also to identify volatile-rich minerals across the surface. Thus, MERTIS will open a new door to identify spectrally heterogeneous surface mineralogy of Mercury.

4.6.2 MESSENGER MASCS

The spectral measurements of sulfides at high phase angles (80°) are also relevant for their detection in MESSENGER MDIS/MASCS UV/VIS data (Fig. ; Phase 80° and Table 4.1). In the UV/VIS spectral range (0.3-0.6µm), both fresh and heated sulfides of CaS, NaS, and MgS show stronger absorption near 0.3µm. MnS shows distinctive spectral bands at 0.52µm. All the fresh and heated sulfides show both minor and sharp bands near 0.22 and 0.26µm. These spectral features do not change phase angles and temperatures. Thermal weathering of sulfides does not influence their spectral nature in the ultraviolet. MASCS UV/VIS spectrometer datasets should be revisited to look for these distinctive spectral features of sulfides.

Table 4.1. Characteristic spectral absorption bands for detection of sulfides by MERTIS of BepiColombo mission

Emissivity	100 °C (μm)	200 °C (μm)	300 °C (μm)	400 °C (μm)	500 °C (μm)
NaS	7.5m, 8.4w, 9.2w, 9.5w, 11w, 11.6w, 13wW	7.5m, 8.4, 9.3d, 11.6, 13, 13.9m	7.1m, 8.8m, 9.2m, 12.8- 13.5W	7.1m, 8.8m, 9.2m, 12.8- 13.5W	8wm, 10wm, 13wm
CaS	7.5, 8.8d, 9.6, 10.2- 14W, 11.4b	7.5, 8.8d, 9.6, 10.2-14W, 11.4b	7.5, 8.8d, 9.6, 10.2-14W, 11.4b	7.5, 8.8d, 9.6, 10.2-14W, 11.4b	7.4, 8.8d, 9.6, 10.2-14W, 11.4b
MgS-1	7.8	7.8	No data	No data	No data
MgS-2	7.8, 8.9wm, 13Wwm	7.8-9W, 13Wm	7.8-9W, 13Wm	9m	9m
MnS	7-8W, 9.8m	7.8m, 9m, 9.8m, 10.5m	7-8W, 9.2b, 9.8m	7-8W, 9.2b, 9.8m	8.8Wb
FeS	-	8.8wmW	>8.8wmW	>8.8wmW	-
CrS	9wmWb	9wmWb	9wmWb	9wmWb	9wmWb
TiS	-	8.1-9W	<<8.1-9W	<<8.1-9W	-

w-weak, W-wide, m-minor, d-doublet, b-bump

In the spectral range from 0.3 to 1.45 μm , both fresh and thermally processed MnS show strong spectral absorption features near 0.52 and 0.6 μm (Fig. 4.5 and Table 4.2). Detection of these features in MDIS/MASCS VIRS datasets will therefore prove their presence on Mercury. Most of the sulfides also have a steeper slope between 0.3 and 0.4 μm and a minor absorption near 1.1 μm that could also be used as a tracer in VIRS datasets for searching for sulfides on Mercury.

4.6.3 BEPICOLOMBO SIMBIO-SYS/VIHI

Because VIHI has a similar spectral range to MESSENGER MASCS VIRS though extended to ~ 2 μm (i.e., ~ 0.4 -2 μm) and nadir-pointed (corresponding to Phase 26^o) (Fig. 4, 5; Phase 26^o and Table 4.2). The minor absorptions near 1.1 and 1.3 μm feature can be traced for MgS and NaS, while the 2 μm features can be studied both for MgS and NaS sulfides. CaS shows a weak and minor absorption feature near 0.55 μm . MnS shows strong absorption features near 0.52 and 0.6 μm . The very flat spectral nature and dark albedo of TiS, FeS, and CrS make them difficult to detect in this spectral range.

4.6.4 SPECTRAL BEHAVIOR OF SULFIDES WITH RESPECT TO PHASE ANGLE AND TEMPERATURE

It is important to understand the spectral behavior of these sulfides as a function of phase angle and temperature effects. Fig. 4.9 shows that the sulfide spectra show few phase angle effects in the UV spectral range. Spectral contrast is subdued with increasing phase angles in the FIR spectral range. Data from the UV/VIS (0.3-0.6 μm) show no spectral variations with the change of phase angle. However, the absorption strength and albedo of the spectra are slightly diminished with increasing phase angle at the spectral range $>1 \mu\text{m}$. Also, the reflectance spectra of heated sulfides in the FIR spectral range (15-100 μm) show a complete loss of features compared to their fresh counterparts. To understand the emissivity spectra with respect to temperature, it is important to revisit Fig. 4.3, which clearly demonstrates dynamic changes in the spectral behavior of sulfides depending on surface temperatures (e.g., NaS). Thus, the spectral behavior of sulfides cannot be generalized for temperature effects as each sulfide behaves differently with respect to temperature. To understand the behavior of these sulfides in the crystal mode, a further extended study of the detailed behavior of sulfide minerals with heating should be performed. Future work will concentrate on prolonged heating of sulfides at Mercury environmental conditions and step-by-step changes in spectral behavior along with their crystal structures.

Table 4.2. Detection of sulfides in the spectral range (1-100 μm) for reflectance measurements

Reflectance	Sulfides	UVVIS (0.3–0.6 μm)	VISIR (0.3–1 μm)	NIR (1–6 μm)	MIR (7–14 μm)	FIR (15–100 μm)	Albedo
CaS	Fresh	0.3, 0.22m, 0.25m	0.55wm	3	8.5, 10.3	18b	high
	Heated	0.3, 0.22m, 0.25m	0.55wm	-	8.5, 10.3	18b	high
CrS	Fresh	0.22m, 0.26m	-	3w	9w,m	28mb	low
	Heated	0.22m, 0.26m	-	-	-	-	low
FeS	Fresh	0.22m, 0.26m	-	-	-	-	low
	Heated	0.22m, 0.26m	-	-	-	-	low
MgS-1	Fresh	0.32Bm, 0.22m, 0.26m	-	3, 1.1m, 2m, 2.4m	7.9b, 8.9i, 10i, 11.6i	-	medium
	Heated	0.22m, 0.26m	-	3, 1.1wm, 2wm, 2.4wm	7.9b	-	medium
MgS-2	Fresh	0.3, 0.22m, 0.25m	-	3, 1.1wm, 2wm, 2.4wm	7.9b, 8.9i, 10i, 11.6i	18, 40b	medium
	Heated	0.3, 0.22m, 0.25m	-	3, 1.1wm, 2wm, 2.4wm	7.9b	-	medium
MnS	Fresh	0.22m, 0.26m, 0.52m, 0.6m	0.52, 0.6	2.8	8.8	28	medium
	Heated	0.22m, 0.26m	0.52, 0.6	2.8wm	8.7m	40b	medium
NaS	Fresh	0.3, 0.22m, 0.25m	-	1.3, 2, 2.5i, 3.4, 4, 4.6w, 5.6i	Ripple (7.8, 8.8, 10, 11.5, 14)m	-	high
	Heated	0.3, 0.22m, 0.25m	-	1.3, 2, 2.5i, 3W, 4, 4.6w, 5.6i	Ripple (7.8, 8.8, 10, 11.5, 14)m	-	high
TiS	Fresh	0.22m, 0.26m	-	-	-	30b	low
	Heated (green)	0.22m, 0.26m	-	-	-	-	low
	Heated (grey)	0.32Bm	0.33	3m	-	25m	low
Effect of phase angle		no	no	yes	yes	yes	

b-bump, B-broad, m-minor, w-weak, W-wide, i-inflection, s-sharp

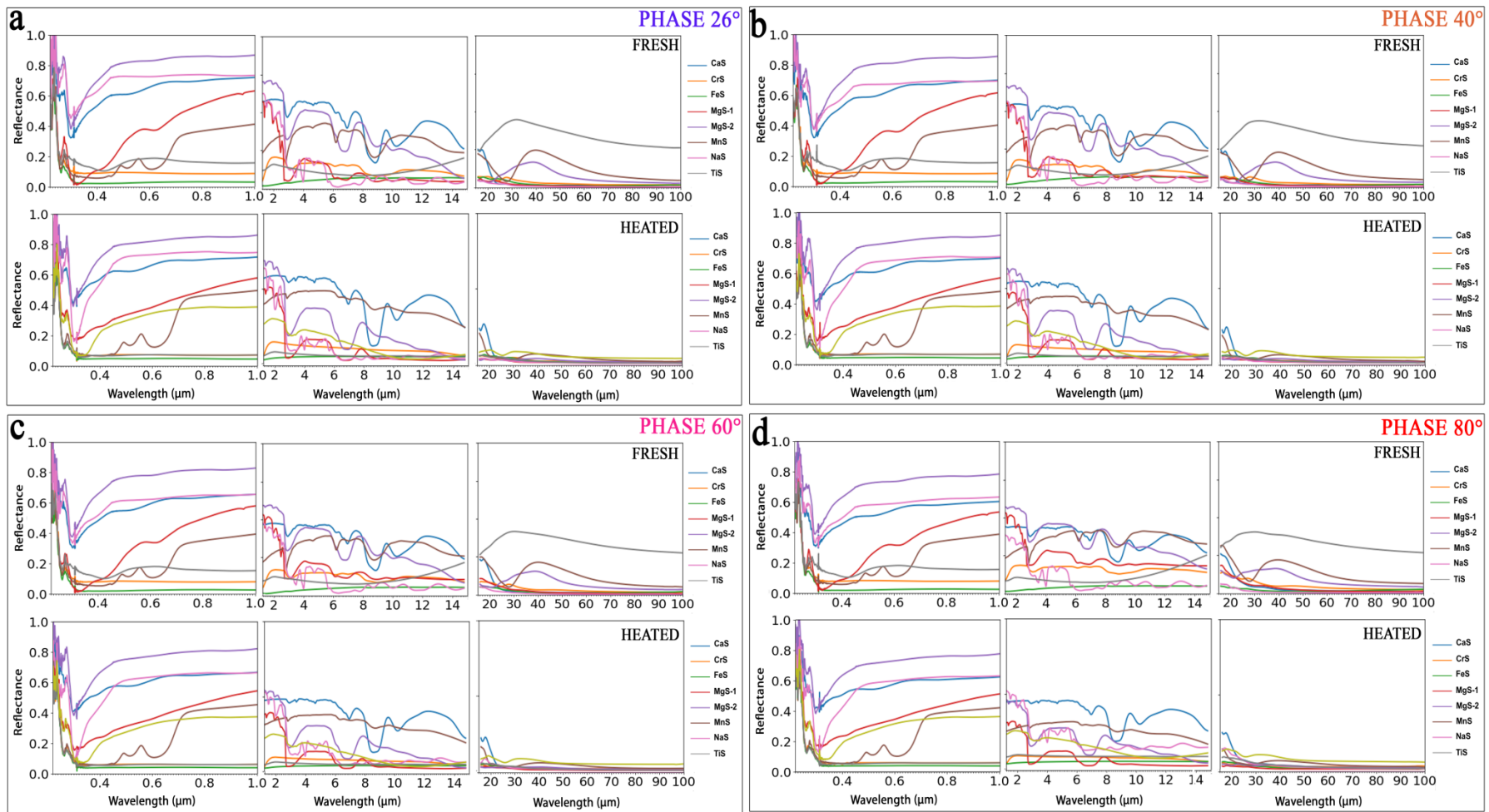


Figure 4.9. Measured reflectance at four phase angles a) 26°, b) 40°, c) 60°, and d) 80° at complete spectra range studied (0.2 – 100 μm) for both fresh and heated sulfides respectively.

4.7 CONCLUSIONS

In this study, the emissivity behavior of sulfides (7-14 μm) with respect to changing temperature under Mercury surface conditions has been carefully addressed. The reflectance spectral behavior of fresh and thermally processed sulfides after emissivity measurements across a wide spectral range (0.2-100 μm) has been studied. Characteristic spectral bands for identification of these sulfides has been cataloged to support analyze of existing and future datasets. Sulfide spectra show less variation with phase angle at shorter wavelength. Therefore, the available MESSENGER MDIS and MASCS UVVIS datasets should be further explored to discover sulfide deposits on Mercury's surface by searching for their distinctive 0.3 μm absorption feature. However, the nature/composition of these sulfides will only be unraveled by MERTIS (TIR spectral range) as each of the sulfides has a characteristic TIR emission spectrum. The ongoing work will focus on 1) Search for these sulfides in the existing orbital datasets, 2) Derivation of spectral parameters that effectively identify them in the future MERTIS datasets, and 3) Machine learning techniques to unmix sulfide spectra from silicates in Mercury surface conditions.

4.8 ACKNOWLEDGEMENT

The authors thank DLR/DAAD Doctorate Fellowship to Indhu Varatharajan for funding her PhD work at PSL-DLR. A portion of this research was supported by the European Union's Horizon 2020 research and innovation program. Europlanet 2020 RI has received funding from the European Union's Horizon 2020 research and innovation programme under grant agreement No 654208.

4.9 SUPPORTING INFORMATION

4.9.1 PLANETARY SPECTROSCOPY LABORATORY (PSL) IN DETAIL

Currently at PSL, we operate two identical FTIR (Fourier transform infrared) spectrometers (Bruker Vertex 80V); one spectrometer (Bruker A) is equipped with aluminum mirrors optimized for spectral measurements in the ultraviolet (UV), visible and NIR (near

infrared) wavelength region (say, 0.2 – 25 μm) (Fig. 4.1 in the main article), and the second one (Bruker B) is equipped with gold-coated mirrors optimized for measurements in near- to far-IR spectral range (1 - 100 μm) (Fig. 4.1 in the main article). Both the spectrometers (Bruker A and Bruker B) use a Bruker A513 variable-angle reflection accessory (two mirrors enabling viewing cone with aperture of 17°) allowing bi-conical reflectance measurements under vacuum conditions for phase angles between 26° and 170° (Maturilli *et al.*, 2014). The second spectrometer (Bruker B, Fig. 4.1 in the main article) is also attached to an external chamber for direct emissivity measurements by heating the samples to required temperature (~320 K – 1000 K) using a high efficiency induction heating system. This chamber is separated from the Bruker B by a shutter so that both the spectrometer and chamber can be operated independently at vacuum conditions. The external chamber can also work at ambient pressure conditions by mounting a vacuum-tight optical window between the chamber and Bruker B. The emissivity chamber is equipped with temperature sensors (thermopiles) for tracking the temperature of the sample and the surrounding environment during the measurements along with a webcam for monitoring the experiment. Thermal infrared spectral studies of a variety of mineral analogues to Mercury and other planetary bodies have been conducted in varying temperature conditions at PSL using this facility (Maturilli *et al.*, 2017a).

4.9.2 STEP-BY-STEP PROCEDURE OF EMISSIVITY MEASUREMENTS OF SULFIDES AT PSL.

Each sulfide sample is poured in a stainless steel cup to a 3-mm-thick uniform layer. The cup is then placed on a carousel above the induction pancake coil inside the external chamber. Each cup is equipped with three thermopile temperature sensors; two of them measure the temperature of the emitting surface of the sample and the third one measures the temperature of the sample cup itself on its side. Therefore, we trace both the surface temperature of the sample (thermopiles on emitting surface), and the thermal environment of the sample (thermopile on the steel cup). The experiment setup is shown in Fig. 4.2 in the main article. Then, the chamber is evacuated slowly until it reaches the final vacuum (pressure of ~ 0.7 mbar). The system is maintained at vacuum for at least 1 hour to get rid of the air molecules trapped in the sample. In the meantime, in the evacuated instrument the MCT detector is cooled using liquid nitrogen.

Once the instrument and chamber is stabilized in vacuum conditions, the sample is slowly heated to ~100 °C by manually controlling the current supply to the induction system.

Once the sample surface temperature stabilizes at 100 °C the measurement procedure is initiated. The shutter between chamber and spectrometer is opened and radiance from the heated sulfide collected by a gold (Au) coated parabolic at 90° off-axis is reflected into the spectrometer and recorded by the MCT detector. For each measurement a set of 100 scans is obtained to increase the signal to noise ratio while keep the sample temperature stabilized at 100 °C.

In the same way, each sulfide sample is heated from 100 to 500 °C (step 100 °C) in vacuum by slowly increasing the current to the induction coil. It takes about 1 h to heat the sample to every increased step of 100 °C. Over the entire heating period, the sulfides are carefully monitored with the webcam installed in the chamber. Therefore, emissivity measurements are taken at temperatures of 100 °C, 200 °C, 300 °C, 400 °C, and 500 °C for better simulating different thermal insulating conditions on Mercury depending on their time of day and/or latitude. After the last emissivity measurement at surface temperature of 500 °C the samples are now thermally processed for the Mercury's surface conditions.

The thermally processed sulfide sample is then cooled overnight down to room temperature in vacuum conditions.

After emissivity measurements of each sulfide sample, the chamber is vented slowly by manual control to avoid disturbing of samples due to sudden gush of air, and the whole chamber is cleaned thoroughly to remove all potentially outgassed materials that might stick to the chamber walls, temperature sensors, the parabolic mirror, and rotating carousel while heating the samples (see Fig. 4.2 of MgS in the main article).

The entire procedure is repeated for every sulfide sample studied.

All the measured emissivity spectra of sulfides are then calibrated against a blackbody reference (in this case, blast furnace slag) for each measured temperature and geometric configuration (Maturilli et al., 2013). The calibrated sample emissivity of the sulfides is shown in Fig. 4.3 in the main article.

4.9.3 STEP-BY-STEP PROCEDURE OF REFLECTANCE MEASUREMENTS OF SULFIDES.

The standard black Teflon sample cups are prepared for all sulfide samples (both fresh and T-processed) for the reflectance measurements.

The instrument is equipped with appropriate beamsplitters and detectors for the corresponding reflectance measurements; e.g., CaF₂ beamsplitter and GaP detector for UV measurements (see, Table 4.2 for all spectral range). For MIR measurements alone, we need to cool the detector using liquid nitrogen.

The reference sample for corresponding spectral range is then loaded to the sample holder for calibration of the reflectance measurements of the sulfides; e.g., White PTFE (plastic) for UV spectral range (details in Table 4.2 for all spectral range). Once the reference is loaded, the instrument is evacuated.

Before taking the reflectance of the reference sample, the software is instructed to run a macro that contains the list of phase angles ($i/e = 13^\circ/13^\circ, 20^\circ/20^\circ, 30^\circ/30^\circ, 40^\circ/40^\circ$) that facilitates the instrument to automatically adjust the motor of the Bruker A513 variable-angle reflection accessory for the respective angles at each measurement of the instrument. This automates the varying phase angle reflectance measurements of both reference and sulfide samples. Thereby, the corresponding reflectance of the reference is measured for calibration of the respective reflectance spectra for varying phase angle and each corresponding phase angle will be used for calibrating the respective phase angle of reflectance in sulfide samples. Each measurement is taken for 100 scans and then averaged to increase the signal-to-noise ratio of the measurement.

After taking the reflectance spectra of reference sample, the sample compartment is vented and the reference is now replaced with the sulfide sample cup, the system is then evacuated, and the reflectance of the sulfide for varying phase angle is measured by following step 4. The measured reflectance spectrum at each phase angle is divided by corresponding reference spectra at the respective phase angle for the final calibrated spectra by the instrument software module. This procedure is repeated for all the sulfides (both fresh and T-processed).

Once all the measurements are taken in a particular spectral range (e.g., UV), now the detectors and beamsplitters are adjusted for another spectral range (say, MIR), and the steps 2-5 are then repeated for the respective spectral range (see, Table 4.4 for corresponding specifications).

As, we have overlapping spectral range between each spectral range, all the four spectra (UV, VIS-IR, TIR, FIR) are stitched together using IDL routine for retrieving the complete spectra (Fig. 4.9 in the main article).

Table 4.3. Samples used in the study

Sample	Crystal Structure	CAS No	Supplier	Mass (g)	Purity (%)
Calcium Sulfide (CaS)	Cubic	20548-54-3	Alfa Aesar	25	99.9
Magnesium Sulfide (MgS-1)	Cubic	12032-36-9	CHEMOS	25	99.9
Magnesium Sulfide (MgS-2)	Cubic	12032-36-9	Tailorlux	30	99
Manganese (II) Sulfide	Cubic	18820-29-6	Alfa Aesar	100	99.9
Iron (II) Sulfide (FeS)	Hexagonal	1317-37-9	Sigma Aldrich	100	99
Chromium (III) Sulfide (Cr ₂ S ₃)	Hexagonal	12018-22-3	Alfa Aesar	5	99
Titanium (IV) Sulfide (TiS ₂)	Octahedral	12039-13-3	Sigma Aldrich	10	99.9
Sodium Sulfide (Na ₂ S)	Cubic	1313-82-2	Sigma Aldrich	50	99.9

Table 4.4. Instrument specifications and spectral ranges of measurements at PSL

Sample Measurements	UV	VIS/IR	MIR (Reflectance)	MIR (Emissivity)	FIR
Bruker Vertex 80V	A	A	A	B	B
Reference	White PTFE (plastic)	Spectralon	Gold sandpaper	Blast furnace slag	Gold sandpaper
Spot size (mm)	2	2	2	49	2
Wavelength (μm)	0.2-0.5	0.4-1	1 - 25	7-14	16-100
Resolution (cm⁻¹)	8	4	4	4	4
Detector	GaP	Si diode	MCT	Nitrogen cooled MCT HgCdTe	DTGS201 (deuterated triglycine sulfate)
Beamsplitter	CaF ₂	CaF ₂	KBr Broadband	KBr	Mylar

THERMAL STABILITY AND EMISSIVITY BEHAVIOR
(7-14 μM) OF CALCIUM-SULFIDES UNDER
SIMULATED DAYTIME SURFACE CONDITIONS FOR
MULTIPLE MERCURY DAYS:
IMPLICATIONS FOR THE FORMATION OF
HOLLOWS AND CALCIUM-SULFIDE DETECTION BY
MERTIS ONBOARD THE BEPICOLOMBO MISSION

I. Varatharajan^{1,2}, C. Stangarone¹, S. Speziale³, A. Maturilli¹, J. Helbert¹, H. Hiesinger⁴, I. Weber⁴, K. E. Bauch⁴

¹Department of Planetary Laboratories, Institute of Planetary Research, German Aerospace Center (DLR), Berlin, Germany, ²Institute of Geological Sciences, Freie University (FU) Berlin, Germany, ³Helmholtz Centre Potsdam - GFZ German Research Centre for Geosciences, Potsdam, Germany, ⁴Institut für Planetologie, Westfälische Wilhelms-Universität Münster, Germany

Under Review in Earth and Planetary Science Letters (EPSL)

Preprint available at Earth and Space Science Open Archive (ESSOAr)

DOI: <https://doi.org/10.1002/essoar.10504659.1>

The author contribution is explained in the [Section 1.3](#).

KEY POINTS

- Spectral emissivity behavior (7-14 μm) of calcium-sulfides (CaS) remains stable for repeated heating cycles under simulated Mercury daytime surface conditions.
- CaS is the stable sulfide that survives the extreme thermal environment of Mercury.
- CaS is an important tracer for other sulfides those might be lost in the hollow-forming process dominated by sublimation.

5.1 ABSTRACT

Global mapping of the nature and distribution of volatiles such as sulfides on Mercury's surface is essential for understanding the thermal evolution of the planet. The surface exposure of these sulfides over extreme day-night temperature cycles (176 days; 450 °C to -170 °C) on Mercury leads to thermal weathering of these sulfide compounds. It has been seen that among the proposed sulfides on Mercury (MgS, FeS, CaS, CrS, TiS, NaS, and MnS), CaS showed relatively stable and distinctive spectral features in the thermal infrared region (TIR; 7-14 μm) when studied under the simulated Mercury day conditions for temperatures ranging from 100 °C up to 500 °C under vacuum (0.1 mbar) (Varatharajan *et al.*, 2019a). In this study, we re-investigated the stability of CaS and its spectral emissivity spectral behavior. We exposed the sample for four consecutive Earth days simulating Mercury day cycles and measured the TIR spectra of CaS for temperatures up to 500 °C (with steps of 100 °C) every day. This time the spectral analysis is coupled and supported by XRD diffraction on the fresh and temperature-processed sample, showing the mineralogical evolution with temperature. We confirm that CaS is a stable compound and therefore it would remain stable on Mercury's surface regardless of investigated peak surface temperatures. This study further implies that, for the hollows dominated by the sublimation of sulfides on Mercury (Blewett *et al.*, 2013, Helbert *et al.*, 2013a, Vilas *et al.*, 2016), CaS could be the last of the sulfides that could be mapped on Mercury as other sulfides were lost by thermal decomposition, leaving behind hollows. This could make CaS an important tracer for other sulfides, which might be lost in the hollow-forming process and supports the detection of CaS within hollows by MESSENGER (Vilas *et al.*, 2016). The emissivity spectra reported here are significant for the detection and mapping of CaS associated with hollows and pyroclastics using the Mercury Radiometer and Thermal Imaging Spectrometer (MERTIS) datasets.

5.2 INTRODUCTION

NASA's MESSENGER (Mercury Surface, Space Environment, Geochemistry, and Ranging) mission revealed that Mercury, unlike the Moon, has been formed in a highly reducing environment with sulfur abundances of up to 4 wt% (Nittler *et al.*, 2011). MESSENGER's XRS (X-Ray Spectrometer) data suggest that FeS and CaS are present in Mercury's shallow regolith, with minor MnS and NaCrS₂ (Nittler *et al.*, 2011; Weider *et al.*, 2016). Thermochemical and experimental evidence indicates that CaS is the major lithophile sulfide on Mercury (Vaughan, 2013), supported by MESSENGER XRS data, which showed a strong correlation in the detected abundances of Ca and S, suggesting the presence of minerals such as oldhamites (Nittler *et al.*, 2011, Weider *et al.*, 2012, Weider *et al.*, 2014, Weider *et al.*, 2016). Sulfides have been proposed to be present at unique sub-km scale landforms called hollows (Helbert *et al.*, 2013a). This hypothesis has been supported by the first spectral evidence of sulfide minerals (CaS, MgS) within the hollows of Dominici crater detected by MESSENGER Mercury Dual-Imaging System (MDIS) that mapped Mercury's surface in the visible-infrared spectral region (400 to 1000 nm) (Vilas *et al.*, 2016). The global spectral mapping of identified hollows and pyroclastics utilizing at wide spectral ranges will enable us to effectively map the sulfide materials across Mercury's surface (Helbert *et al.*, 2013a, Thomas *et al.*, 2014a, Thomas *et al.*, 2014b, Vilas *et al.*, 2016, Lucchetti *et al.*, 2018, Besse *et al.*, 2020).

The Mercury Radiometer and Thermal Imaging Spectrometer (MERTIS) onboard the Mercury Planetary Orbiter (MPO) of ESA/JAXA's BepiColombo mission will be the first orbital thermal infrared spectrometer (TIS) and radiometer (TIR) to map the surface mineralogy in the mid-infrared spectral range (Hiesinger *et al.*, 2010, Hiesinger *et al.*, 2020). With its two channels (TIS, TIR), MERTIS will characterize the emissivity behavior of surface materials, including sulfides, between 7 μm and 14 μm (TIS) (between 7 μm and 40 μm with TIR) with a spectral resolution of 90 nm (78 spectral channels) and a spatial resolution of 500m/pixel along with its corresponding surface temperature.

In a recent study (Varatharajan *et al.*, 2019a), the emissivity behavior of a wide range of sulfides (MgS, FeS, CaS, CrS, TiS, NaS, and MnS) within the MERTIS spectral range (7-14 μm) were studied for temperatures ranging from 100 °C up to 500 °C, with heating steps of 100 °C

under vacuum (0.1 mbar). The study showed that, among these sulfides, only CaS exhibited strong emissivity features and minor susceptibility to thermal weathering while reaching extreme temperatures of 500 °C for one simulated Mercury day (Varatharajan *et al.*, 2019a).

Mercury's surface is repeatedly exposed to extreme temperature changes, ranging from 450 °C during daytime to -170 °C during nighttime over a one day/night cycle of 176 terrestrial days (Soter and Ulrichs, 1967, Krotikov and Shchuko, 1975a). In this study, we aim at further investigating the physical/thermal and emissivity/spectral stability of CaS while exposed to an extreme thermal environment for multiple simulated Mercury days as a function of temperature (100 °C, 200 °C, 300 °C, 400 °C, and 500 °C) under vacuum (0.1 mbar) for each day (see Section 5.3.1). For the whole duration of the experiment, the vacuum was maintained inside the emissivity chamber. The physical stability of CaS is studied by X-Ray diffraction (XRD) analysis of the starting (fresh synthetic) CaS and the resulting thermally processed CaS after four simulated Mercury days (Section 5.3.2). Our study is important for understanding the thermal stability of the volatile-bearing materials such as CaS under Mercury daytime surface conditions for their effective detection from the orbit by MERTIS.

5.3 SAMPLE, FACILITY AND METHODS

For this study, the starting material used is synthetic CaS with a grain size of ~10 µm (certified by industrial supplier Alfa Aesar; CAS No. 20548-54-3) as used in the study by (Varatharajan *et al.*, 2019a). The facility and methods for emissivity and x-ray diffraction studies are explained below in Section 5.3.1 and Section 5.3.2 respectively.

5.3.1 EMISSIVITY

Planetary Spectroscopy Laboratory (PSL) is located at the Institute of Planetary Research, German Aerospace Center (DLR) in Berlin, Germany. Among the facilities present at PSL, the emissivity chamber allows to heat up various analogue materials, reaching extreme temperatures and to study their emissivity behaviors as a function of temperature (50 °C-600 °C) across a wide spectral range (1-50 µm). The systematic emissivity studies results in an extensive planetary materials emissivity library. Such specialized spectral library is created to support surface composition analyses of hot planetary targets such as Mercury, Venus, Moon,

and Io (Maturilli *et al.*, 2008, Helbert and Maturilli, 2009, Helbert *et al.*, 2013a, Helbert *et al.*, 2013b, Helbert *et al.*, 2019, Varatharajan *et al.*, 2019a). One of the three identical FTIR (Fourier transform infrared) spectrometers (Bruker Vertex 80V) at PSL is connected to the external emissivity chamber (Fig. 5.1). The spectrometer is optimized for spectral measurements under vacuum conditions (0.1 mbar). The chamber is separated from the spectrometer by a shutter and a vacuum-tight optical window between the chamber and the spectrometer, enabling the chamber to be operated under vacuum or at the desired pressure condition.

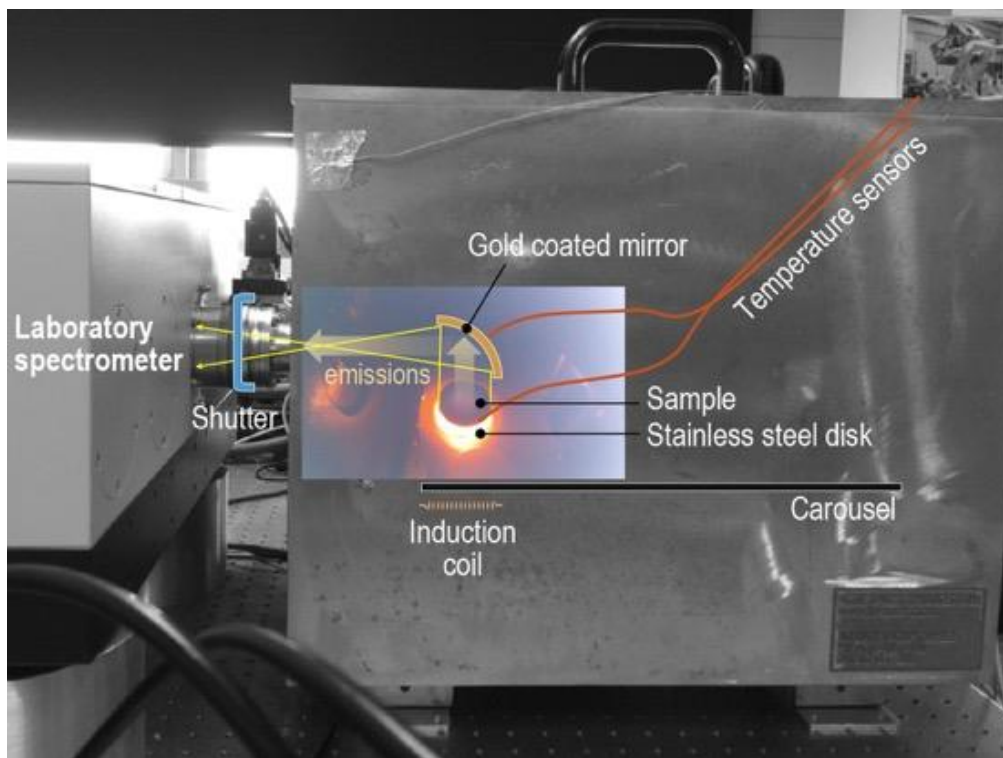


Figure 5.1. Graphical illustration of the laboratory set-up at PSL for high temperature emissivity measurements. The figure shows the heating of the sample cup using induction coil and its corresponding emissions been deflected to the Bruker 80V spectrometer using a gold-coated mirror. The image from inside the chamber was taken by a webcam during the measurement. The samples are placed in a stainless-steel disk, which is then placed on the carousel. The induction coil heats the sample cup through the carousel. The shutter between the spectrometer and the emissivity chamber enables us to physically detach the emissivity chamber and spectrometer while heating under vacuum and therefore protecting the spectrometer from continuous heat emissions. The shutter is open only while recording the measurements when sample cup reaches its desired temperatures.

For this study, the fresh CaS sample is placed in a stainless-steel cup which is then placed on a carousel, that can be rotated via a stepper motor to bring several samples to the measurement position without breaking the vacuum inside the chamber. The sample is heated from below the carousel (made of quartz glass) by an induction system. The temperature of the sample cup is controlled by adjusting the current applied to the induction coil. Three temperature sensors (thermopiles) on the sample and on the side of the sample cup, continuously monitor the bulk surface temperature, while the surrounding environment of the sample is monitored by a webcam (Fig. 5.1). The spectrometer is equipped with MCT HgCdTe detector (cooled by liquid nitrogen) and KBr beamsplitter to study the emissivity behavior of CaS at the TIR spectral region (7-14 μm) at the spectral resolution of 4 cm^{-1} under vacuum.

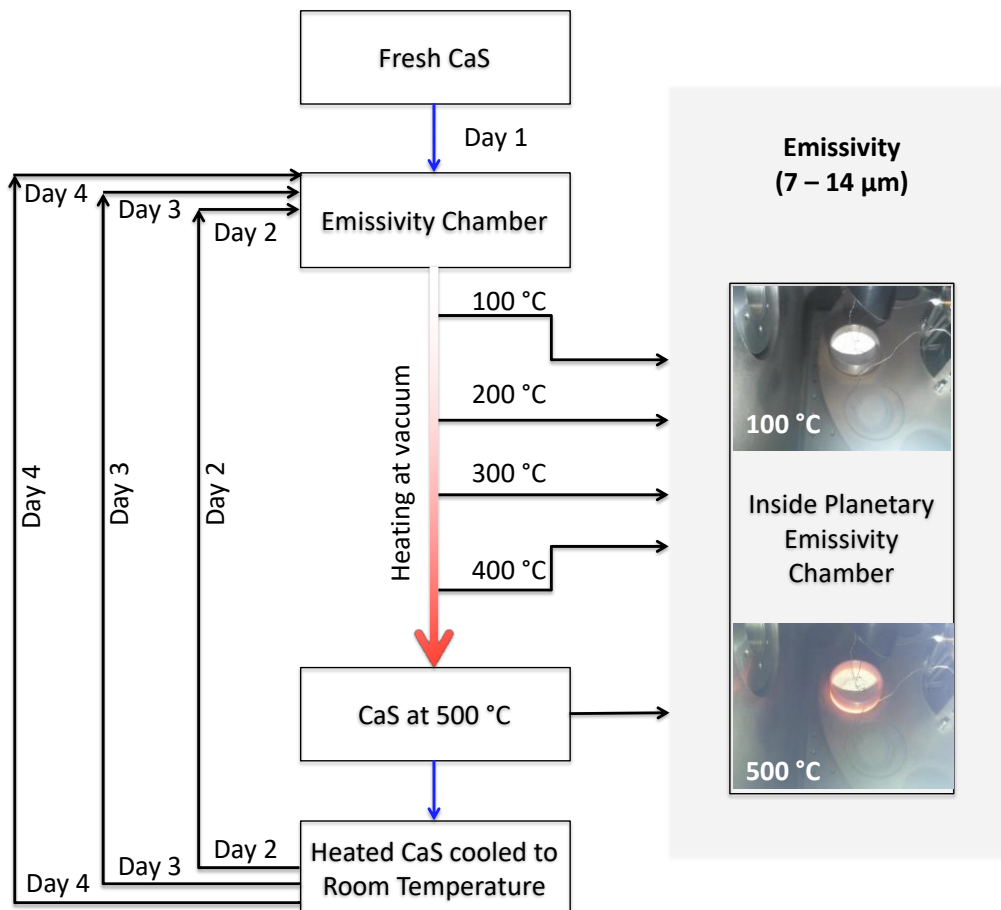


Figure 5.2. Graphical summary of the methodology used in the study to measure the emissivity of calcium sulfides (CaS) for four heating cycles during which the sample surface temperatures reach up to 500°C. The experimental set-up inside the emissivity chamber is also shown for temperatures 100 °C and 500 °C.

In this study, the emissivity spectral measurements of CaS are conducted for four simulated Mercury days each. The simple graphical flowchart of the experimental procedure is shown in Fig. 5.2. The detailed step by step experimental procedure is explained below:

1. Once the experimental setup is ready and the fresh CaS sample loaded, both the spectrometer and the chamber are slowly evacuated. Before heating up, the sample is kept under vacuum for at least 1 hour to purge it from any air trapped in the sample. In the meantime, the detector is cooled down by liquid nitrogen.

2. Once the instrument and the chamber are stabilized under vacuum conditions, CaS is slowly heated up by manually controlling the current to the induction system. When the sample surface is stable at 100 °C, the first measurement takes place. The shutter between the chamber and the spectrometer opens, allowing the spectrometer to detect the radiance coming from the heated surface of CaS. The radiance is collected and deflected by a gold (Au) coated parabolic mirror at 90° off-axis into the spectrometer. After the measurement, the shutter is closed again to avoid that any particle reaches the spectrometer optics during heating process.

3. This procedure is repeated at temperatures of 200 °C, 300 °C, 400 °C, and 500 °C, thus obtaining the emissivity measurements for 1st simulated Mercury day.

4. After the last measurement at 500 °C, the chamber and the thermally processed CaS sample cool down overnight reaching room temperature. The vacuum condition is kept constant during the entire process. During the entire heating period, the CaS sample cup is never moved and is carefully monitored with the webcam installed in the chamber to detect outgassing events.

5. Each step from 2 to 4 is repeated every day for another three consecutive Earth days simulating a Mercury day cycle where the surface reaches up to 500 °C. For all the four days of measurements, the vacuum pump is continuously operated. The samples are therefore not exposed to the atmosphere during the entire experiment (Fig. 5.2).

At the end of the measurements, the CaS sample used for the measurements is by all means thermally processed (T-processed) under Mercury daytime temperatures. All the measured emissivity spectra of CaS, which are shown in Figure 5.3, are finally calibrated against a blackbody reference at their respective measured temperatures and geometric

configurations. PSL uses blast furnace slag as a standard blackbody for the temperatures and spectral range used in this study (Maturilli *et al.*, 2013).

5.3.2 X-RAY DIFFRACTION (XRD)

In order to understand the physical stability of CaS under the extreme thermal environment of Mercury and to explain the observed changes in its spectral characteristics (Fig. 5.3), the XRD analyses of the fresh starting material (CaS) and the recovered thermally processed CaS were conducted at the Helmholtz Centre Potsdam - GFZ German Research Centre for Geosciences, Potsdam. The instrument used for the XRD analyses is a STOE STADI P powder diffractometer. The primary Cu $K_{\alpha 1}$ radiation was produced with 40 kV acceleration voltage and 40 mA beam current and a Ge (111) primary monochromator. The diffracted radiation was detected by a high-resolution DECTRIS MYTHEN detector. Measurements were performed in the range $2\theta = 5^\circ$ - 100° where 2θ is the angle between incident X-ray beam and reflected X-ray beam. The accuracy of the system was monitored before each measurement by collecting a full X-ray diffraction spectrum of Si standard (NIST 640d). The average value of the unit-cell parameter of Si is $5.430 \pm 0.001 \text{ \AA}$, which, compared to the certified value $a_0 = 5.43123 \pm 0.00008 \text{ \AA}$, corresponds to an accuracy of 0.02%.

The results obtained from the XRD measurements for starting and thermally processed CaS are shown in Fig. 5.4a and Fig. 5.4b respectively and are discussed in detail in Section 5.4.2.

5.4 RESULTS AND DISCUSSIONS

5.4.1 EMISSIVITY MEASUREMENTS

The spectral evolution of calibrated emissivity of the CaS for four simulated Mercury days is discussed below:

Simulated Mercury Day 1: With the increase of temperature from 100 to 500 °C during the first simulated Mercury day (Fig. 5.3a). We observed that: a) The band center near 7.5 μm remains constant until the sample reaches 400 °C, dropping shortwards to $\sim 7.4 \mu\text{m}$ at 500 °C; b) The emissivity shows a maximum doublet near 8.8 μm and this spectral feature does not change in strength and position when heating from 100 °C to 400 °C, whereas at 500 °C, the emissivity near the 8.3 μm spectral shoulder slightly increases; c) The band center near 9.6

μm does not change until heating up to 300 °C but slightly shifts to longer wavelengths with increasing temperatures from 300 °C to 500 °C; d) The center of the spectral shoulder near 10.2 μm and the spectral spike near 11.4 μm slightly increase with increasing temperatures from 100 °C to 500 °C; and e) The emissivity for spectral features near 7.5 μm and 9.5 μm decreases with increasing temperatures.

Simulated Mercury Day 2: Emissivity spectra of CaS at 100 °C (Fig. 5.3b; black) during Day 2 show comparatively similar spectral shapes compared to emissivity spectra of CaS at 500 °C of Day 1 (Fig. 5.3a; red). Within the spectral region of 7.5-9.5 μm , the overall spectral morphology remains stable while heating up to 500 °C. However, the spectral shape at wavelength larger than 12 μm changes drastically when the sample temperature exceeds 400 °C. Up to 300 °C, the spectral shape between 10 μm and 12 μm display a negative slope having spectral shoulders (minor peaks in emissivity) at 10.2 μm and 11.4 μm . However, at temperatures 400 °C, this spectral slope evolves into a broad emissivity band. This spectral feature is also observed in spectra taken at 500 °C with a slight increase in emissivity.

Simulated Mercury Day 3: In order to test the stability of the emissivity spectra of CaS at the end of the measurements at Day 2 (Fig.3b; red), the emissivity procedure is repeated again for Day 3. At temperature of 100 °C (Fig. 5.3c; black) during Day 3, the emissivity of CaS maintains the spectral shape of CaS at 400 °C and 500 °C during the previous day (Fig. 5.3b; red). While heating through 200°, 300°, 400°, and 500°C, the general spectral morphology of the emissivity behavior of CaS did not show any significant changes. For all temperatures, a) the emissivity of CaS during Day 3 shows minima at ~ 7.5 μm and 9.5 μm , b) the emissivity maximum shows a doublet feature centered around ~ 8.8 μm , and c) the spectral shape between 10 and 12 μm feature shows a broad spectral band in contrast to the spectral shape of Day 1.

Simulated Mercury Day 4: When the sample was heated again through the fourth simulated Mercury day (100-500 °C) under vacuum, the emissivity spectra remained unchanged with respect to the previous day (Day 3) at all respective temperatures.

At the end of the four days of emissivity measurements of the CaS sample under vacuum, a mild “rotten egg” odor was sensed while opening the chamber. This may indicate the release of S during the experiments.

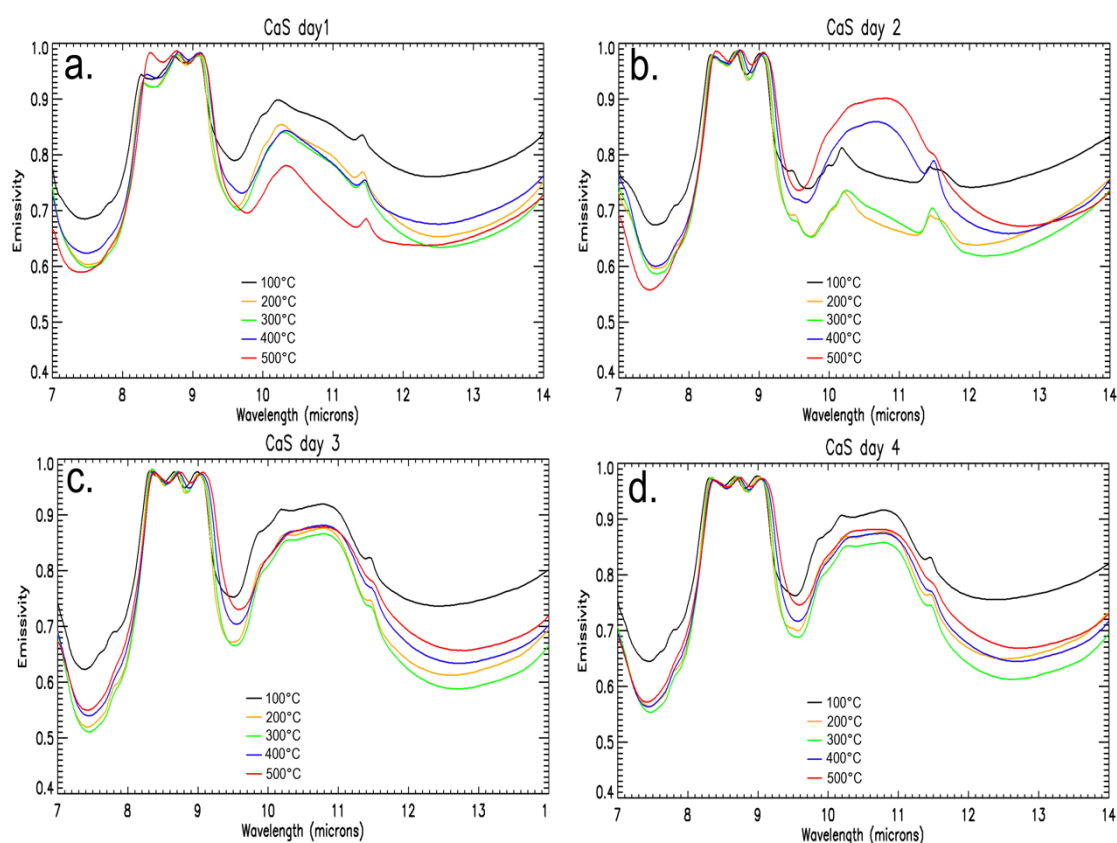


Figure 5.3. (a-d) Emissivity measurements showing emissivity behavior of CaS under four simulated Mercury daytime surface conditions where peak surface temperatures reach up to 400-500°C. (b) The evolution of an emissivity feature near 10-11 μm is observed for samples heated to >400 °C during second simulated Mercury day. (c-d) However, the spectra remained constant during the third and fourth day.

5.4.2 XRD ANALYSIS

In order to explain the changes in spectral characteristics of fresh CaS and the products after four heating cycles (Fig. 5.3), XRD analyses were conducted for the fresh starting CaS (corresponding to emissivity spectra during Day 1) and the resulting thermally processed CaS (corresponding to emissivity spectra during Day 4).

The measured XRD diffractogram of the starting/fresh CaS against the theoretical XRD diffractogram of pure CaS is plotted in Fig. 5.4a. The measured XRD diffractogram of our fresh CaS displays an extra peak (d-spacing at circa 1.35 Å) marked as red arrow in Fig. 5.4a which does not belong to the calculated XRD pattern of pure CaS. This extra peak is probably due to minor impurities in the starting material of the synthetic CaS sample. Hence, the emissivity

spectra of CaS at all temperatures for Day 1 (Fig. 5.3a) does not correspond to the emissivity spectra of pure CaS.

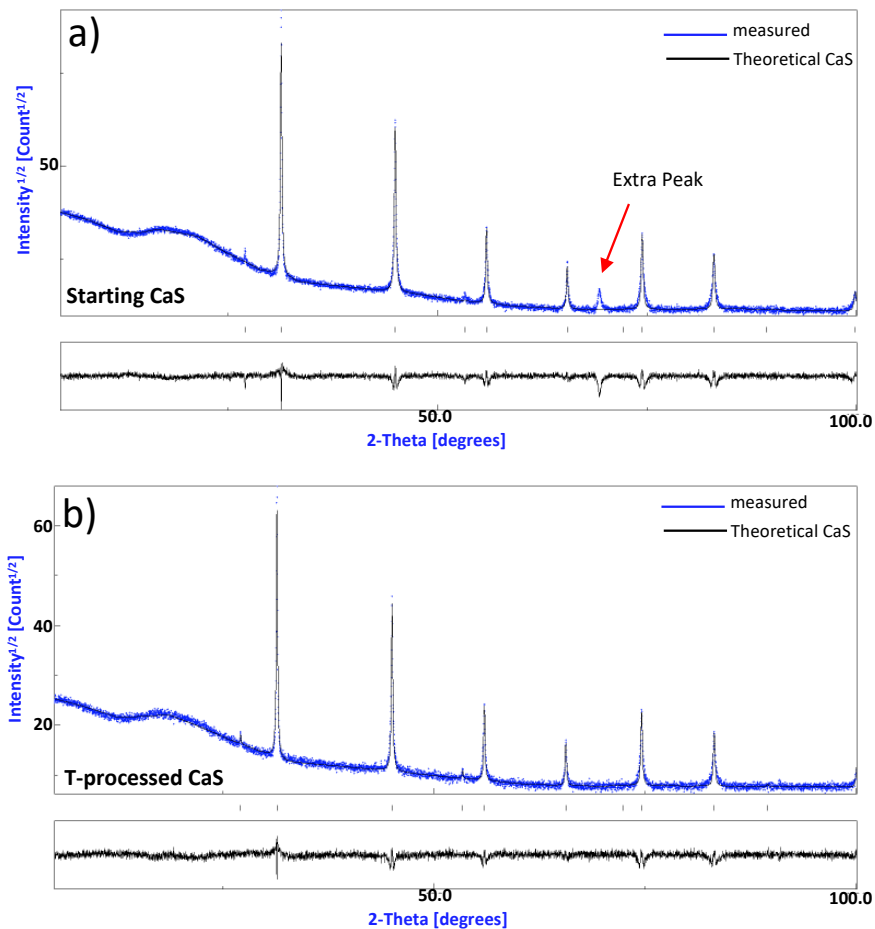


Figure 5.4. The XRD diffratogram results obtained for (a) fresh CaS and (b) thermally processed CaS after four heating cycles. The top plot for both (a) and (b) compares the measured (blue-dotted) and calculated XRD pattern of CaS (black solid). The bottom plot for both (a) and (b) shows the difference between observed and calculated XRD amplitudes of CaS. The presence of impurities in the starting/fresh CaS sample is indicated by the extra peak (d-spacing at circa 1.35 Angstrom) in the measured XRD pattern of the starting sample in (a) marked by red arrow. This extra peak (d-spacing at circa 1.35 Angstrom) disappeared in the measured XRD pattern of the thermally processed CaS in (b) which could suggest that these impurities get amorphous or cryptocrystalline or even sublimated after heating upto 500 °C.

However, this extra peak (d-spacing at circa 1.35 Angstrom) disappeared in the measured XRD pattern of the thermally processed (T-processed) CaS, which matches with all the peaks attributed to the calculated XRD pattern of pure CaS as shown in Fig. 5.4b. This disappearance of the extra peak in the T-processed CaS can be explained as, impurities within the starting sample that either become amorphous or cryptocrystalline or even sublimated in the process of repeated heating up to 500 °C (Fig 4b). The match of the peaks of the measured

XRD pattern of the thermally processed sample with the calculated XRD pattern of pure CaS (shown in Fig. 5.4b) confirms the thermal stability of CaS. Hence, the emissivity spectra of CaS at Day 4 at all temperatures correspond to the emissivity spectrum of pure CaS which is stable at even the extreme temperatures of Mercury and during repeated heating cycles.

5.5 IMPLICATIONS

Several studies (Blewett *et al.*, 2013, Helbert *et al.*, 2013a) suggested that the formation of hollows can be attributed to the thermal decomposition/sublimation of volatile-rich minerals such as sulfides constituting the hollow materials. (Thomas *et al.*, 2014a) conducted a global investigation of hollows on Mercury for its extent and size in order to understand their formation mechanism. The study showed that the hollows in the northern hemisphere are preferentially on sun-facing slopes implying a formation mechanism related to solar heating.

The emissivity of sulfides (7-14 μm) as a function of temperature under simulated Mercury daytime surface conditions showed that most of the proposed sulfides (MgS, FeS, CrS, TiS, NaS, and MnS) show spectrally evolving emissivity behavior changes with increasing surface temperatures (Varatharajan *et al.*, 2019a). This further suggests that these sulfides thermally decompose and sublime when exposed to extreme thermal environment of Mercury, and probably form hollows.

Previous studies show that Mercury's 2:3 orbital resonance has a significant impact on the latitudinal and longitudinal dependence on the peak surface temperatures during Mercury days (Soter and Ulrichs, 1967, Krotikov and Shchuko, 1975a, Vasavada *et al.*, 1999, Bauch *et al.*, 2021). Therefore, it is important to understand the maximum daytime temperature distribution of Mercury along with the spatial distribution of hollows for their effective mapping and detection (Helbert *et al.*, 2013a, Vilas *et al.*, 2016). In order to achieve this, we re-created the modeled temperature map of Mercury derived from Bauch *et al.* (2021) which was mapped for Mercury latitudes between 60 °N and 60 °S and we overlaid the globally mapped hollow groups of Thomas *et al.* (2014a) (Fig. 5.5). The locations of hollow groups are re-mapped from the supplementary file provided in Thomas *et al.* (2014a). Both surface temperature and hollow distribution are overlaid on the MESSENGER MDIS Map Projected

Low-Incidence Angle Basemap (LOI) of global monochrome map (750 nm) at a resolution of 256 pixels per degree (~ 166 m/pix) (Hawkins *et al.*, 2007, Denevi *et al.*, 2018) (Fig. 5.5).

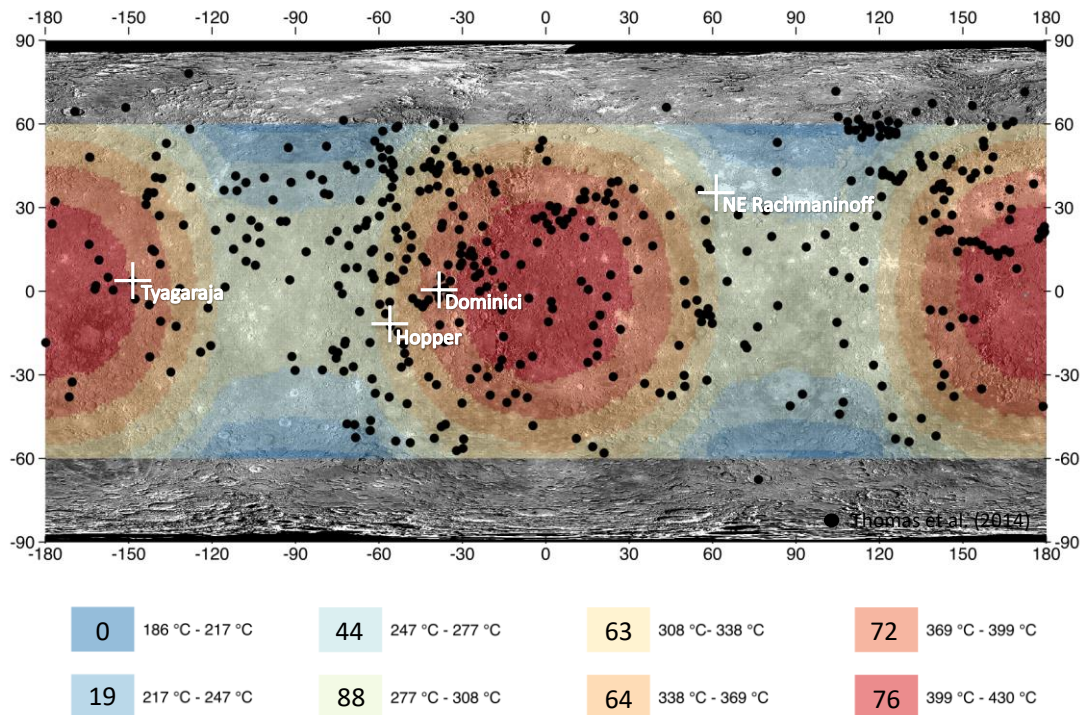


Figure 5.5 The peak surface temperature distribution across Mercury surface is mapped from (Bauch *et al.*, 2021). The surface temperatures are overlaid on the MESSENGER MDIS global Map Projected Low-Incidence Angle Basemap (LOI) data set consists of a global monochrome map (750 nm) of reflectance at a resolution of 256 pixels per degree (~ 166 m/pix) (Hawkins *et al.*, 2007, Denevi *et al.*, 2018). The black datapoints indicate the distribution of hollows across Mercury's surface mapped by Thomas *et al.* (2014). The hollows within the Tyagaraja (3.89°N, 328.9°E), Dominici (1.38°N, 323.5°E), and Hopper (12.4°S 304.1°E) craters and NE Rachmaninoff (27.6°N, 57.4°E) are marked by white crosses.

Fig. 5.5 shows that hollows are distributed globally irrespective of the varying peak surface temperatures (T_{peak}). The total number of hollows in regions between 60°N and 60°S with peak daytime surface temperatures above ~ 300 °C (orange to red; Fig. 5.5) and below ~ 300 °C (blue to yellow; Fig. 5.5) are 275 and 151 respectively. Some notable examples are volcanic materials within the NE Rachmaninoff basin (27.6°N, 57.4°E) which are located within the temperature regime ~ 277 °C $< T_{\text{peak}} < \sim 308$ °C (light green) whereas hollows within the Tyagaraja (3.89°N, 328.9°E) and Dominici (1.38°N, 323.5°E) craters are located in areas within ~ 369 °C $< T_{\text{peak}} < \sim 399$ °C (intermediate red). Hopper (12.4°S, 304.1°E) crater is located within the temperature regime ~ 308 °C $< T_{\text{peak}} < \sim 338$ °C (yellow) in Fig. 5.5. This compels the

need for study for creating unique spectral library of various hollow-forming materials such as sulfides as a function of varying surface temperatures of Mercury (Varatharajan *et al.*, 2019a).

CaS belongs to the group of proposed sulfides of Mercury that constitute the chemical composition of surface features of presumably volcanic origin – such as hollow-forming minerals and pyroclastics (Helbert *et al.*, 2013a, Vilas *et al.*, 2016, Besse *et al.*, 2020). In volcanic terrains, CaS has been proposed and spectrally detected in the hollows in visible-infrared spectral region using the MDIS data (Helbert *et al.*, 2013a, Vilas *et al.*, 2016). Varatharajan *et al.* (2019) demonstrated that most sulfides (MgS, FeS, CrS, TiS, NaS, and MnS) except for CaS are both physically and spectrally unstable when exposed to extreme daytime thermal environment of Mercury. The results from our study where CaS is exposed to repeated heating cycles under simulated Mercury daytime surface conditions (up to 500 °C), strongly suggest that CaS is the most stable sulfide against thermal weathering on Mercury's surface. This indirectly suggests that unlike other sulfides (MgS, FeS, CrS, TiS, NaS, and MnS), CaS may not significantly contribute to hollow formation on Mercury by solar heating as CaS does not decompose with repeated heating cycles even under extreme temperatures reaching up to 500 °C. This would make CaS (if detected and mapped by MERTIS) a good tracer for sulfides (possibly among other volatiles) on Mercury that leads to formation of hollows, as other sulfides are lost in sublimation leaving behind the hollows.

In fact, CaS was successfully detected within the hollows of Dominici and Hopper craters (Vilas *et al.*, 2016) and these craters occur in surface regions where peak temperatures reach ~400 °C as marked in Fig. 5.5 Future studies that combine the global mapping of CaS, the extent and depth of hollows bearing CaS and other sulfides will give further insight into the nature of volatiles on Mercury's surface and its interior as well as hollow forming mechanisms. As the emissivity behavior of pure CaS does not evolve with increasing surface temperatures, CaS can be globally mapped irrespective of the peak surface temperatures/heating cycles across Mercury.

Furthermore, the spectral investigation of various sulfides by Varatharajan *et al.* (2019) showed that the TIR spectral region is sensitive for the detection and characterization of sulfide minerals under Mercury daytime conditions. Hence, MERTIS onboard the BepiColombo mission will support the global mapping of volatiles on Mercury's surface and will help understanding the hollow forming mechanisms and its materials. Ultimately, such studies will

help calculating the volatile budget of Mercury's interior and its contributions to Mercury's exosphere.

5.6 CONCLUSIONS

In this study, the physical and spectral stability of CaS has been investigated for four simulated Mercury days (heating cycles). The study indicates that calcium sulfide (CaS) is stable on Mercury's surface with emissivity spectra retaining their characteristic features irrespective of surface temperatures and repeated heating cycles typical for Mercury. At all surface temperatures, the presence of CaS on Mercury surface can be identified by its emissivity behavior in the TIR spectral region (7-14 μm) which is characterized by a) a spectral minimum at $\sim 7.5 \mu\text{m}$ and $9.5 \mu\text{m}$, b) an emissivity maximum centered around $\sim 8.8 \mu\text{m}$ with a peak doublet, and c) a broad spectral band between 10 and 12 μm . Our study demonstrates that CaS is the least thermally weathered sulfide among those expected on Mercury's surface, making it a good tracer for the presence of sulfides (possibly among other volatiles) associated with hollows and pyroclastics when globally mapped by MERTIS. The unique spectral library provided with this work will support global mapping of CaS around hollows and pyroclastic materials of Mercury surface using MERTIS payload onboard BepiColombo mission. The global mapping of CaS along with other sulfides across hollows will further help our understanding of the hollow formation mechanism dominated by sublimation process.

5.7 ACKNOWLEDGEMENTS

IV thank DLR/DAAD Doctorate Fellowship for funding her PhD work at PSL-DLR. A portion of this research was supported by the European Union's Horizon 2020 research and innovation program. Europlanet 2020 RI has received funding from the European Union's Horizon 2020 research and innovation programme under grant agreement No 654208.

THERMAL INFRARED SPECTROSCOPY (7-14 μM)
OF SILICATES UNDER SIMULATED MERCURY
DAYTIME SURFACE CONDITIONS
AND THEIR DETECTION:
SUPPORTING MERTIS ONBOARD THE
BEPICOLOMBO MISSION

I. Varatharajan^{1,2}, C. Stangarone¹, F. D. H. Wilke³, A. Maturilli¹, J. Helbert¹,
H. Hiesinger⁴, I. Weber⁴

¹Department of Planetary Laboratories, Institute of Planetary Research, German Aerospace Center (DLR), Berlin, Germany, ²Institute of Geological Sciences, Freie University (FU) Berlin, Germany, ³GFZ German Research Centre for Geosciences, Telegrafenberg, 14473 Potsdam, Germany, ⁴Institut für Planetologie, Westfälische Wilhelms-Universität Münster, Germany

Submitted to Icarus

Preprint available at Earth and Space Science Open Archive (ESSOAr)

DOI: <https://doi.org/10.1002/essoar.10504660.1>

The author contribution is explained in the [Section 1.3](#).

KEY POINTS

- Spectral emissivity of powdered silicates (7-14 μm) under simulated Mercury Daytime conditions are studied.
- Silicates show strong and distinct spectral features in thermal IR (7-14 μm) spectral region.
- Christiansen Feature (CF) and Restrahland Band (RB1) of silicates varies with temperatures under vacuum.
- CF vs RB1 plot can uniquely distinguish major silicate groups in the emissivity spectral region.

7

THE MERCURY RADIOMETER AND THERMAL INFRARED IMAGING SPECTROMETER (MERTIS) ONBOARD BEPICOLOMBO: FIRST INFLIGHT CALIBRATION RESULTS

M. D'Amore¹, J. Helbert¹, A. Maturilli¹, I. Varatharajan^{1,2}, B. Ulmer³, T. Säuberlich¹, R. Berlin¹,
G. Peter¹, H. Hiesinger⁴, G. Arnold¹

¹Department of Planetary Laboratories, Institute of Planetary Research, German Aerospace Center (DLR), Berlin, Germany, ²Institute of Geological Sciences, Freie University (FU) Berlin, Germany, ³Ingenieurbüro Bernd Ulmer, Frankfurt Oder, Germany; ⁴University of Muenster, Institute for Planetology, Muenster, Germany.

Published in SPIE Proceedings 11128, Infrared Remote Sensing and Instrumentation XXVII,
September 2019

DOI: <https://doi.org/10.1117/12.2529089>

The author contribution is explained in the Section 1.3.

8

CONCLUSIONS

8.1 SUMMARY

This chapter summarizes the main findings of the four presented studies (Chapters 2,4,5,6) and discusses their relevance in the broader scientific context. The chapter 3 and 7 are published work which describes the working capabilities of PSL spectroscopy facility and BepiColombo's MERTIS instrument respectively.

8.1.1 SURFACE SCIENCE FROM MASCS SPECTROMETER

In chapter 2, the global multivariate spectral analysis was carried out on the NASA MESSENGER visible-infrared hyperspectral reflectance spectrometer (MASCS) datasets and the study is currently under revision with JGR planets (Varatharajan *et al.*, 2020a). This study aimed at mapping the spectral heterogeneity across the Mercury's surface and to correlate their differences along with the known geochemical units derived by (Vander Kaaden *et al.*, 2017). MASCS is a point spectrometer with its datapoints scattered unevenly over Mercury surface where each pixel has different spatial resolution, and this was one of the serious drawbacks to perform global analysis. In the presented work, this limitation is overcome by resampling the data to a uniform equal-angular grid of 1 pixel per degree which mimicked the global imaging spectrometer data format. The global multivariate analysis such as standard spectral parameter maps, k-means clustering, and principal component analysis (PCA) was then applied to this datacube to spectrally characterize Mercury's surface. The presented results demonstrated that among these different methods, PCA proves to be an efficient tool which brings out the spectral heterogeneity among the various geochemical terrains of Mercury. The principal component (PC) 6 specifically correlates to both chemical and physical properties of the surface and therefore enabling us to identify surface units based on grain size, the presence of amorphous materials, and space-weathering associated alterations. Further, the PC false color composite map (FCC) made from PCs 1, 2, and 6 effectively distinguished diverse spectral heterogeneity across Mercury's surface. One of the main

highlights of the presented study include, the two northern volcanic plains' geochemical regions; the high-Mg and low-Mg terrains was spectrally classified for the first-time using reflectance spectrometer data which was achieved from the FCC created from the PCs 1,2 and 6. However, a direct investigation of the surface mineralogy is still missing due to absence of any diagnostic absorption features that distinctively distinguishes these two units. In order to achieve this, the spectral range beyond the VNIR coverage provided by MESSENGER is required which will be achieved by the MERTIS payload onboard BepiColombo mission which will map the Mercury surface at 7-14 μm spectral region which will provide the direct measure of the Si-O abundance of the bulk silicate mineralogy, in addition to identifying the sulfide mineralogy within the hollows. Furthermore, the radiometer channel of MERTIS will investigate the regolith physical properties, such as grain size and thermal inertia, and therefore assist the testing of the correlation of PC6 with fine-grained, and the least space-weathered surface materials. This presented work therefore emphasizes the diversity of Mercury's surface materials and the importance of global mineral mapping with greater detail to understand the planet's geological evolution, its volatile budget, and ongoing surface processes.

8.1.2 SPECIALIZED SPECTRAL LIBRARY UNDER SIMULATED DAYTIME SURFACE CONDITIONS OF MERCURY

To detect the mineral diversity of a planet's surface, it is essential to study the spectral variations over a broad wavelength range at relevant simulated laboratory conditions. With MERTIS onboard BepiColombo aiming to map the surface mineralogy and its diversity on Mercury surface, it is important to understand the change in emissivity behaviour of wide range of Mercury analogues under extreme thermal environment conditions of Mercury where daytime surface temperatures can reach upto 500°C (Vasavada *et al.*, 1999). In order to facilitate the realistic mineral mapping, a specialised spectral library is required to be built under controlled laboratory conditions by imitating the Mercury's daytime surface environment conditions. In this thesis, the presented study includes a new emissivity spectral library of wide range of sulfides and silicate analogues of Mercury as a function of temperature under vacuum. The spectral library was built using the planetary emissivity chamber facility at DLR, Berlin which is briefly described in Chapter 3. This section summarises the results

obtained in the emissivity study of these fine-grained Mercury analogues to supplement the fine-grained nature of Mercury regolith (Shevchenko, 2002).

8.1.2.1 SULFIDE MINERALOGY

NASA MESSENGER data revealed that irrespective of Mercury's closeness to the Sun, Mercury is richer in volatiles especially sulfur (S) with an average abundance of 4 wt% (Nittler *et al.*, 2011). This sulfur are proposed to be brought to the surface as sulfides in the form of slag deposits in Mercury's hollows and pyroclastic deposits (Helbert *et al.*, 2013a). (Vilas *et al.*, 2016) successfully identified the presence of CaS and MgS within the Dominici and Hopper hollows using MESSENGER's MDIS datasets in comparison with the laboratory spectra obtained at PSL. However, comprehensive spectral library of sulfide minerals measured under vacuum conditions in a wide spectral range (0.2-100 μm) was lacking. This affects the detectability and understanding of the distribution, abundance, and type of sulfides on Mercury using remote-sensing spectral observations. To address this, the presented work in chapter 4 reports the unique spectral library which includes a) the emissivity spectroscopy of 7 powdered (<10 μm grain size) synthetic sulfides including MgS, FeS, CaS, CrS, TiS, NaS, and MnS as a function of temperature under vacuum and b) the UV-FIR reflectance spectroscopy of the fresh and thermally weathered sulfides counterparts. The presented study is published in EPSL as (Varatharajan *et al.*, 2019a). The emissivity measurements were performed in the TIR spectral range (\sim 7-14 μm) for sample temperatures from 100°C-500°C, covering the daytime temperature cycle on Mercury's surface. The measured spectral reflectance of fresh and thermally processed sulfides includes a wide spectral range (0.2-100 μm) at four different phase angles, 26°, 40°, 60°, 80°. The presented work also catalogues the diagnostic spectral bands for identification of these sulfides to support analyze of existing and future datasets. The emissivity study showed that among all sulfides, CaS was relatively stable showing distinctive spectral features while undergoing rise in temperature for one Mercury day which could be mapped effectively if presented in MERTIS datasets. The presented work also shows that reflectance spectra of studied sulfides show less variation with phase angle at shorter wavelength along with the distinctive 0.3 μm spectral feature for all sulfides. This spectral feature could be further exploited in the MASCS UVVIS datasets to map the distribution of sulfides across the Mercury's surface. The newly created spectral library in the presented work is already used in the study by (Besse *et al.*, 2020) which explores the spectral nature of

selected pyroclastic deposits of the Mercury surface. Besse et al. (2020) reports the similarity between the MASCS spectra of the pyroclastic deposits and the measured sulfides spectra reported in chapter 4. This unique spectral library will therefore facilitate the detection of sulfides by spectrometers onboard MESSENGER (MASCS and MDIS) and BepiColombo (MERTIS and SIMBIO-SYS/VIHI).

The physical, thermal, and emissivity spectral stability of CaS were further re-investigated under repeated exposure to extreme thermal environment of Mercury daytime surface conditions. To achieve this, CaS sample was heated from room temperature to 500°C and the emissivity spectra in 7-14 μm is measured while reaching temperatures at 100°C, 200°C, 300°C, 400°C, and 500°C under vacuum (0.1 mbar) for simulated Mercury days. The XRD diffractogram analysis were further conducted for the fresh and thermally processed CaS samples. This study showed that CaS is the only stable sulfide that could be mapped on the Mercury surface among proposed sulfur-related volatiles (MgS, FeS, CaS, CrS, TiS, NaS, and MnS) on Mercury. This suggests that for the hollow forming mechanisms dominated by sublimation, detection of CaS could act as potential tracers of sulfides which are otherwise lost in the thermal decomposition under extreme thermal environment of Mercury. MERTIS will therefore aid the global mapping of CaS of Mercury surface and help in understanding the volatile budget of the Mercury interior.

8.1.2.2 SILICATE MINERALOGY

MESSENGER's MASCS and MDIS datasets reveal that Mercury surface spectra in the VNIR spectral region displays a featureless and red-sloped spectrum for the major surface units due to the presence of Fe-poor silicate mineralogy of the planet's surface. This nature of Mercury surface therefore limits the direct mineral mapping of the surface in the VNIR spectral region and will be overcome by TIR (7-14 μm) mapping of Mercury surface by BepiColombo's MERTIS as this spectral region is sensitive to Si-O based mineralogy irrespective of the transition metals. In chapter 6, the emissivity spectra of the finely grained (<25 μm) silicate analogues of Mercury are studied under simulated daytime surface conditions of Mercury. The studied silicate analogues include a) olivine (a Mg-rich forsterite), b) pyroxenes (diopside, enstatite, and hypersthene), c) feldspars (plagioclase group; anorthite, labradorite, andesine, oligoclase, and K-feldspar; microcline) and d) feldspathoid (nepheline)

as suggested by (Helbert et al., 2007; Namur and Charlier, 2017; Vander Kaaden et al., 2017) through telescope data and geochemistry suite data of MESSENGER. In the presented work, the specialized spectral library which includes the emissivity spectra of these as a function of temperature (increasing from 100°C, up to 500°C, with T steps of 100°C) under vacuum are reported in the spectral range of 7-14 μm at 4 cm^{-1} spectral resolution. Furthermore, spectral parameters such as Christiansen Feature (CF) position, first Reststrahlen band (RB1) position, RB1 emissivity, and RB spectral contrast were derived for all temperatures for each mineral to understand their change in spectral behavior as a function of temperature and their detection from the orbit. The study showed that with increase in temperatures, RB1 position shifts to higher wavelengths, RB1 emissivity decreases, and RB spectral contrast increases respectively for all the silicates studied. The reported study introduces the CF vs RB1 for the first-time which aids in unambiguously discriminate the major silicate groups such as feldspars, pyroxenes, and olivine regardless of the temperature at which they were measured. The resulting highlight of the study is that this CF vs RB1 plot can be widely used to map the igneous surface mineralogy of various silicate targets such as Moon, Mars, and S-type asteroids in the 7-14 μm spectral region in remote sensing via orbit and ground based telescope observations.

8.2 IMPLICATIONS

The results presented in this work have important implications in identifying and mapping the global mineral diversity of Mercury surface materials which was missing till now. The unique emissivity spectral library of silicates and sulfides in the TIR (7-14 μm) spectral region will aid the direct surface mineral mapping of Mercury surface at 500 m/pixel using MERTIS datasets when BepiColombo reaches orbit by 2026. The long cruise phase of BepiColombo not only enables us to be prepared with the required spectral library, it also helps us to expand the list of Mercury analogue minerals that can be included to the list.

The global multivariate analysis of MASCS datasets at spatial binning of 1ppd reveals the spectral heterogeneity of major geochemical terranes of Mercury and for the first time spectrally distinguishes the low-Mg and high-Mg units of northern volcanic plains (Varatharajan *et al.*, 2020a). SIMBIO-SYS/VIHI onboard BepiColombo will be mapping these

geochemical terranes at a spatial resolution of 500 m/pixel along with MERTIS data, combined together they become a powerful source to decipher directly the planet's surface mineralogy and its geomorphologic relations for the first time. The temperature dependent specialised spectral library being build will aid in deciphering the respective mineralogies of these surfaces. With BepiColombo on its way to Mercury, the global multivariate analysis of the very high spatial resolution hyperspectral VNIR+MIR data from SIMBIO-SYS VIHI and MERTIS will help to understand the spectral and mineralogical diversities within various geochemical units of Mercury.

The varying phase angle investigation of the reflectance spectroscopy of sulfides developed in this study for both fresh and thermally weathered counterparts in the wide spectral range of 0.2-100 μm can be used to map the volatile-rich mineral deposits on the planet by both MESSENGER and BepiColombo datasets. The 0.3 μm features of the sulfides are characteristically distinctive and not affected by the phase angle variations. This spectral feature can be used to search for sulfides in the existing the MASCS UVVIS datasets. Furthermore, the emissivity mapping of these sulfides using MERTIS data will provide both the spatial and mineralogical diversity of the volatile-rich materials. This will be the key in understanding the nature of the Mercury interior and its thermal evolution.

The mineral interpretation of the Mercury surface in the past telescope data (Sprague *et al.*, 1994, Emery *et al.*, 1998, Sprague *et al.*, 2000, Sprague *et al.*, 2002, Sprague *et al.*, 2009) has only been studied using spectral unmixing techniques with endmember materials whose spectral reflectance (inverted to derive emissivity using Kirchoff's law, see Chapter 1) have been measured at room temperature. The presented work in this thesis evidently shows that the spectral behaviour of the silicates and sulfides change in their spectral shape at different temperatures. Using this specialized endmember spectral library created under Mercury's conditions should therefore significantly increase the accuracy of the deconvolution model results of not only MERTIS but also telescopic observations of Mercury (Varatharajan *et al.*, 2018). Therefore, this specialised temperature dependent emissivity spectral library can be widely used in the new spectral unmixing analysis of past and new TIR telescope observations of Mercury to be prepared for MERTIS data analysis. The newly introduced CF vs RB1 plot further promises wider implications in identifying the wider silicate groups of igneous

mineralogy of Mercury and can be extended to various other silicate targets such as Moon, Mars, and S-type asteroids for both orbit and telescope observations.

This thesis advances the study of Mercury with orbital and telescope spectroscopy by contributing the specialised spectral library of Mercury analogue minerals under simulated daytime surface conditions of Mercury. The spectral analysis approach such as PCA can be further extended to the BepiColombo datasets to aid the spectral characterisation of Mercury surface at greater spatial resolution. Due to the highly elliptical orbit of MESSENGER, the southern hemisphere of the planet is barely mapped for its chemical composition. BepiColombo's geochemistry and spectroscopy instrument suite will fill this gap and provide with the global perspective of the planet at greater spatial resolution. MERTIS will provide the new set of spectral datasets at TIR spectral range which will unveil the silicate make-up of the planet and may give us the new estimates of volatile wt%. BepiColombo will therefore answer the key questions such as volatile budget of the planet, the silicate make-up and extent of volcanic minerals, the mineralogy of primordial crust of Mercury, the presence of graphite in the form of possible floatation crust, the compositional differences along the crustal stratigraphy, on-going space weathering processes and put together will answer the Mercury formation, internal thermal evolution, and the processes that shape the surface of the planet. The new temperature dependent spectral library built and its related spectral analysis for emissivity in the TIR spectral range will aid in answering these questions with the return of BepiColombo datasets.

BIBLIOGRAPHY

- ARMSTRONG, J. T. 1995. Citzaf-a package of correction programs for the quantitative Electron Microbeam X-Ray-Analysis of thick polished materials, thin-films, and particles. *Microbeam Analysis*, 4, 177-200.
- BANDFIELD, J. L. & ROGERS, A. D. 2019. Thermal Infrared Spectral Modeling. *Remote Compositional Analysis: Techniques for Understanding Spectroscopy*, 324-336.
- BAUCH, K. E., HIESINGER, H., GREENHAGEN, B. T. & HELBERT, J. 2021. Estimation of surface temperatures on Mercury in preparation of the MERTIS experiment onboard BepiColombo. *Icarus*, 354, 114083.
- BELL, J. F. 1997. VISIBLE AND NEAR-INFRARED SPECTROSCOPY (VIS-NIR) Visible and near-infrared spectroscopy. *Encyclopedia of Planetary Science*. Dordrecht: Springer Netherlands.
- BENZ, W., ANIC, A., HORNER, J. & WHITBY, J. A. 2008. The Origin of Mercury. In: BALOGH, A., KSANFOMALITY, L. & VON STEIGER, R. (eds.) *Mercury*. New York, NY: Springer New York.
- BESSE, S., DORESSOUNDIRAM, A., BARRAUD, O., GRITON, L., CORNET, T., MUÑOZ, C., VARATHARAJAN, I. & HELBERT, J. 2020. Spectral Properties and Physical Extent of Pyroclastic Deposits on Mercury: Variability Within Selected Deposits and Implications for Explosive Volcanism. *Journal of Geophysical Research: Planets*, 125, e2018JE005879.
- BESSE, S., DORESSOUNDIRAM, A. & BENKHOFF, J. 2015. Spectroscopic properties of explosive volcanism within the Caloris basin with MESSENGER observations. *Journal of Geophysical Research: Planets*, 120, 2102-2117.
- BISHOP, J., BELL III, J. & MOERSCH, J. E. 2019. *Remote Compositional Analysis: Techniques for Understanding Spectroscopy, Mineralogy, and Geochemistry of Planetary Surfaces*, Cambridge, Cambridge University Press.
- BLEWETT, D. T., CHABOT, N. L., DENEVI, B. W., ERNST, C. M., HEAD, J. W., IZENBERG, N. R., MURCHIE, S. L., SOLOMON, S. C., NITTLER, L. R., MCCOY, T. J., XIAO, Z., BAKER, D. M. H., FASSETT, C. I., BRADEN, S. E., OBERST, J., SCHOLTEN, F., PREUSKER, F. & HURWITZ, D. M. 2011. Hollows on Mercury: MESSENGER Evidence for Geologically Recent Volatile-Related Activity. *Science*, 333, 1856-1859.
- BLEWETT, D. T., HAWKE, B. R., LUCEY, P. G. & ROBINSON, M. S. 2007. A Mariner 10 color study of mercurian craters. *Journal of Geophysical Research: Planets*, 112.
- BLEWETT, D. T., LEVY, C. L., CHABOT, N. L., DENEVI, B. W., ERNST, C. M. & MURCHIE, S. L. 2014. Phase-ratio images of the surface of Mercury: Evidence for differences in sub-resolution texture. *Icarus*, 242, 142-148.
- BLEWETT, D. T., ROBINSON, M. S., DENEVI, B. W., GILLIS-DAVIS, J. J., HEAD, J. W., SOLOMON, S. C., HOLSCLAW, G. M. & MCCLINTOCK, W. E. 2009. Multispectral images of Mercury

- from the first MESSENGER flyby: Analysis of global and regional color trends. *Earth and Planetary Science Letters*, 285, 272-282.
- BLEWETT, D. T., VAUGHAN, W. M., XIAO, Z., CHABOT, N. L., DENEVI, B. W., ERNST, C. M., HELBERT, J., D'AMORE, M., MATURILLI, A., HEAD, J. W. & SOLOMON, S. C. 2013. Mercury's hollows: Constraints on formation and composition from analysis of geological setting and spectral reflectance. *Journal of Geophysical Research: Planets*, 118, 1013-1032.
- BOOYSEN, R., GLOAGUEN, R., LORENZ, S., ZIMMERMANN, R. & NEX, P. A. M. 2020. Geological Remote Sensing. *Reference Module in Earth Systems and Environmental Sciences*. Elsevier.
- BORA, M., JYOTI, D., GUPTA, D. & KUMAR, A. 2014. Effect of different distance measures on the performance of K-means algorithm: an experimental study in Matlab. *arXiv preprint arXiv:1405.7471*.
- BOTT, N., DORESSOUNDIRAM, A., ZAMBON, F., CARLI, C., GUZZETTA, L., PERNA, D. & CAPACCIONI, F. 2019. Global spectral properties and lithology of Mercury: the example of the Shakespeare (H-03) quadrangle. *Journal of Geophysical Research: Planets*, 0.
- ÇENGEL, Y. A., TURNER, R. H., CIMBALA, J. M. & KANOGLU, M. 2001. *Fundamentals of thermal-fluid sciences*, McGraw-Hill New York.
- CHANCE, K. & MARTIN, R. V. 2017. *Spectroscopy and Radiative Transfer of Planetary Atmospheres*, Oxford University Press.
- CHAPMAN, C. R. 1988. Mercury: Introduction to an end-member planet. *Mercury*, 1-23.
- CHIHARA, H., KOIKE, C. & TSUCHIYAMA, A. 2001. Low-temperature optical properties of silicate particles in the far-infrared region. *Publications of the Astronomical Society of Japan*, 53, 243-250.
- CHRISTENSEN, P. R., BANDFIELD, J. L., HAMILTON, V. E., HOWARD, D. A., LANE, M. D., PIATEK, J. L., RUFF, S. W. & STEFANOV, W. L. 2000. A thermal emission spectral library of rock-forming minerals. *Journal of Geophysical Research: Planets*, 105, 9735-9739.
- CLARK, P. E. & RILEE, M. L. 2010. *Remote sensing tools for exploration: observing and interpreting the electromagnetic spectrum*, Springer Science & Business Media.
- CLOUTIS, E., BECK, P., GILLIS-DAVIS, J. J., HELBERT, J. & LOEFFLER, M. J. 2019. Effects of Environmental Conditions on Spectral Measurements. *Remote Compositional Analysis: Techniques for Understanding Spectroscopy*, 289-306.
- CONEL, J. E. 1969. Infrared emissivities of silicates: Experimental results and a cloudy atmosphere model of Spectral emission from condensed particulate mediums. *Journal of Geophysical Research (1896-1977)*, 74, 1614-1634.
- COOPER, B., POTTER, A., KILLEN, R. & MORGAN, T. 2001. Midinfrared spectra of Mercury. *Journal of Geophysical Research: Planets*, 106, 32803-32814.
- COOPER, B. L., SALISBURY, J. W., KILLEN, R. M. & POTTER, A. E. 2002. Midinfrared spectral features of rocks and their powders. *Journal of Geophysical Research: Planets*, 107, 1-1-17.

- D'AMORE, M., HELBERT, J., MATURILLI, A., VARATHARAJAN, I., ULMER, B., SÄUBERLICH, T., BERLIN, R., PETER, G., HIESINGER, H. & ARNOLD, G. 2019. *The mercury radiometer and thermal infrared imaging spectrometer (MERTIS) onboard Bepi Colombo: first inflight calibration results*, SPIE.
- D'AMORE, M., HELBERT, J., MATURILLI, A., VARATHARAJAN, I., ULMER, B., SÄUBERLICH, T., BERLIN, R., PETER, G., WALTER, I., HIESINGER, H., MARTINEZ, S., LANDALUCE, I. O. D. & CASALE, M. 2018. *Data processing of the Mercury radiometer and thermal infrared imaging spectrometer (MERTIS) onboard Bepi Colombo*, SPIE.
- D'INCECCO, P., HELBERT, J., D'AMORE, M., MATURILLI, A., HEAD, J. W., KLIMA, R. L., IZENBERG, N. R., MCCLINTOCK, W. E., HIESINGER, H. & FERRARI, S. 2015. Shallow crustal composition of Mercury as revealed by spectral properties and geological units of two impact craters. *Planetary and Space Science*, 119, 250-263.
- DE HON, R., SCOTT, D. & UNDERWOOD JR, J. 1981. Geologic map of the Kuiper (H-6) quadrangle of Mercury. *United States Geological Survey, Geologic Investigations Series, Map I-1233*.
- DEER, W. A., FRS, HOWIE, R. A. & ZUSSMAN, J. 2013. *An Introduction to the Rock-Forming Minerals*, Mineralogical Society of Great Britain and Ireland.
- DENEVI, B. W., CHABOT, N. L., MURCHIE, S. L., BECKER, K. J., BLEWETT, D. T., DOMINGUE, D. L., ERNST, C. M., HASH, C. D., HAWKINS, S. E., III, KELLER, M. R., LASLO, N. R., NAIR, H., ROBINSON, M. S., SEELOS, F. P., STEPHENS, G. K., TURNER, F. S. & SOLOMON, S. C. 2018. Calibration, Projection, and Final Image Products of MESSENGER's Mercury Dual Imaging System. *Space Science Reviews*, 214.
- DENEVI, B. W., ERNST, C. M., MEYER, H. M., ROBINSON, M. S., MURCHIE, S. L., WHITTEN, J. L., HEAD, J. W., WATTERS, T. R., SOLOMON, S. C., OSTRACH, L. R., CHAPMAN, C. R., BYRNE, P. K., KLIMCZAK, C. & PELOWSKI, P. N. 2013. The distribution and origin of smooth plains on Mercury. *Journal of Geophysical Research: Planets*, 118, 891-907.
- DENEVI, B. W., ROBINSON, M. S., SOLOMON, S. C., MURCHIE, S. L., BLEWETT, D. T., DOMINGUE, D. L., MCCOY, T. J., ERNST, C. M., HEAD, J. W., WATTERS, T. R. & CHABOT, N. L. 2009. The Evolution of Mercury's Crust: A Global Perspective from MESSENGER. *Science*, 324, 613-618.
- DILNER, D. 2016. Thermodynamic description of the Fe–Mn–Ca–Mg–S system. *Calphad*, 53, 55-61.
- DOMINGUE, D. L., CHAPMAN, C. R., KILLEN, R. M., ZURBUCHEN, T. H., GILBERT, J. A., SARANTOS, M., BENNA, M., SLAVIN, J. A., SCHRIVER, D., TRÁVNÍČEK, P. M., ORLANDO, T. M., SPRAGUE, A. L., BLEWETT, D. T., GILLIS-DAVIS, J. J., FELDMAN, W. C., LAWRENCE, D. J., HO, G. C., EBEL, D. S., NITTLER, L. R., VILAS, F., PIETERS, C. M., SOLOMON, S. C., JOHNSON, C. L., WINSLOW, R. M., HELBERT, J., PELOWSKI, P. N., WEIDER, S. Z., MOUAWAD, N., IZENBERG, N. R. & MCCLINTOCK, W. E. 2014a. Mercury's weather-beaten surface: Understanding mercury in the context of lunar and asteroidal space weathering studies. *Space Science Reviews*, 181, 121-214.
- DOMINGUE, D. L., CHAPMAN, C. R., KILLEN, R. M., ZURBUCHEN, T. H., GILBERT, J. A., SARANTOS, M., BENNA, M., SLAVIN, J. A., SCHRIVER, D., TRÁVNÍČEK, P. M., ORLANDO, T. M., SPRAGUE, A. L., BLEWETT, D. T., GILLIS-DAVIS, J. J., FELDMAN, W. C., LAWRENCE,

- D. J., HO, G. C., EBEL, D. S., NITTLER, L. R., VILAS, F., PIETERS, C. M., SOLOMON, S. C., JOHNSON, C. L., WINSLOW, R. M., HELBERT, J., PEPLOWSKI, P. N., WEIDER, S. Z., MOUAWAD, N., IZENBERG, N. R. & MCCLINTOCK, W. E. 2014b. Mercury's Weather-Beaten Surface: Understanding Mercury in the Context of Lunar and Asteroidal Space Weathering Studies. *Space Science Reviews*, 181, 121-214.
- DOMINGUE, D. L., D'AMORE, M., FERRARI, S., HELBERT, J. & IZENBERG, N. R. 2019a. Analysis of the MESSENGER MASCS photometric targets part I: Photometric standardization for examining spectral variability across Mercury's surface. *Icarus*, 319, 247-263.
- DOMINGUE, D. L., D'AMORE, M., FERRARI, S., HELBERT, J. & IZENBERG, N. R. 2019b. Analysis of the MESSENGER MASCS photometric targets part II: Photometric variability between geomorphological units. *Icarus*, 319, 140-246.
- DOMINGUE, D. L., MURCHIE, S. L., CHABOT, N. L., DENEVI, B. W. & VILAS, F. 2011. Mercury's spectrophotometric properties: Update from the Mercury Dual Imaging System observations during the third MESSENGER flyby. *Planetary and Space Science*, 59, 1853-1872.
- DOMINGUE, D. L., MURCHIE, S. L., DENEVI, B. W., ERNST, C. M. & CHABOT, N. L. 2015. Mercury's global color mosaic: An update from MESSENGER's orbital observations. *Icarus*, 257, 477-488.
- DONALDSON HANNA, K. L., THOMAS, I. R., BOWLES, N. E., GREENHAGEN, B. T., PIETERS, C. M., MUSTARD, J. F., JACKSON, C. R. M. & WYATT, M. B. 2012. Laboratory emissivity measurements of the plagioclase solid solution series under varying environmental conditions. *Journal of Geophysical Research: Planets*, 117.
- EMERY, J. P., SPRAGUE, A. L., WITTEBORN, F. C., COLWELL, J. E., KOZLOWSKI, R. W. H. & WOODEN, D. H. 1998. Mercury: Thermal Modeling and Mid-infrared (5–12 μm) Observations. *Icarus*, 136, 104-123.
- EMERY, W., CAMPS, A. & RODRIGUEZ-CASSOLA, M. 2017. *Introduction to Satellite Remote Sensing: Atmosphere, Ocean, Land and Cryosphere Applications*, Elsevier Science.
- FARMER, V. C. 1974. The Infrared Spectra of Minerals. *Mineralogical Society, London*, Monograph 4.
- FARRAND, W. H., MERÉNYI, E. & PARENTE, M. C. 2019. Hyper-and Multispectral Visible and Near-Infrared Imaging Analysis. *Remote Compositional Analysis: Techniques for Understanding Spectroscopy*, 307-323.
- FERRARI, S., MATURILLI, A., CARLI, C., D'AMORE, M., HELBERT, J., NESTOLA, F. & HIESINGER, H. 2020. Thermal infrared emissivity of felsic-rich to mafic-rich analogues of hot planetary regoliths. *Earth and Planetary Science Letters*, 534, 116089.
- FERRARI, S., NESTOLA, F., MASSIRONI, M., MATURILLI, A., HELBERT, J., ALVARO, M., DOMENEGHETTI, M. C. & ZORZI, F. 2014. In-situ high-temperature emissivity spectra and thermal expansion of C 2/c pyroxenes: implications for the surface of Mercury. *American Mineralogist*, 99, 786-792.
- FISCHER, E. M. & PIETERS, C. M. 1994. Remote determination of exposure degree and iron concentration of lunar soils using VIS-NIR spectroscopic methods. *Icarus*, 111, 475-488.

- FLAMINI, E., CAPACCIONI, F., COLANGELI, L., CREMONESE, G., DORESSOUNDIRAM, A., JOSSET, J. L., LANGEVIN, Y., DEBEL, S., CAPRIA, M. T., DE SANCTIS, M. C., MARINANGELI, L., MASSIRONI, M., MAZZOTTA EPIFANI, E., NALETTO, G., PALUMBO, P., ENG, P., ROIG, J. F., CAPORALI, A., DA DEPPO, V., ERARD, S., FEDERICO, C., FORNI, O., SGAVETTI, M., FILACCHIONE, G., GIACOMINI, L., MARRA, G., MARTELLATO, E., ZUSI, M., COSI, M., BETTANINI, C., CALAMAI, L., ZACCARIOTTO, M., TOMMASI, L., DAMI, M., FICAI VELTRONI, J., POULET, F. & HELLO, Y. 2010. SIMBIO-SYS: The spectrometer and imagers integrated observatory system for the BepiColombo planetary orbiter. *Planetary and Space Science*, 58, 125-143.
- GOGUEN, J. D. 2014. Planetary surface photometry and imaging: progress and perspectives. *Reports on Progress in Physics*, 77, 104901.
- GOLDSTEN, J. O., RHODES, E. A., BOYNTON, W. V., FELDMAN, W. C., LAWRENCE, D. J., TROMBKA, J. I., SMITH, D. M., EVANS, L. G., WHITE, J. & MADDEN, N. W. 2007. The MESSENGER gamma-ray and neutron spectrometer. *The Messenger Mission to Mercury*. Springer.
- GOODFELLOW, I., BENGIO, Y. & COURVILLE, A. 2016. Deep Learning. *MIT Press*.
- GOUDGE, T. A., HEAD, J. W., KERBER, L., BLEWETT, D. T., DENEVI, B. W., DOMINGUE, D. L., GILLIS-DAVIS, J. J., GWINNER, K., HELBERT, J., HOLSCRAW, G. M., IZENBERG, N. R., KLIMA, R. L., MCCLINTOCK, W. E., MURCHIE, S. L., NEUMANN, G. A., SMITH, D. E., STROM, R. G., XIAO, Z., ZUBER, M. T. & SOLOMON, S. C. 2014. Global inventory and characterization of pyroclastic deposits on Mercury: New insights into pyroclastic activity from MESSENGER orbital data. *Journal of Geophysical Research E: Planets*, 119, 635-658.
- GRIFFITHS, P. R. & DE HASETH, J. A. 2007. *Fourier transform infrared spectrometry*, John Wiley & Sons.
- GUANTER, L., BRELL, M., CHAN, J. C. W., GIARDINO, C., GOMEZ-DANS, J., MIELKE, C., MORSDORF, F., SEGL, K. & YOKOYA, N. 2019. Synergies of Spaceborne Imaging Spectroscopy with Other Remote Sensing Approaches. *Surveys in Geophysics*, 40, 657-687.
- HAMILTON, V. E. 2000. Thermal infrared emission spectroscopy of the pyroxene mineral series. *Journal of Geophysical Research: Planets*, 105, 9701-9716.
- HAMILTON, V. E. 2010. Thermal infrared (vibrational) spectroscopy of Mg–Fe olivines: A review and applications to determining the composition of planetary surfaces. *Geochemistry*, 70, 7-33.
- HAPKE, B. 2001. Space weathering from Mercury to the asteroid belt. *Journal of Geophysical Research: Planets*, 106, 10039-10073.
- HAPKE, B. 2012. *Theory of Reflectance and Emittance Spectroscopy*, Cambridge, Cambridge University Press.
- HAPKE, B., DANIELSON JR., G. E., KLAASEN, K. & WILSON, L. 1975. Photometric observations of Mercury from Mariner 10. *Journal of Geophysical Research (1896-1977)*, 80, 2431-2443.

- HARGITAI, H., KERESZTURI, Á. & GILLIS-DAVIS, J. Pit-Floor Crater. *Encyclopedia of Planetary Landforms*, 1-6.
- HARMON, J. K., SLADE, M. A., BUTLER, B. J., HEAD, J. W., RICE, M. S. & CAMPBELL, D. B. 2007. Mercury: Radar images of the equatorial and midlatitude zones. *Icarus*, 187, 374-405.
- HAWKINS, S. E., BOLDT, J. D., DARLINGTON, E. H., ESPIRITU, R., GOLD, R. E., GOTWOLS, B., GREY, M. P., HASH, C. D., HAYES, J. R. & JASKULEK, S. E. 2007. The Mercury dual imaging system on the MESSENGER spacecraft. *Space Science Reviews*, 131, 247-338.
- HELBERT, J., DYAR, D., MATURILLI, A., WIDEMANN, T., MARCQ, E., ROSAS-ORTIZ, Y., WALTER, I., D'AMORE, M., ALEMANNI, G., MUELLER, N. & SMREKAR, S. 2019. Spectroscopy of the Surface of Venus - in the Laboratory and from Orbit. *EPSC-DPS Joint Meeting 2019*.
- HELBERT, J., HIESINGER, H., WALTER, I., SÄUBERLICH, T., MATURILLI, A., D'AMORE, M., KNOLLENBERG, J., LORENZ, E., PETER, G. & ARNOLD, G. 2010. *MERTIS: understanding Mercury's surface composition from mid-infrared spectroscopy*, SPIE.
- HELBERT, J. & MATURILLI, A. 2009. The emissivity of a fine-grained labradorite sample at typical Mercury dayside temperatures. *Earth and Planetary Science Letters*, 285, 347-354.
- HELBERT, J., MATURILLI, A. & D'AMORE, M. 2013a. Visible and near-infrared reflectance spectra of thermally processed synthetic sulfides as a potential analog for the hollow forming materials on Mercury. *Earth and Planetary Science Letters*, 369–370, 233-238.
- HELBERT, J., MATURILLI, A., DYAR, M., FERRARI, S., MÜLLER, N. & SMREKAR, S. 2018. Orbital spectroscopy of the surface of Venus. *LPI*, 1219.
- HELBERT, J., MOROZ, L. V., MATURILLI, A., BISCHOFF, A., WARELL, J., SPRAGUE, A. & PALOMBA, E. 2007. A set of laboratory analogue materials for the MERTIS instrument on the ESA BepiColombo mission to Mercury. *Advances in Space Research*, 40, 272-279.
- HELBERT, J., NESTOLA, F., FERRARI, S., MATURILLI, A., MASSIRONI, M., REDHAMMER, G. J., CAPRIA, M. T., CARLI, C., CAPACCIONI, F. & BRUNO, M. 2013b. Olivine thermal emissivity under extreme temperature ranges: Implication for Mercury surface. *Earth and Planetary Science Letters*, 371–372, 252-257.
- HENDRIX, A. R., RETHERFORD, K. D., RANDALL GLADSTONE, G., HURLEY, D. M., FELDMAN, P. D., EGAN, A. F., KAUFMANN, D. E., MILES, P. F., PARKER, J. W., HORVATH, D., ROJAS, P. M., VERSTEEG, M. H., DAVIS, M. W., GREATHOUSE, T. K., MUKHERJEE, J., STEFFL, A. J., PRYOR, W. R. & STERN, S. A. 2012. The lunar far-UV albedo: Indicator of hydration and weathering. *Journal of Geophysical Research: Planets*, 117.
- HENDRIX, A. R., VILAS, F. & LI, J.-Y. 2016. The UV signature of carbon in the solar system. *Meteoritics & Planetary Science*, 51, 105-115.
- HERRICK, R. R., BATEMAN, E. M., CRUMPACKER, W. G. & BATES, D. 2018. Observations From a Global Database of Impact Craters on Mercury With Diameters Greater than 5 km. *Journal of Geophysical Research: Planets*, 123, 2089-2109.
- HIESINGER, H., HELBERT, J., ALEMANNI, G., BAUCH, K. E., D'AMORE, M., MATURILLI, A., MORLOK, A., REITZE, M. P., STANGARONE, C., STOJIC, A. N., VARATHARAJAN, I., WEBER, I. & THE, M. C.-I. T. 2020. Studying the Composition and Mineralogy of the

- Hermean Surface with the Mercury Radiometer and Thermal Infrared Spectrometer (MERTIS) for the BepiColombo Mission: An Update. *Space Science Reviews*, 216, 110.
- HIESINGER, H., HELBERT, J. & MERTIS CO-I TEAM 2010. The Mercury Radiometer and Thermal Infrared Spectrometer (MERTIS) for the BepiColombo mission. *Planetary and Space Science*, 58, 144-165.
- HOLSCLAW, G. M., MCCLINTOCK, W. E., DOMINGUE, D. L., IZENBERG, N. R., BLEWETT, D. T. & SPRAGUE, A. L. 2010. A comparison of the ultraviolet to near-infrared spectral properties of Mercury and the Moon as observed by MESSENGER. *Icarus*, 209, 179-194.
- HOOD, L. L. 2016. Magnetic anomalies concentrated near and within Mercury's impact basins: Early mapping and interpretation. *Journal of Geophysical Research: Planets*, 121, 1016-1025.
- HORGAN, B. H. N., CLOUTIS, E. A., MANN, P. & BELL III, J. F. 2014. Near-infrared spectra of ferrous mineral mixtures and methods for their identification in planetary surface spectra. *Icarus*, 234, 132-154.
- HSU, C.-P. S. 1997. Infrared spectroscopy. *Handbook of instrumental techniques for analytical chemistry*, 249.
- INSTRUMENT-USER-MANUAL 2013. BepiColombo MERTIS - Instrument User Manual (FM)". *German Aerospace Center*, , MER-DLR-MA-001, Issue 1, Revision 3.
- IZENBERG, N. R., KLIMA, R. L., MURCHIE, S. L., BLEWETT, D. T., HOLSCLAW, G. M., MCCLINTOCK, W. E., MALARET, E., MAUCERI, C., VILAS, F., SPRAGUE, A. L., HELBERT, J., DOMINGUE, D. L., HEAD III, J. W., GOUDGE, T. A., SOLOMON, S. C., HIBBITTS, C. A. & DYAR, M. D. 2014. The low-iron, reduced surface of Mercury as seen in spectral reflectance by MESSENGER. *Icarus*, 228, 364-374.
- JOLLIFFE, I. 2011. Principal Component Analysis. In: LOVRIC, M. (ed.) *International Encyclopedia of Statistical Science*. Berlin, Heidelberg: Springer Berlin Heidelberg.
- JOZWIAK, L. M., HEAD, J. W. & WILSON, L. 2018. Explosive volcanism on Mercury: Analysis of vent and deposit morphology and modes of eruption. *Icarus*, 302, 191-212.
- KERBER, L., HEAD, J. W., BLEWETT, D. T., SOLOMON, S. C., WILSON, L., MURCHIE, S. L., ROBINSON, M. S., DENEVI, B. W. & DOMINGUE, D. L. 2011. The global distribution of pyroclastic deposits on Mercury: The view from MESSENGER flybys 1–3. *Planetary and Space Science*, 59, 1895-1909.
- KERBER, L., HEAD, J. W., SOLOMON, S. C., MURCHIE, S. L., BLEWETT, D. T. & WILSON, L. 2009. Explosive volcanic eruptions on Mercury: Eruption conditions, magma volatile content, and implications for interior volatile abundances. *Earth and Planetary Science Letters*, 285, 263-271.
- KINCZYK, M. J., PROCKTER, L. M., CHAPMAN, C. R., SUSORNEY, H. C. M. & . 2016. A Morphological Evaluation of Crater Degradation on Mercury: Revisiting Crater Classification with MESSENGER Data. *47th Lunar and Planetary Science Conference*, #1573.

- KLIMA, R. L., DENEVI, B. W., ERNST, C. M., MURCHIE, S. L. & PEPLOWSKI, P. N. 2018. Global Distribution and Spectral Properties of Low-Reflectance Material on Mercury. *Geophysical Research Letters*, 45, 2945-2953.
- KOIKE, C., CHIHARA, H., TSUCHIYAMA, A., SUTO, H., SOGAWA, H. & OKUDA, H. 2003. Compositional dependence of infrared absorption spectra of crystalline silicate. *A&A*, 399, 1101-1107.
- KOIKE, C., MUTSCHKE, H., SUTO, H., NAOI, T., CHIHARA, H., HENNING, T., JÄGER, C., TSUCHIYAMA, A., DORSCHNER, J. & OKUDA, H. 2006. Temperature effects on the mid- and far-infrared spectra of olivine particles. *A&A*, 449, 583-596.
- KROTIKOV, V. & SHCHUKO, O. 1975a. Thermal conditions in the surface layer of Mercury. *Soviet Astronomy*, 19, 86-89.
- KROTIKOV, V. D. & SHCHUKO, O. B. 1975b. Thermal conditions in the surface layer of Mercury. *Astronomicheskii Zhurnal*, 52, 146.
- LANE, M., ALLAIN, J., CLARK, R., CLOUTIS, E., DYAR, M., HELBERT, J., HENDRIX, A., HOLSCLAW, G., OSTERLOO, M. & PEARSON, N. 2018. Toolbox for Research and Exploration (TRES): The Fine-Particle Spectral Library. *LPI*, 1098.
- LANE, M. D. & BISHOP, J. L. 2019. Mid-infrared (Thermal) Emission and Reflectance Spectroscopy: Laboratory Spectra of Geologic Materials. In: BELL III, J. F., BISHOP, J. L. & MOERSCH, J. E. (eds.) *Remote Compositional Analysis: Techniques for Understanding Spectroscopy, Mineralogy, and Geochemistry of Planetary Surfaces*. Cambridge: Cambridge University Press.
- LAWRENCE, D. J., PEPLOWSKI, P. N., BECK, A. W., FELDMAN, W. C., FRANK, E. A., MCCOY, T. J., NITTLER, L. R. & SOLOMON, S. C. 2017. Compositional terranes on Mercury: Information from fast neutrons. *Icarus*, 281, 32-45.
- LEWIS, J. S. 1988. Origin and composition of Mercury. *Mercury*, University of Arizona Press.
- LOGAN, L. M., HUNT, G. R., SALISBURY, J. W. & BALSAMO, S. R. 1973. Compositional implications of Christiansen frequency maximums for infrared remote sensing applications. *Journal of Geophysical Research (1896-1977)*, 78, 4983-5003.
- LUCCHETTI, A., PAJOLA, M., GALLUZZI, V., GIACOMINI, L., CARLI, C., CREMONESE, G., MARZO, G. A., FERRARI, S., MASSIRONI, M. & PALUMBO, P. 2018. Mercury Hollows as Remnants of Original Bedrock Materials and Devolatilization Processes: A Spectral Clustering and Geomorphological Analysis. *Journal of Geophysical Research: Planets*, 123, 2365-2379.
- LUCEY, P. G. & RINER, M. A. 2011. The optical effects of small iron particles that darken but do not redden: Evidence of intense space weathering on Mercury. *Icarus*, 212, 451-462.
- LYON, R. J. P. 1965. Analysis of rocks by spectral infrared emission (8 to 25 microns). *Economic Geology*, 60, 715-736.
- MACQUEEN, J. Some methods for classification and analysis of multivariate observations. Proceedings of the Fifth Berkeley Symposium on Mathematical Statistics and Probability, Volume 1: Statistics, 1967 1967 Berkeley, Calif.: University of California Press, 281-297.
- MAHONEY, T. J. 2014. Mercury: An Overview. In: MAHONEY, T. J. (ed.) *Mercury*. New York, NY: Springer New York.

- MANCINELLI, P., MINELLI, F., MONDINI, A., PAUSELLI, C. & FEDERICO, C. 2015. A downscaling approach for geological characterization of the Raditladi basin of Mercury. *Geological Society, London, Special Publications*, 401, 57-75.
- MARCHI, S., MASSIRONI, M., CREMONESE, G., MARTELLATO, E., GIACOMINI, L. & PROCKTER, L. 2011. The effects of the target material properties and layering on the crater chronology: The case of Raditladi and Rachmaninoff basins on Mercury. *Planetary and Space Science*, 59, 1968-1980.
- MATURILLI, A., DONALDSON HANNA, K. L., HELBERT, J. R. & PIETERS, C. A New Standard for Calibration of High Temperature Emissivity: Laboratory Intercalibration at PEL of DLR and ALEC of Brown University. LPSC 2013, 2013/03/01/ 2013.
- MATURILLI, A. & HELBERT, J. 2014. Characterization, testing, calibration, and validation of the Berlin emissivity database. *Journal of Applied Remote Sensing*, 8, 084985.
- MATURILLI, A., HELBERT, J., AMORE, M. D., VARATHARAJAN, I., HIESINGER, H. & BAUCH, K. 2018a. *The operations plan for the MErcury Radiometer and Thermal infrared Imaging Spectrometer (MERTIS) on its way to Mercury*, SPIE.
- MATURILLI, A., HELBERT, J., AMORE, M. D., VARATHARAJAN, I. & ORTIZ, Y. R. 2018b. *The Planetary Spectroscopy Laboratory (PSL): wide spectral range, wider sample temperature range*, SPIE.
- MATURILLI, A., HELBERT, J., D'AMORE, M., VARATHARAJAN, I. & ORTIZ, Y. R. 2018c. *The Planetary Spectroscopy Laboratory (PSL): wide spectral range, wider sample temperature range*, SPIE.
- MATURILLI, A., HELBERT, J., FERRARI, S. & D'AMORE, M. 2016a. On the effect of emergence angle on emissivity spectra: application to small bodies. *Earth, Planets and Space*, 68, 84.
- MATURILLI, A., HELBERT, J., FERRARI, S., DAVIDSSON, B. & D'AMORE, M. 2016b. Characterization of asteroid analogues by means of emission and reflectance spectroscopy in the 1- to 100- μ m spectral range. *Earth, Planets and Space*, 68, 113.
- MATURILLI, A., HELBERT, J. & MOROZ, L. 2008. The Berlin emissivity database (BED). *Planetary and Space Science*, 56, 420-425.
- MATURILLI, A., HELBERT, J., ST. JOHN, J. M., HEAD III, J. W., VAUGHAN, W. M., D'AMORE, M., GOTTSCHALK, M. & FERRARI, S. 2014. Komatiites as Mercury surface analogues: Spectral measurements at PEL. *Earth and Planetary Science Letters*, 398, 58-65.
- MATURILLI, A., HELBERT, J. & VARATHARAJAN, I. 2019. Graphite as Potential Darkening Agent for Mercury: Spectral Measurements Under Simulated Mercury Conditions. *Lunar and Planetary Science Conference*.
- MATURILLI, A., HELBERT, J., VARATHARAJAN, I. & HIESINGER, H. 2017a. Emissivity Spectra of Analogue Materials at Mercury P-T Conditions. *48th Lunar and Planetary Science Conference*. Houston: Lunar and Planetary Institute.
- MATURILLI, A., HELBERT, J., VARATHARAJAN, I. & HIESINGER, H. 2017b. Emissivity Spectra Of Analogue Materials At Mercury T-P Conditions. *48th Lunar and Planetary Science Conference*, 1427.

- MATURILLI, A., HELBERT, J., WITZKE, A. & MOROZ, L. 2006. Emissivity measurements of analogue materials for the interpretation of data from PFS on Mars Express and MERTIS on Bepi-Colombo. *Planetary and Space Science*, 54, 1057-1064.
- MATURILLI, A., HELBERT, J., VARATHARAJAN, I. & HIESINGER, H. 2017. Emissivity Spectra Of Analogue Materials At Mercury T-P Conditions. *48th Lunar and Planetary Science Conference*, 1427.
- MCCLINTOCK, W. E., IZENBERG, N. R., HOLSCLAW, G. M., BLEWETT, D. T., DOMINGUE, D. L., HEAD, J. W., HELBERT, J., MCCOY, T. J., MURCHIE, S. L., ROBINSON, M. S., SOLOMON, S. C., SPRAGUE, A. L. & VILAS, F. 2008. Spectroscopic Observations of Mercury's Surface Reflectance during MESSENGER's First Mercury Flyby. *Science*, 321, 62-65.
- MCCLINTOCK, W. E. & LANKTON, M. R. 2007. The Mercury Atmospheric and Surface Composition Spectrometer for the MESSENGER Mission. *Space Science Reviews*, 131, 481-521.
- MCCORD, T. B. & CLARK, R. N. 1979. The Mercury soil: Presence of Fe²⁺. *Journal of Geophysical Research: Solid Earth*, 84, 7664-7668.
- MCKELVY, M. J., CLAUNSINGER, W. S. & OUVRARD, G. 2007. Titanium Disulfide. *Inorganic Syntheses*.
- MORIMOTO, N. 1988. Nomenclature of Pyroxenes. *Mineralogy and Petrology*, 39, 55-76.
- MURCHIE, S. L., IZENBERG, N. R. & KLIMA, R. L. 2019. Spectral Analyses of Mercury. In: BELL III, J. F., BISHOP, J. L. & MOERSCH, J. E. (eds.) *Remote Compositional Analysis: Techniques for Understanding Spectroscopy, Mineralogy, and Geochemistry of Planetary Surfaces*. Cambridge: Cambridge University Press.
- MURCHIE, S. L., KLIMA, R. L., DENEVI, B. W., ERNST, C. M., KELLER, M. R., DOMINGUE, D. L., BLEWETT, D. T., CHABOT, N. L., HASH, C. D. & MALARET, E. 2015. Orbital multispectral mapping of Mercury with the MESSENGER Mercury Dual Imaging System: Evidence for the origins of plains units and low-reflectance material. *Icarus*, 254, 287-305.
- MURCHIE, S. L., WATTERS, T. R., ROBINSON, M. S., HEAD, J. W., STROM, R. G., CHAPMAN, C. R., SOLOMON, S. C., MCCLINTOCK, W. E., PROCKTER, L. M., DOMINGUE, D. L. & BLEWETT, D. T. 2008. Geology of the Caloris Basin, Mercury: A View from MESSENGER. *Science*, 321, 73-76.
- MUSTARD, J. F. & GLOTCH, T. D. 2019. Theory of Reflectance and Emittance Spectroscopy of Geologic Materials in the Visible and Infrared Regions. *Remote Compositional Analysis: Techniques for Understanding Spectroscopy*, 21-41.
- MUSTARD, J. F. & PIETERS, C. M. 1989. Photometric phase functions of common geologic minerals and applications to quantitative analysis of mineral mixture reflectance spectra. *Journal of Geophysical Research: Solid Earth*, 94, 13619-13634.
- NAMUR, O. & CHARLIER, B. 2017. Silicate mineralogy at the surface of Mercury. *Nature Geosci*, 10, 9-13.
- NAMUR, O., CHARLIER, B., HOLTZ, F., CARTIER, C. & MCCAMMON, C. 2016. Sulfur solubility in reduced mafic silicate melts: Implications for the speciation and distribution of sulfur on Mercury. *Earth and Planetary Science Letters*, 448, 102-114.

- NITTLER, L. R., STARR, R. D., WEIDER, S. Z., MCCOY, T. J., BOYNTON, W. V., EBEL, D. S., ERNST, C. M., EVANS, L. G., GOLDSTEN, J. O., HAMARA, D. K., LAWRENCE, D. J., MCNUTT, R. L., SCHLEMM, C. E., SOLOMON, S. C. & SPRAGUE, A. L. 2011. The Major-Element Composition of Mercury's Surface from MESSENGER X-ray Spectrometry. *Science*, 333, 1847-1850.
- OKIN, G. S. & PAINTER, T. H. 2004. Effect of grain size on remotely sensed spectral reflectance of sandy desert surfaces. *Remote Sensing of Environment*, 89, 272-280.
- PEPLOWSKI, P. N., KLIMA, R. L., LAWRENCE, D. J., ERNST, C. M., DENEVI, B. W., FRANK, E. A., GOLDSTEN, J. O., MURCHIE, S. L., NITTLER, L. R. & SOLOMON, S. C. 2016. Remote sensing evidence for an ancient carbon-bearing crust on Mercury. *Nature Geoscience*, 9, 273.
- PEPLOWSKI, P. N., LAWRENCE, D. J., FELDMAN, W. C., GOLDSTEN, J. O., BAZELL, D., EVANS, L. G., HEAD, J. W., NITTLER, L. R., SOLOMON, S. C. & WEIDER, S. Z. 2015. Geochemical terranes of Mercury's northern hemisphere as revealed by MESSENGER neutron measurements. *Icarus*, 253, 346-363.
- PÉREZ-JUSTE, I. & FAZA, O. N. 2015. Interaction of radiation with matter. *Structure Elucidation in Organic Chemistry*.
- PETER, G., HELBERT, J., HIESINGER, H., WEBER, I., WALTER, I., ARNOLD, G. & SÄÜBERLICH, T. Developing of MERTIS as an advanced process from the study up to the flight model. Infrared Remote Sensing and Instrumentation XXI, 2013. International Society for Optics and Photonics, 886707.
- PIETERS, C. M. & ENGLERT, P. A. J. 1993. *Remote Geochemical Analysis, Elemental and Mineralogical Composition*.
- PIETERS, C. M., FISCHER, E. M., RODE, O. & BASU, A. 1993. Optical effects of space weathering: The role of the finest fraction. *Journal of Geophysical Research: Planets*, 98, 20817-20824.
- REITZE, M., MORLOK, A., HIESINGER, H., WEBER, I. & STOJIC, A. 2017. Infrared spectroscopy of Mercury analogue materials under simulated Mercury surface temperature conditions.
- REITZE, M. P., WEBER, I., KROLL, H., MORLOK, A., HIESINGER, H. & HELBERT, J. 2020. Mid-infrared spectroscopy of alkali feldspar samples for space application. *Mineralogy and Petrology*, 114, 453-463.
- ROBINSON, M. S. & LUCEY, P. G. 1997. Recalibrated Mariner 10 color mosaics: Implications for mercurian volcanism. *Science*, 275, 197-200.
- ROBINSON, M. S., MURCHIE, S. L., BLEWETT, D. T., DOMINGUE, D. L., HAWKINS, S. E., HEAD, J. W., HOLSCLAW, G. M., MCCLINTOCK, W. E., MCCOY, T. J., MCNUTT, R. L., PROCKTER, L. M., SOLOMON, S. C. & WATTERS, T. R. 2008. Reflectance and Color Variations on Mercury: Regolith Processes and Compositional Heterogeneity. *Science*, 321, 66-69.
- ROSAS ORTIZ, Y., HELBERT, J., MATORILLI, A. & LEHMANN, M. 2018. A Compact Planetary Simulation Chamber for the Characterization of the Bi-Directional Reflectance of Asteroid, Cometary, and Solar System Small Bodies (SSSB) Analogues at Low-Temperature Environments. *LPI*, 1883.

- ROTHERY, D. A., MASSIRONI, M., ALEMANNI, G., BARRAUD, O., BESSE, S., BOTT, N., BRUNETTO, R., BUNCE, E., BYRNE, P., CAPACCIONI, F., CAPRIA, M. T., CARLI, C., CHARLIER, B., CORNET, T., CREMONESE, G., D'AMORE, M., DE SANCTIS, M. C., DORESSOUNDIRAM, A., FERRANTI, L., FILACCHIONE, G., GALLUZZI, V., GIACOMINI, L., GRANDE, M., GUZZETTA, L. G., HELBERT, J., HEYNER, D., HIESINGER, H., HUSSMANN, H., HYODO, R., KOHOUT, T., KOZYREV, A., LITVAK, M., LUCCHETTI, A., MALAKHOV, A., MALLIBAND, C., MANCINELLI, P., MARTIKAINEN, J., MARTINDALE, A., MATURILLI, A., MILILLO, A., MITROFANOV, I., MOKROUSOV, M., MORLOK, A., MUINONEN, K., NAMUR, O., OWENS, A., NITTLER, L. R., OLIVEIRA, J. S., PALUMBO, P., PAJOLA, M., PEGG, D. L., PENTTILÄ, A., POLITI, R., QUARATI, F., RE, C., SANIN, A., SCHULZ, R., STANGARONE, C., STOJIC, A., TRETIVAKOV, V., VÄISÄNEN, T., VARATHARAJAN, I., WEBER, I., WRIGHT, J., WURZ, P. & ZAMBON, F. 2020. Rationale for BepiColombo Studies of Mercury's Surface and Composition. *Space Science Reviews*, 216, 66.
- SALISBURY, J. W., D'ARIA, D. M. & JAROSEWICH, E. 1991. Midinfrared (2.5–13.5 μm) reflectance spectra of powdered stony meteorites. *Icarus*, 92, 280-297.
- SALISBURY, J. W., WALTER, L. S., VERGO, N. & D'ARIA, D. 1987. Mid-infrared (2.1-25 μm) spectra of minerals. U.S. Geological Survey Open File Report 87-263. Reston.
- SCHLEMM, C. E., STARR, R. D., HO, G. C., BECHTOLD, K. E., HAMILTON, S. A., BOLDT, J. D., BOYNTON, W. V., BRADLEY, W., FRAEMAN, M. E. & GOLD, R. E. 2007. The X-Ray Spectrometer on the MESSENGER spacecraft. *The Messenger Mission to Mercury*. Springer.
- SHAKUN, A., KORABLEV, O., MOSHKIN, B., GRIGORIEV, A., IGNATIEV, N., MASLOV, I., SAZONOV, O., PATSAEV, D., KUNGUROV, A. & SANTOS-SKRIPKO, A. 2017. Fourier Transform Spectrometers for remote sensing of planetary atmospheres and surfaces. *CEAS Space Journal*, 9, 399-409.
- SHEVCHENKO, V. V. 2002. The Structure of the Surface of Mercury's Regolith from Remote Sensing Data. *Solar System Research*, 36, 359-366.
- SHIRLEY, J. H. & FAIRBRIDGE, R. W. 1997. *Encyclopedia of planetary sciences*.
- SOLOMON, S. C., MCNUTT, R. L., GOLD, R. E., ACUÑA, M. H., BAKER, D. N., BOYNTON, W. V., CHAPMAN, C. R., CHENG, A. F., GLOECKLER, G., HEAD III, J. W., KRIMIGIS, S. M., MCCLINTOCK, W. E., MURCHIE, S. L., PEALE, S. J., PHILLIPS, R. J., ROBINSON, M. S., SLAVIN, J. A., SMITH, D. E., STROM, R. G., TROMBKA, J. I. & ZUBER, M. T. 2001. The MESSENGER mission to Mercury: scientific objectives and implementation. *Planetary and Space Science*, 49, 1445-1465.
- SOTER, S. & ULRICHS, J. 1967. Rotation and Heating of the Planet Mercury. *Nature*, 214, 1315-1316.
- SPRAGUE, A. L., DEUTSCH, L. K., HORA, J., FAZIO, G. G., LUDWIG, B., EMERY, J. & HOFFMANN, W. F. 2000. Mid-infrared (8.1–12.5 μm) imaging of Mercury. *Icarus*, 147, 421-432.
- SPRAGUE, A. L., DONALDSON HANNA, K. L., KOZLOWSKI, R. W. H., HELBERT, J., MATURILLI, A., WARELL, J. B. & HORA, J. L. 2009. Spectral emissivity measurements of Mercury's surface indicate Mg- and Ca-rich mineralogy, K-spar, Na-rich plagioclase, rutile, with possible perovskite, and garnet. *Planetary and Space Science*, 57, 364-383.

- SPRAGUE, A. L., EMERY, J. P., DONALDSON, K. L., RUSSELL, R. W., LYNCH, D. K. & MAZUK, A. L. 2002. Mercury: Mid-infrared (3–13.5 μm) observations show heterogeneous composition, presence of intermediate and basic soil types, and pyroxene. *Meteoritics & Planetary Science*, 37, 1255-1268.
- SPRAGUE, A. L., HUNTEN, D. M. & LODDERS, K. 1995. Sulfur at Mercury, Elemental at the Poles and Sulfides in the Regolith. *Icarus*, 118, 211-215.
- SPRAGUE, A. L., KOZLOWSKI, R. W. H., WITTEBORN, F. C., CRUIKSHANK, D. P. & WOODEN, D. H. 1994. Mercury: Evidence for anorthosite and basalt from mid-infrared (7.3-13.5 μm) spectroscopy. *Icarus*, 109, 156-167.
- SPRAGUE, A. L., NASH, D. B., WITTEBORN, F. C. & CRUIKSHANK, D. P. 1997. Mercury's feldspar connection mid-IR measurements suggest plagioclase. *Advances in Space Research*, 19, 1507-1510.
- SPUDIS, P. D. & GUEST, J. E. 1988. Stratigraphy and geologic history of Mercury. *Mercury*, 118-164.
- STANGARONE, C. 2017. *Ab initio calculations of Raman and IR spectra of orthoenstatite and forsterite: lattice dynamics and modelling for planetary remote sensing*. Universita'degli studi di Parma. Dipartimento di Fisica e Scienze della
- STANGARONE, C., HELBERT, J., MATURILLI, A., TRIBAUDINO, M. & PRENCIPE, M. 2017. Modelling of thermal-IR spectra of forsterite: application on remote sensing for Mercury. *European Planetary Science Congress*, 11.
- STROM, R. G. & SPRAGUE, A. L. 2003. *Exploring Mercury: the iron planet*, Springer Science & Business Media.
- TAYLOR, L. A., PIETERS, C. M., KELLER, L. P., MORRIS, R. V. & MCKAY, D. S. 2001. Lunar mare soils: Space weathering and the major effects of surface-correlated nanophase Fe. *Journal of Geophysical Research: Planets*, 106, 27985-27999.
- THOMAS, R. J., ROTHERY, D. A., CONWAY, S. J. & ANAND, M. 2014a. Hollows on Mercury: Materials and mechanisms involved in their formation. *Icarus*, 229, 221-235.
- THOMAS, R. J., ROTHERY, D. A., CONWAY, S. J. & ANAND, M. 2014b. Long-lived explosive volcanism on Mercury. *Geophysical Research Letters*, 41, 6084-6092.
- TRANG, D., LUCEY, P. G. & IZENBERG, N. R. 2017. Radiative transfer modeling of MESSENGER VIRS spectra: Detection and mapping of submicroscopic iron and carbon. *Icarus*, 293, 206-217.
- VANDER KAADEN, K. E., M. MCCUBBIN, F., R. NITTLER, L., N. PEPLOWSKI, P., Z. WEIDER, S., A. FRANK, E. & J. MCCOY, T. 2017. Geochemistry, mineralogy, and petrology of boninitic and komatiitic rocks on the mercurian surface: Insights into the mercurian mantle. *Icarus*, 285, 155-168.
- VARATHARAJAN, I., D'AMORE, M., DOMINGUE, D., HELBERT, J. & MATURILLI, A. 2020a. Global Multivariate Spectral Analysis of Mercury and the Identification of Geochemical Terrains: Derived from the MASCS Spectrometer onboard NASA's MESSENGER Mission. *Earth and Space Science Open Archive*. <https://doi.org/10.1002/essoar.10501760.1>.

- VARATHARAJAN, I., D'AMORE, M., MATURILLI, A., HELBERT, J. & HIESINGER, H. Machine Learning Approach to Deconvolution of Mid-Infrared Telescope Spectra of Mercury: Supporting MERTIS onboard ESA/JAXA BepiColombo mission. AGU Fall Meeting Abstracts, 2018/12/01/ 2018. P41D-3762.
- VARATHARAJAN, I., MATURILLI, A., HELBERT, J., ALEMANNI, G. & HIESINGER, H. 2019a. Spectral behavior of sulfides in simulated daytime surface conditions of Mercury: Supporting past (MESSENGER) and future missions (BepiColombo). *Earth and Planetary Science Letters*, 520, 127-140.
- VARATHARAJAN, I., MATURILLI, A., SIVARAMAN, B., HELBERT, J., GROTT, M., MEKA, J. K., VIJAYAN, S. & BHARDWAJ, A. 2019b. Phase Angle Dependent Ultraviolet to Far-Infrared (0.25-100 μm) Reflectance Spectroscopy of Mukundpura (CM2) Meteorite: Potential analogue of (162173) Ryugu and (101955) Bennu. *Earth and Space Science Open Archive*.
- VARATHARAJAN, I., STANGARONE, C., MATURILLI, A., HELBERT, J. & HIESINGER, H. 2020b. Emissivity of Powdered Silicates in TIR Spectral Range (7-14 μm) Under Simulated Daytime Surface Conditions of Mercury and Their Detection from the Orbit. *LPI*, 1962.
- VARATHARAJAN, I., TSANG, C., WOHLFARTH, K., WÖHLER, C., IZENBERG, N. & HELBERT, J. 2019c. Surface Composition of Mercury from NIR (0.7-4.2 μm) Ground-Based IRTF/SpeX Spectroscopy. *Earth and Planetary Science Congress (EPSC)*, 1331-2.
- VASAVADA, A. R., PAIGE, D. A. & WOOD, S. E. 1999. Near-Surface Temperatures on Mercury and the Moon and the Stability of Polar Ice Deposits. *Icarus*, 141, 179-193.
- VAUGHAN, W. M. H., J. W.; PARMAN, S. W.; HELBERT, J. 2013. What Sulfides Exist on Mercury? *44th Lunar and Planetary Science Conference 2013*.
- VERNAZZA, P., DEMEO, F., NEDELCO, D. A., BIRLAN, M., DORESSOUNDIRAM, A., ERARD, S. & VOLQUARSEN, E. 2010. Resolved spectroscopy of Mercury in the near-IR with SpeX/IRTF. *Icarus*, 209, 125-137.
- VILAS, F., DOMINGUE, D. L., HELBERT, J., D'AMORE, M., MATURILLI, A., KLIMA, R. L., STOCKSTILL-CAHILL, K. R., MURCHIE, S. L., IZENBERG, N. R., BLEWETT, D. T., VAUGHAN, W. M. & HEAD, J. W. 2016. Mineralogical indicators of Mercury's hollows composition in MESSENGER color observations. *Geophysical Research Letters*, 43, 1450-1456.
- VILAS, F., LEAKE, M. A. & MENDELL, W. W. 1984. The dependence of reflectance spectra of Mercury on surface terrain. *Icarus*, 59, 60-68.
- VILAS, F. & MCCORD, T. B. 1976. Mercury: Spectral reflectance measurements (0.33–1.06 μm) 1974/1975. *Icarus*, 28, 593-599.
- WALTER, I., ZEH, T., HELBERT, J., HIESINGER, H., GEBHARDT, A., HIRSCH, H., KNOLLENBERG, J., KESSLER, E., RATAJ, M. & HABERMEIER, J. Deep space instrument design for thermal infrared imaging with MERTIS. *Infrared Remote Sensing and Instrumentation XIX*, 2011. International Society for Optics and Photonics, 81540Y.
- WARELL, J., R.W. KOZLOWSKI, A.L. SPRAGUE, J. HELBERT, A. ÖNEHAG, G. TROUT & ROTHERY, D. 2009. Ground-Based Infrared Spectroscopy of Mercury's Near-Global Surface With IRTF/SpeX: Complementing MESSENGER Compositional Observations. *40th Lunar and Planetary Science Conference*, Abstract #1931.

- WATTERS, T. R., HEAD, J. W., SOLOMON, S. C., ROBINSON, M. S., CHAPMAN, C. R., DENEVI, B. W., FASSETT, C. I., MURCHIE, S. L. & STROM, R. G. 2009. Evolution of the Rembrandt Impact Basin on Mercury. *Science*, 324, 618-621.
- WEIDER, S. Z., NITTLER, L. R., MURCHIE, S. L., PEPOWSKI, P. N., MCCOY, T. J., KERBER, L., KLIMCZAK, C., ERNST, C. M., GOUDGE, T. A., STARR, R. D., IZENBERG, N. R., KLIMA, R. L. & SOLOMON, S. C. 2016. Evidence from MESSENGER for sulfur- and carbon-driven explosive volcanism on Mercury. *Geophysical Research Letters*, 43, 3653-3661.
- WEIDER, S. Z., NITTLER, L. R., STARR, R. D., CRAPSTER-PREGONT, E. J., PEPOWSKI, P. N., DENEVI, B. W., HEAD, J. W., BYRNE, P. K., HAUCK, S. A., EBEL, D. S. & SOLOMON, S. C. 2015. Evidence for geochemical terranes on Mercury: Global mapping of major elements with MESSENGER's X-Ray Spectrometer. *Earth and Planetary Science Letters*, 416, 109-120.
- WEIDER, S. Z., NITTLER, L. R., STARR, R. D., MCCOY, T. J. & SOLOMON, S. C. 2014. Variations in the abundance of iron on Mercury's surface from MESSENGER X-Ray Spectrometer observations. *Icarus*, 235, 170-186.
- WEIDER, S. Z., NITTLER, L. R., STARR, R. D., MCCOY, T. J., STOCKSTILL-CAHILL, K. R., BYRNE, P. K., DENEVI, B. W., HEAD, J. W. & SOLOMON, S. C. 2012. Chemical heterogeneity on Mercury's surface revealed by the MESSENGER X-Ray Spectrometer. *Journal of Geophysical Research: Planets*, 117.
- WHITTEN, J. L. & HEAD, J. W. 2015. Rembrandt impact basin: Distinguishing between volcanic and impact-produced plains on Mercury. *Icarus*, 258, 350-365.
- WU, B., DI, K., OBERST, J. & KARACHEVTSEVA, I. 2018. *Planetary remote sensing and mapping*, CRC Press.
- XIAO, Z., STROM, R. G., BLEWETT, D. T., BYRNE, P. K., SOLOMON, S. C., MURCHIE, S. L., SPRAGUE, A. L., DOMINGUE, D. L. & HELBERT, J. 2013. Dark spots on Mercury: A distinctive low-reflectance material and its relation to hollows. *Journal of Geophysical Research: Planets*, 118, 1752-1765.
- YANG, Y., LI, S., MILLIKEN, R. E., ZHANG, H., ROBERTSON, K. & HIROI, T. 2019. Phase Functions of Typical Lunar Surface Minerals Derived for the Hapke Model and Implications for Visible to Near-Infrared Spectral Unmixing. *Journal of Geophysical Research: Planets*, 124, 31-60.
- ZEH, T., GAL, C., KAISER, S., PETER, G., WALTER, I., HELBERT, J., JACHLEWSKI, J., MULTHAUP, K. & HIESINGER, H. MERTIS: reflective baffle design and manufacturing. *Infrared Remote Sensing and Instrumentation XVIII*, 2010. International Society for Optics and Photonics, 780800.

The path from dreams to success does exist. May you have the vision to find it, the courage to get on to it, and the perseverance to follow it.

Astronaut Dr Kalpana Chawla